Physiological Remodelling of Mitral Valve Chordae Tendineae In The Maternal Bovine Heart

by

Brandon Paul Scott

Submitted in partial fulfillment of the requirements
for the degree of Master of Applied Science

at

Dalhousie University
Halifax, Nova Scotia
July 2016

TABLE OF CONTENTS

LIST OF TABLES

LIST OF FIGURES

ABSTRACT

Maternal tissues necessarily undergo a dramatic series of physiological changes to effectively support the developing fetus. Arguably, the most profound and influential changes occur within the cardiovascular system. A state of volume overload develops in pregnancy, triggering a remodelling of the maternal cardiovascular tissues – including heart valves. The maternal heart valves display a remarkable capacity for structural, biochemical, and biomechanical transformation under these intensified hemodynamic conditions. The mitral valve in particular increases its anterior leaflet area by ~35%, with a striking ~22% increase in the number of chordae tendineae attachments to its ventricular surface.

The mechanism responsible for this maternal increase in chordae number is currently unknown. We hypothesize that chordae increase in number via the splitting of existing tendons, accompanying the leaflet expansion observed in pregnancy. The overarching objective of this thesis work is to establish the maternal chordae as actively remodelling structures similar to the anterior leaflet, and to determine the mechanism by which maternal chordae tendineae multiply. Using a bovine pregnancy model, chordae from never-pregnant heifers and pregnant cows were harvested from a local abattoir. Differential scanning calorimetry was performed to assess collagen thermal stability, while longitudinally-cut histological sections were stained with Picrosirius Red and Movat Pentachrome to reveal collagen crimp and general extracellular matrix composition (ECM) respectively. Chordal sections were additionally immunostained for α-SMA to identify activated valvular interstitial cells (aVICs), and for periostin – a protein required for proper fetal chordae branching patterns.

The evidence presented herein suggests that chordae splitting may be occurring in both heifers and pregnant animals. Collagen thermal stability, all crimp metrics, and the quantity of aVICs were largely unchanged between pregnancy groups. However, chordae bifurcations displayed a unique ECM compared to the surrounding tissue: a surplus of glycosaminoglycans, high cell density, and the presence of longitudinally-oriented elastin propagations into the tissue core – all evidence of active ECM remodelling in both heifers and pregnant cows. Periostin expression was elevated at bifurcations and found overlapping with elastic fiber propagations – supporting the chordae splitting concept in both animal groups. Irrespective of pregnancy state, differences in thermal stability and crimp structure were observed between strut, basal, and marginal chordae.

This work has shown, for the first time, that chordae bifurcations are unique in their composition and structure, suggesting that chordae splitting may occur in *both* heifers and pregnant cows as a fundamental, routine tissue turnover mechanism. As our understanding of the pregnancy-specific mechanisms responsible for the maternal increase in chordae number improves, so too does the therapeutic potential for valvular disease and heart failure which in many cases, share similar remodelling triggers (volume overload) to that of pregnancy.

LIST OF ABBREVIATIONS USED

ANOVA	Analysis of Variance
AV	Atrioventricular
aVIC	Activated Valvular Interstitial Cell
CRL	Crown-to-Rump Length
DAB	Diaminobenzidine
DNA	Deoxyribonucleic acid
DSC	Differential Scanning Calorimetry
ECM	Extracellular Matrix
EDTA	Ethylenediaminetetraacetic acid
EMT	Endothelial-Mesenchymal Transdifferentiation
FWHM	Full Width Half Maximum
GAG	Glycosaminoglycan
HIT	Hydrothermal Isometric Tension
HRP	Horseradish Peroxidase
MMP	Matrix Metalloproteinase
PBS	Phosphate Buffered Saline
qVIC	Quiescent Valvular Interstitial Cell
SD	Standard Deviation
SE	Standard Error
T_{onset}	Onset Temperature
T_{peak}	Peak Temperature
VIC	Valvular Interstitial Cell
α-SMA	α-Smooth Muscle Actin

ACKNOWLEDGEMENTS

There are many people requiring acknowledgement for the completion of this thesis. Firstly, I'd like to thank my supervisor Dr. Sarah Wells, for the opportunity to work on this project and helping me see it through to its fulfillment. To my other committee members – Dr. Michael Lee and Dr. Samuel Veres – I'd like to say thank you for the inspiration and advice you've provided me while working with this project. I've learned an extraordinary amount from everyone.

The bulk of this thesis relied on a series of histological experiments – techniques with which I originally had no familiarity. This project would not have been possible without the histology expertise provided by Patricia Colp, who was always friendly, enthusiastic, and willing to assist whenever possible. A sincere thank you goes out to Michel Johnson for his technical assistance with differential scanning calorimetry, and to the workers of Reid's Abattoir for consistently making my bovine heart collection a rather entertaining experience. I'd also like to mention the students of Dalhousie's Integrated Science Program who've contributed to the image analyses for this work.

Furthermore, the author would like to thank the funding sources for this project: The Natural Sciences and Engineering Research Council of Canada and The Dalhousie Medical Research Foundation.

Lastly, to all my family and friends, thank you for your continued support throughout my thesis research. Specifically, to my parents Paul and Cecelia, I would not be who I am today without your continual encouragement, guidance, and love.

Chapter 1
Introduction

1.1 Overview of Cardiac Physiology

The heart is comprised of four muscular chambers – two thin-walled atria and two relatively thick-walled ventricles. Together, these chambers function as two pumps in series to circulate blood throughout the body. The right atrium and right ventricle act as one pump, propelling oxygen-poor venous blood towards the pulmonary circulation for oxygenation, while the left atrium and left ventricle pump oxygen-rich blood towards the systemic circulation. Compared to the ventricles, the atria are under relatively low pressures (~6-8 mmHg) and function largely as terminal reservoirs of the venous system. Their contractile behaviour serves primarily to optimize ventricular filling during the cardiac cycle, a phenomenon known as "atrial kick"[1].

Although both higher than the pressures experienced by the atria, the dramatically different pressures experienced by the left and right ventricles during the cardiac cycle are reflected in their muscular architecture. Healthy peak pressures in the left ventricle during the contractile phase are approximately three times higher than those endured by the right ventricle. Moreover, the force required to propel blood towards the peripheral organs is 6-7 times greater than what is needed to drive blood flow through the pulmonary circuit. As a result, the left ventricular wall is twice as thick and has nearly three times the mass of the right ventricle[2].

Situated between the atria and ventricles are two inflow valves, also known as the atrioventricular (AV) valves. The tricuspid valve is found on the right side of the heart, and the mitral or bicuspid valve is on the left. The semilunar valves, so named because of their crescent shaped connective tissue cusps, are the outflow valves permitting blood to flow towards the lungs for oxygenation (pulmonary valve) and through the aorta for systemic distribution (aortic valve). Despite their unique anatomical locations and profound structural differences, the role of both the semilunar and AV valves is

ultimately to maintain a unidirectional flow of blood through the heart. An overview of heart anatomy is presented in Figure 1.1.

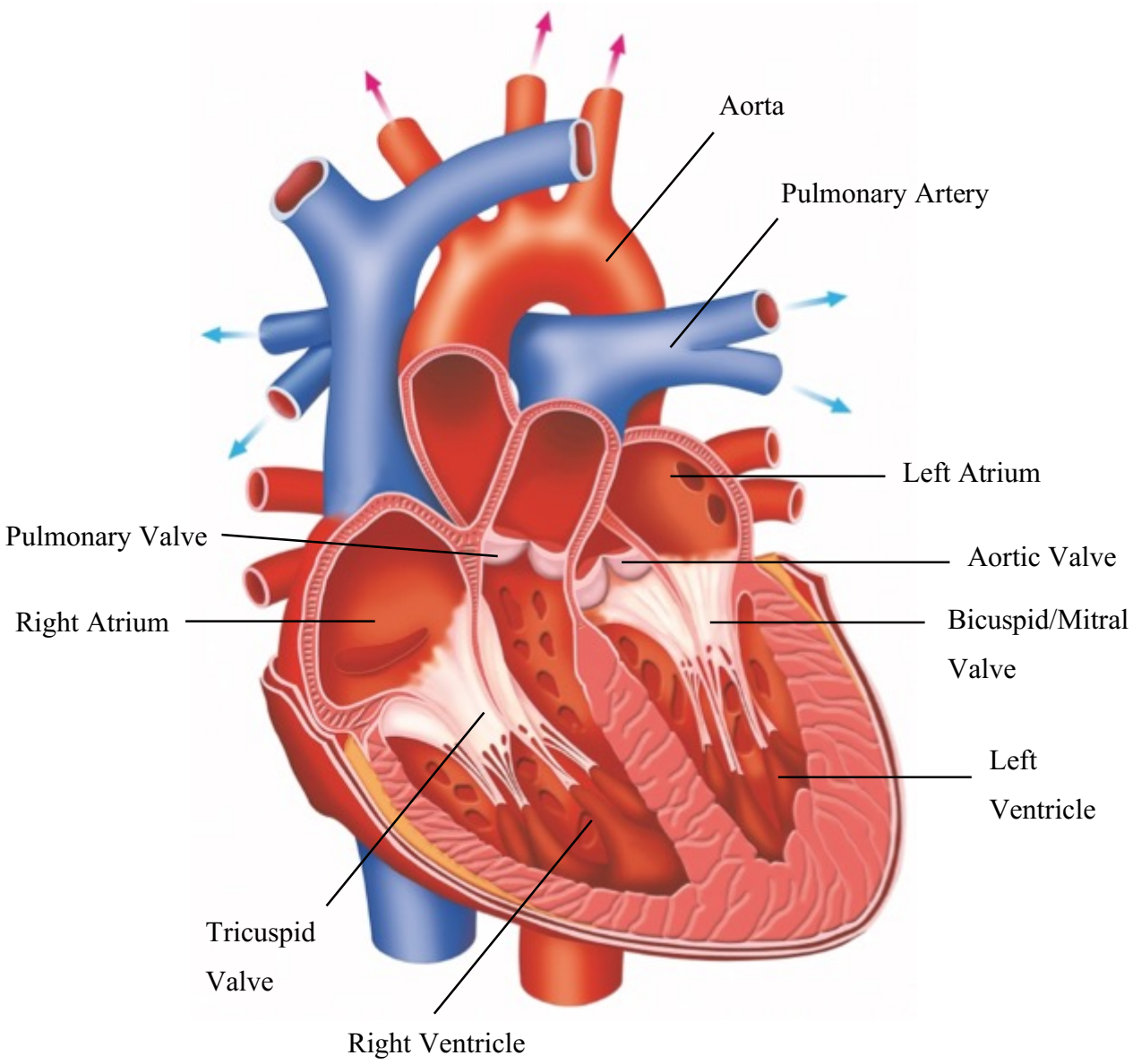

Figure 1.1: Schematic of heart anatomy. Retrieved and modified from: http://www.howitworksdaily.com/inside-the-human-heart/[3].

1.1.1 The Cardiac Cycle

The cardiac cycle is defined by a series of electrical and mechanical events, which generate the necessary pressure gradients to drive blood flow throughout the body. Pressure-volume loops, which visually demonstrate the relationship between left ventricular volume and left ventricular pressure, are an informative means by which to follow the cardiac cycle as it progresses (Figure 1.2). The cardiac cycle is commonly divided into two phases: a phase of myocardial contraction (systole), followed by a phase of relaxation (diastole). At the end of ventricular filling, just as the pressure inside the ventricle surpasses that of the atrium, the AV valves close and ventricular contraction begins. Initially, the pressure inside the ventricle is lower than arterial pressure and thus, both the AV valves and semilunar valves are closed. This gives rise to a sharp increase in pressure as the ventricle contracts – a cardiac event known as isovolumic contraction (Figure 1.2, 'A'). Once the pressure inside the ventricle exceeds arterial pressure, the semilunar valves open and the ejection phase of the cardiac cycle begins whereby blood is forced out of the ventricles into the aorta and pulmonary trunk (Figure 1.2, 'B'). The ejection phase is initially characterized by an increase in ventricular pressure as blood flow into the aorta exceeds peripheral blood flow from its branches, and then gradually falls as ventricular output decreases whilst flow from the aorta persists[2,4].

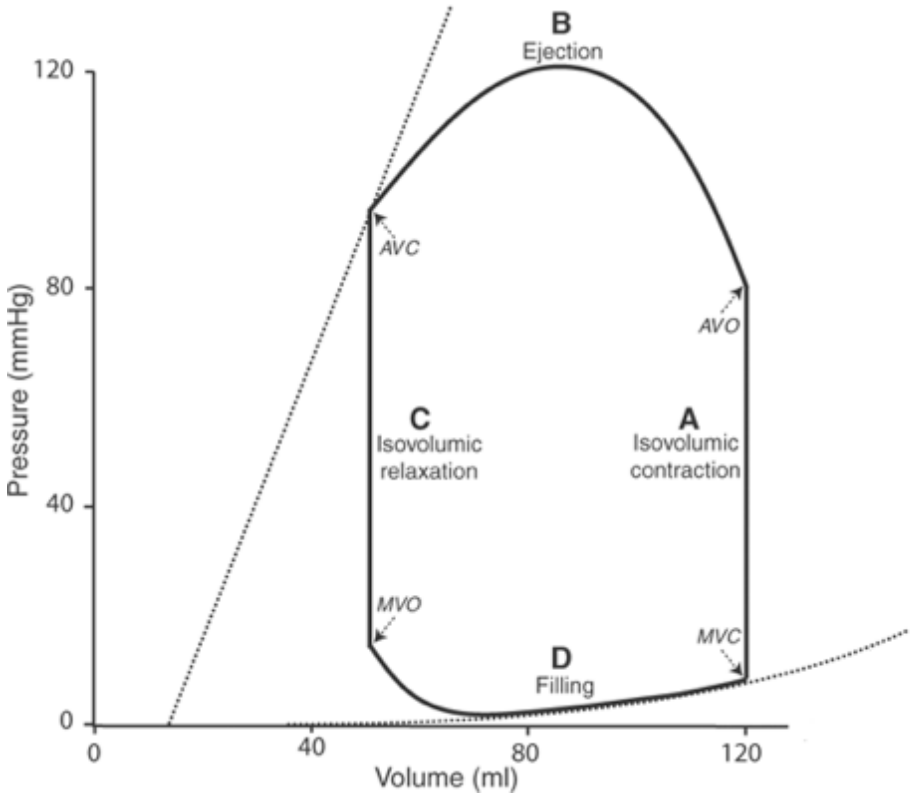

Figure 1.2: Left ventricular pressure-volume loop. MVC – mitral valve closure, AVO – aortic valve opening, AVC – aortic valve closure, MVO – mitral valve opening. Taken from Katz (2010)[2].

The transition from ventricular systole to diastole is marked by semilunar valve closure as ventricular pressure drops. During isovolumic relaxation, the AV and semilunar valves are closed and ventricular pressure continues to drop sharply until it falls below that of the atrium (Figure 1.2, 'C'). This pressure difference causes the AV valves to open, allowing the ventricle to fill rapidly with blood (Figure 1.2, 'D'). Ventricular filling is terminated by atrial systole, which delivers a final surge of blood to maximize ventricular volume prior to contraction. At this point, the wave of depolarization responsible for the preceding atrial contraction reaches the ventricular myocardium and recommences the cardiac cycle with ventricular systole. At rest, the entire cardiac cycle takes approximately 800 ms to complete[4].

Despite all the complex electrical and mechanical events involved with each loop of the cardiac cycle, the efficiency of the entire process relies heavily upon maintaining a unidirectional flow of blood through the heart. This responsibility is borne by our heart

valves, which prevent retrograde flow between chambers and the inappropriate exchange of blood between the ventricles and the arterial outlets. A function of such high importance has inevitably lead to the formation of remarkable connective tissue structures able to withstand a lifetime of high cycle fatigue loading without failure.

1.2 Heart Valves – The Guardians of Unidirectional Flow

Heart valves are multicomponent, multilayered connective tissue flaps covered in a layer of endothelial cells (endocardium). All four valves of the heart lie in a common plane towards the base of the heart in a region known as the fibrous skeleton – a region that consists primarily of dense collagen fibers (collagen is discussed in more detail in Section 1.2.2). The fibrous skeleton functions to electrically insulate the atria from the ventricles to ensure proper cardiac conduction, and, importantly for valve biomechanics, is anchored to the myocardium and serves to provide mechanical support for the heart valves[5]. The pulmonary and aortic valves are macroscopically quite similar, consisting of three similarly sized leaflets whose free edges coapt to prevent arterial backflow during diastole. Histologically, both the aortic and pulmonary valves consist of three distinct tissue layers containing varying amounts of collagen, elastin, proteoglycans, and glycosaminoglycans (GAGs)[5,6]; the local distribution of these extracellular matrix (ECM) proteins and polysaccharides are tailored to the mechanical forces endured by specific regions of the valve tissue[6-9]. Crucial to the ECM remodelling of valvular tissue is the presence of valvular interstitial cells (VICs), which reside throughout all three morphologically distinct layers[10].

The atrioventricular valves are open during diastole, and closed during systole to prevent retrograde flow into the atria. In terms of composition, atrioventricular valves are similar to the semilunar valves in that their principle components are collagen, elastin, proteoglycans, GAGs, and VICs. Moreover, they also contain a tri-layered tissue structure in which the relative amount of these constituent molecules is spatially unique. This provides structural and functional heterogeneity optimized for the cyclic loading patterns endured throughout the cardiac cycle[11,12]. Compared to the semilunar valves however, the atrioventricular apparatus is structurally more elaborate. Altogether, they

are comprised of four components: the valve leaflets, annulus, papillary muscles, and chordae tendineae.

The annulus is a saddle-shaped fibrous ring that serves to anchor the valve leaflets and undergoes 3D deformations during the cardiac cycle[13,14]; such dynamic motion is believed to optimize ventricular filling during diastole and facilitate valve coaptation during systole[15]. As their names suggest, the tricuspid valve has three leaflets forming the coaptation surface, while the bicuspid (mitral) valve contains only two. The remaining components of the atrioventricular valve – the chordae tendineae and the papillary muscles – are collectively called the subvalvular apparatus. The chordae tendineae are cardiac tendons that insert into the ventricular aspect of the leaflets on their basal end, and attach apically to small projections of the ventricular myocardium known as the papillary muscles. Their role is to maintain leaflet closure and prevent valve inversion under the high ventricular pressures associated with systole[11]. Collectively, these four structures act in tandem to ensure proper cardiac function and to ultimately maintain a unidirectional flow of blood through the heart.

Heart valves, especially the atrioventricular valves, are more than passive assemblages of connective tissue. They actively control intracardiac blood flow through dynamic annular and leaflet deformation, and via papillary muscle contraction[16], experiencing an assortment of sophisticated biomechanical forces with every heartbeat. These valves are actively remodelled by VICs throughout our lifetime, continually renewing GAGs and collagen to preserve long-term valve durability and healthy cardiac function[8,17,18]. Heart valve disease and ventricular dysfunction cause inappropriate valve remodelling, jeopardizing the heart's ability to efficiently deliver blood to peripheral tissues. With an aging population, heart valve disease is on the rise with a national prevalence of approximately 2.5% in the United States – a situation described by some as the next cardiac epidemic[19-21]. Owing to its importance in overall heart function, relatively high disease prevalence in comparison to other heart valves, and ill-understood remodelling mechanisms, this work will be focused specifically on the mitral valve and its associated chordae tendineae.

1.2.1 Mitral Leaflet Anatomy & Structure

The mitral valve is comprised of two main leaflets – a smaller posterior leaflet, and a larger anterior leaflet (Figure 1.3). Due to the anatomical inaccuracy of their respective names, the posterior leaflet is also referred to as the mural leaflet, and, the anterior leaflet, which maintains a degree of fibrous continuity with regions of the aortic valve, is commonly called the aortic leaflet[22]. These two leaflets are separated by the presence of two large indentations, or commissures, that give rise to a third and often-forgotten portion of the mitral valve known as the commissural leaflets. The posterior leaflet encompasses two-thirds of the annular circumference, yet its surface is approximately half that of the anterior leaflet[23-26]. The result is a rather narrow and elongated posterior leaflet, as opposed to the more rounded anterior leaflet. Recognizable indentations divide the posterior leaflet into three scallops known as P1, P2, and P3. Although no indentations exist along its perimeter, the same naming conventions apply to the anterior leaflet (A1-A3), facilitating regional descriptions in parallel with its posterior counterpart[27,28] .

Throughout systole when the mitral valve is closed, the posterior and anterior leaflets overlap distally to form the coaptation zone (Figure 1.3). The combined surface area of the two leaflets together is 1.5-2 times greater than the orifice area created by the annulus, giving rise to a surplus region of leaflet tissue during valve closure[29]. This areal redundancy is known as the valve's "functional reserve," accommodating modest hemodynamic fluctuations and changes in annular dimension without severe clinical complication[29,30]. The ventricular surface within the coaptation zone is populated with chordal attachments and, due to its appearance, is appropriately named the rough zone. Conversely, any regions of the leaflet tissue lacking chordae tendineae (generally more central regions and those proximal to the annulus) are called clear zones[22] (Figure 1.6).

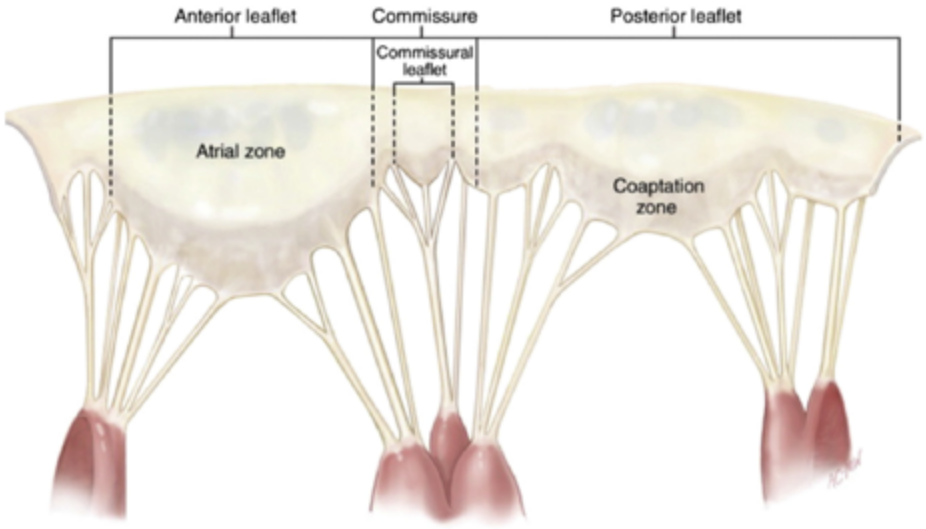

Figure 1.3: Schematic of the unfolded mitral valve showing leaflets, chordae, and papillary muscles. Taken from Carpentier (2010)[31].

Past histological analyses of the mitral leaflets described four distinct tissue layers: the atrialis, spongiosa, fibrosa, and ventricularis[32]. However, the mitral leaflets are now predominantly described throughout the current literature as being trilaminar structures, whereby the fibrosa and ventricularis are viewed as a single, united layer. The atrialis is the uppermost layer facing the left atrium. A monolayer of endothelium covers its surface, which overlays a grouping of elastic fibers, mixed with a smaller quantity of collagen fibers. The high presence of elastic fibers in the atrialis is believed to help resist radial strains when the valve is open[11]. The middle layer, or spongiosa, is composed primarily of proteoglycans and GAGs. The abundance of the highly anionic GAG side-chains in this layer provides mechanically advantageous tissue hydration, which acts to lubricate the atrialis and fibrosa during leaflet bending[22,33-35]. Lastly, the largest pressures and tensile loads are borne by the fibrosa and as such, it contains the highest collagen content with only sparse elastic fibers[36]. Similar to the atrialis, the blood-contacting surface is covered in a layer of endothelial cells. The individual thicknesses of each layer vary from the annular attachment to the free edge following its functional need. The atrialis and spongiosa layers increase in thickness distally, while the fibrosa layer becomes increasingly thin[22].

1.2.2 Collagen Structure, Remodelling, & Thermal Stability

Collagen is ubiquitously found throughout the human body, and is the main structural protein found in heart valves. A single collagen molecule is comprised of three individual α-helices (polypeptide chains), which themselves combine to form collagen's characteristic triple helical structure. Each α-chain contains a repeating Glycine-X-Y amino acid triplet, where X and Y can be any amino acid[37], although they are most commonly proline or hydroxyproline[38,39]. Collagen is organized hierarchically; from the molecular scale all the way up to a visible human tendon, collagen is strategically packed into progressively larger structures that grant the tissue remarkable tensile properties. Collagen molecules assemble laterally and longitudinally to form collagen fibrils – typically on a scale from 50 to a few hundred nanometers in diameter. A grouping of collagen fibrils compile to form collagen fibers, which are then packaged into fascicles that finally form the overall tendon structure[40]. Collagen fibers often exhibit collagen crimp: a microscale repeating fiber wave that allows the tissue to mildly extend under low stress before molecular engagement of the collagen backbone itself (collagen mechanics are discussed in more detail in Section 1.2.6).

The α-helices of collagen molecules are held together and primarily stabilized by intramolecular hydrogen bonding[38]. The tensile strength of collagen fibers however, is largely granted by the presence of intermolecular cross-links[41]. During assembly, neighbouring collagen molecules are covalently cross-linked at specific locations by lysyl oxidase. Over time, these originally divalent immature cross-links react spontaneously to become mature, trivalent cross-links[41]. The ratio of immature to mature cross-links within collagenous tissues – like heart valves – can be an indicator of the remodelling state of the tissue. This is because immature cross-link formation occurs more quickly than does the formation of mature cross-links; adult tissues contain relatively few immature cross-links as these are converted into mature cross-links with time[42,43]. Therefore, a tissue with a larger immature to mature cross-link ratio can be viewed as having a larger proportion of newly synthesized collagen and thus, is seen as a more actively remodelling tissue[44,45].

Importantly for the concepts presented in this thesis, collagen's thermal stability can also be related to its remodelling state and organization. Collagen denaturation occurs

via the rupture of its hydrogen bonds, causing a loss of native triple helical structure into a random coil configuration[46]. One region of the collagen molecule in particular – the thermally labile domain – is the least thermally stable and is consequently the site of initial α-chain uncoupling[47]. The thermal energy required to denature collagen depends heavily upon the physical packing of adjacent molecules. A more tightly packed collagen network confines the thermally labile domain, reducing its configurational entropy and thus requiring a greater energetic input to unfold and initiate collagen denaturation[47]. This is known as the polymer-in-a-box mechanism of collagen thermal stability (Figure 1.4). Indeed, collagen molecules in solution (not confined within a fiber lattice) display denaturation temperatures only slightly above body temperature[48]. With this in mind, methods such as hydrothermal isometric tension (HIT) and differential scanning calorimetry (DSC), which probe the thermal properties of collagen, can provide an indirect look into the molecular organization of tendons. Lower denaturation temperatures obtained through these techniques signify an increased lateral spacing of collagen molecules within the tissue. Increased lateral spacing can result from increased mechanical loading and active cellular remodelling[45,49] – a concept that will be referred back to with respect to leaflet and chordal remodelling in this work.

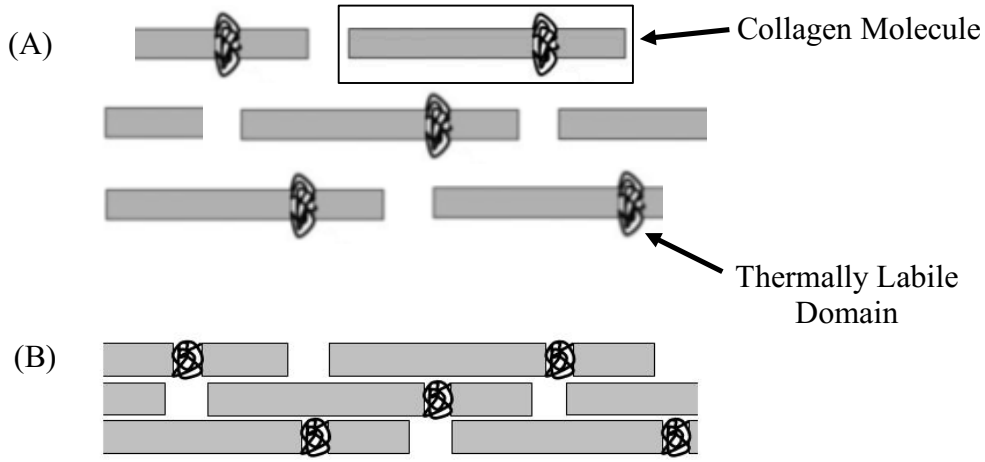

Figure 1.4: The Polymer-in-a-box mechanism for collagen thermal stability[47]. (A) Increased lateral spacing between collagen molecules leaves the thermally labile domain relatively unconstrained, leading to lower denaturation temperatures in thermal analyses such as differential scanning calorimetry. (B) Thermally labile domain configurations are restricted by neighbouring molecules when tightly packed, leading to molecular stabilization and higher denaturation temperatures.

1.2.3 Chordae Tendineae Internal Structure

The mitral chordae tendineae are extensions of the leaflet fibrosa. Superficially, the chordae are wrapped in an outer layer of endothelial cells continuous with that of the valve leaflets[50,51] (Figure 1.5). Beneath this endothelial exterior is a heterogeneous protein layer dominated by elastin fibers. Elastin provides the tissue with its necessary distensibility and is believed to facilitate force transfer to the valve leaflets[52]. Upon recoil, elastin also helps restore collagen crimp as tension dissipates. In this layer, blood vessels can be found running from the papillary muscle up to the mitral valve leaflets[52]. As we progress deeper into the tendon core, collagen content increases substantially and the elastin content is minimal. By dry weight, collagen makes up approximately 60% of the chordae tendineae[53,54] and is responsible for the remarkable tensile strength of these tendons; the most prominent collagens in the chordae are types I and III[55]. Although less abundant than what is found in the leaflets, chordae also contain proteoglycans and GAGs throughout the tissue bulk[53], namely decorin and biglycan[56].

Ultrastructural studies on human mitral valve chordae using scanning and transmission electron microscopy have shown that collagen fibrils contained within larger longitudinally-oriented bundles vary considerably in their directionality[57,58]. The variable alignment of collagen fibrils (nanoscale) and dense waves of collagen crimp (microscale) within chordae could speak to their function as fatigue resistant structures, having to endure ~35 million tensile loading cycles each year. Under the cyclic tensile stress imposed by the beating heart, such an arrangement would first allow the crimped fiber bundles to flatten, followed by the alignment of the collagen fibril network within these bundles. This limits excessive strain on the collagen backbone itself at low loads[58]. Together, the spatial distribution of collagen and elastin within the chordae tendineae is well suited to its cyclic loading environment; however, over time, these proteins on their own are not capable of enduring a lifetime of cyclic loading. The longevity and structural integrity of the valvular tissue is also maintained through routine tissue turnover by VICs[8,17,18]. These fibroblast-like cells are evenly distributed throughout the inner and outer layers of the chordae[52].

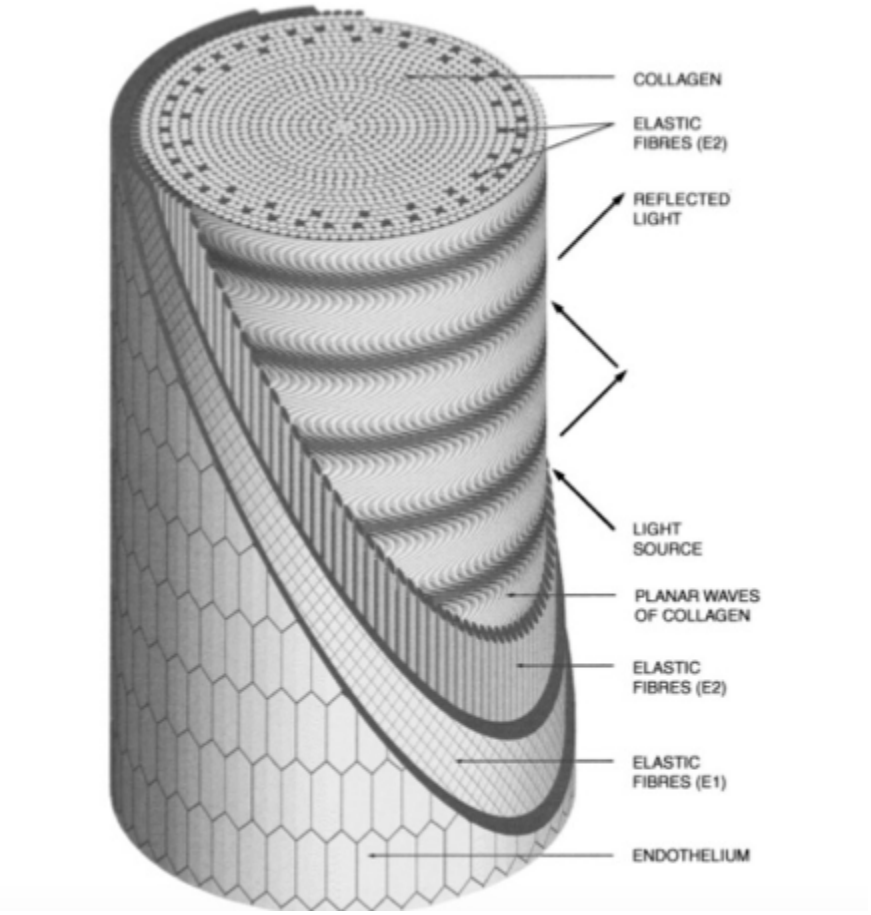

Figure 1.5: Histological composition of the chordae tendineae. Alternating light and dark bands in the collagen core correspond to the waves of collagen crimp. Taken from Millington-Sanders et al. (1998)[51].

1.2.4 Chordae Nomenclature

The complexity of the chordae branching network and diversity of their insertion locations into the leaflet fibrosa has, out of necessity, led to a system of classification for chordae. Unfortunately, chordae nomenclature has become ambiguous over the years as various authors continue to use different terminology in describing the same anatomically located chordae. Beginning in the early 1900s and continuing throughout most of the 20th century, a three-order system was developed to describe the insertion locations of the various chordal attachments[59-61]. In 1970, Lam et al. refined the original classification

system to further emphasize the morphological differences between chordae and to provide a more detailed overview of chordal arrangement[62]. The primary (first order), or marginal chordae, attach to the free edge of both the anterior and posterior leaflets. In doing so, marginal chordae commonly split and form multiple attachments within close proximity to the free edge, creating a fine network of translucent chordae[61]. According to the classification of Lam et al. (1970), the group of first order chordae was extended to include commissural and cleft chordae. Commissural chordae include all chordae attached to the commissural leaflet (leaflet indentations which separate the anterior and posterior leaflet), while the cleft chordae define – and attach to – the distinct notches of the posterior leaflet that form P1, P2, and P3.

Secondary (second order) chordae attach to the main body of both leaflets beyond the free margin. These numerous chordal attachments, which may arise from the same bifurcating stem as the marginal chordae, roughen the ventricular surface of the leaflet creating a series of mild endocardial folds[63]. As such, these chordae are frequently called rough zone chordae. The two largest rough zone chordae that attach to the anterior leaflet of the mitral valve are called the strut chordae. These chordae are easily identifiable by their size and their characteristic attachment at approximately the 4 and 8 o'clock positions[62]. Lastly, the tertiary (third order), or basal chordae, are exclusive to the posterior leaflet. Basal chordae originate from the left posterior ventricular wall and insert directly (i.e. are unbranched) into the posterior leaflet near the annular tissue[61,62,64].

Although the foundations of this nomenclature have remained the same, confounding variation in use of this terminology has arisen in more recent times making it difficult to compare chordae between publications[29,65]. For example, traditionally basal chordae have been viewed, as described above, as being attached only to the posterior leaflet as single, tendinous extensions from the ventricular wall. Some authors describe the basal chordae as merely rough zone chordae on both the anterior and posterior leaflets[36,66], while others refer to basal chordae as the intermediate chordae[67]. Further still, Ritchie et al. (2005)[52] identify basal and intermediate chordae as distinct structures on the posterior leaflet based on their insertion distance from the annulus. From the perspective of such researchers, tertiary chordae are no longer a recognizable grouping. The most recent publication by Gunnal et al. (2015)[68] provides an intricate morphological

evaluation of chordae studied in human cadavers, presenting more the 20 distinct terminologies for chordae based upon their origin, attachments, insertion, distribution, branching pattern and gross structure. For simplification, the naming conventions used herein for anterior leaflet chordae will follow the outline provided in Table 1.1 and Figure 1.6.

Table 1.1: Types of chordae tendineae and their anatomical descriptions.

Chordae Terminology	Description
Marginal	Attach to leaflet free edge
Basal/Rough Zone	Attach beyond free margin into body of leaflet tissue
Strut	The largest two chordae attached beyond the free margin at approximately the 4 and 8 o'clock positions

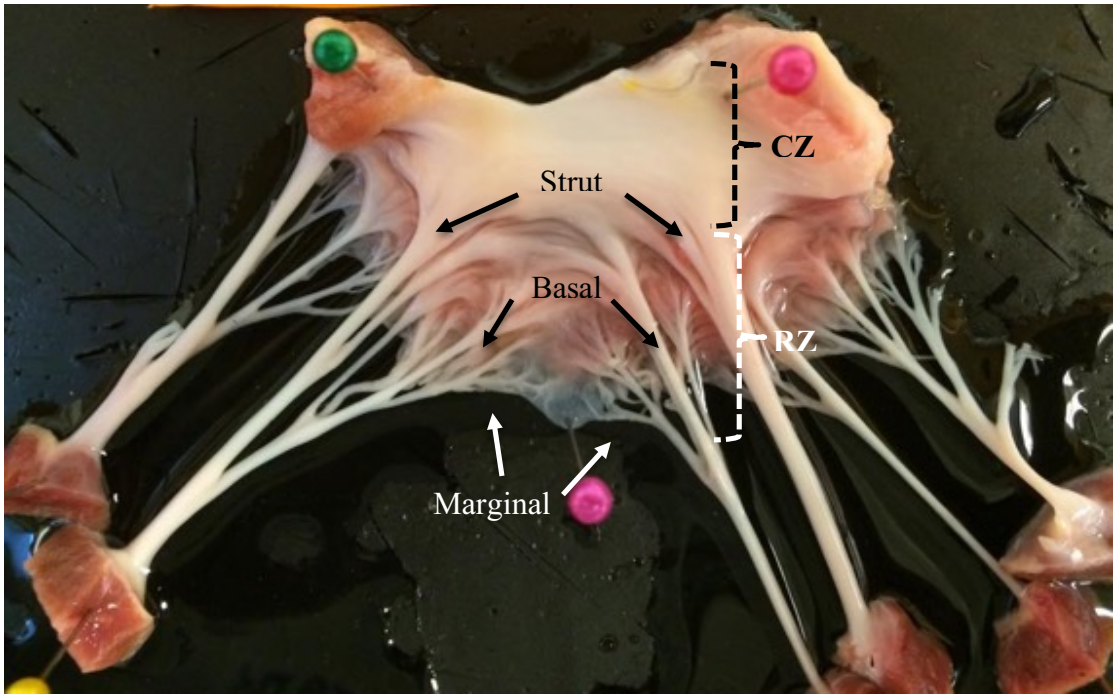

Figure 1.6: Excised bovine mitral valve anterior leaflet showing examples of the strut, basal, and marginal chordae types in relation to the rough and clear zones (RZ, CZ).

Despite this useful naming system, ambiguity can still remain as not all mitral valves are identical. Indeed, there is considerable intervalvular variability in chordae branching patterns, overall number, and papillary muscle architecture[68,69]. Typical rough zone chordae branch three times before they insert into the anterior leaflet; one chorda becomes continuous with the free edge whilst the others insert beyond to reinforce the coaptation zone. A study of 50 human mitral valves showed that nearly 20% of rough zone chordae from the anterior leaflet were atypical, showing abnormal branching patterns[62]. Similarly, Becker & De Wit (1979) described a "spectrum of normality" with respect to the chordal apparatus after finding deficient branching in the rough zone chordae in 39 of 100 otherwise normal human mitral valves. Interestingly, 36 out of 40 mitral valves with a leaflet deformity had atypical chordal apparatuses located in the region of the leaflet defect, suggesting that variations in chordal architecture could have functional consequences[70].

1.2.5 Not All Chordae Are Created Equal

Each specific group of chordae (named here as: marginal, basal, and strut) has unique composition, microstructure, and characteristic mechanical properties that reflect their different roles in not only preserving proper valve function, but also in maintaining ventricular normality. Early observations by Lim and Boughner (1975) clearly demonstrated that larger chordae (strut and basal) were more extensible than those with smaller diameters (marginal)[50]. These observations were later confirmed by Kunzelman and Cochran (1990), who also described marginal chordae as being significantly stiffer than the larger basal chordae[71]. Without any further experimentation, these studies rationalized that basal chordae were critical for establishing an even leaflet surface during valve closure[50], while marginal chordae, with a higher modulus and being more numerous, would carry a greater stress during systole to effectively support the mitral valve leaflets[71]. Although these studies merely speculated as to the functional ramifications of mechanically distinct chordae, later studies sought to answer these specific questions.

Following their original study, Lim and Boughner (1976) used transmission electron microscopy to assess collagen ultrastructure in human mitral valve chordae tendineae. They discovered an inverse relationship between collagen fibril density and chordae diameter, providing an explanation for the greater extensibility observed in thicker chordae[57]. Approximately 30 years later, in a pair of comprehensive studies performed by Liao and Vesely (2003) and Liao et al. (2009)[72,73], a structural basis for the size-related mechanical properties of mitral chordae tendineae was proposed. Thin, marginal chordae had smaller fibril diameters, relatively high fibril densities, and a larger crimp wavelength – all evidence to support a stiffer, less extensible structure. Differences in fibril configuration and fibril-fibril interactions were thus responsible for the significant differences in mechanical properties between chordae types[72,73].

Beyond collagen architecture, different chordae types have unique compositions and cellularity. Marginal chordae have a higher amount of newly synthesized collagen and DNA per mg of tissue compared to both basal and strut chordae[52]; this indicates a higher quantity of VICs in these tissues (VICs are discussed with more detail in Section 1.3). Moreover, marginal chordae contain a higher concentration of GAGs[54]. These data correlate well with our understanding of marginal chordae as stiffer structures which experience less stress relaxation than other chordae, as more proteoglycan linkages between collagen fibrils could prevent fibril-fibril slippage[54].

All in all, the structures of different chordae adhere to their specific functional roles. Through transection (chordae severing) studies, chordae of each type have been eliminated from the working mitral valve to gain a better understanding of each chorda's primary purpose in valve and ventricular function. Severed marginal chordae, as studied in an isolated pig heart model, can lead to significant free edge prolapse and mitral regurgitation[74]. Similarly, excised porcine mitral valves lacking marginal chordae placed in a left ventricular pulsatile flow system demonstrate severe regurgitant flow[75]. Marginal chordae thus maintain proper leaflet coaptation and valve competence. Reasonably, a tensile structure with a responsibility of this magnitude would benefit from a high presence of synthetic VICs and increased collagen synthesis to preserve its structural integrity[52].

Comparable studies reveal a completely different role for basal and strut chordae. The network of basal chordae act as a continuous, dynamic link between the papillary muscles and leaflet tissue. They play a supportive role by preventing inappropriate leaflet bulging and papillary muscle displacement, and effectively transfer force between the leaflets and papillary muscles to reduce the systolic stresses imposed on the anterior leaflet belly[75-77]. Lastly, and unlike marginal and basal chordae, severing both strut chordae *in vivo* does not impair leaflet coaptation, alter leaflet shape, nor create mitral regurgitation[78]. Rather, strut chordae appear to be important for upholding left ventricular geometry and function. Cutting strut chords reportedly impairs the development of left ventricular pressure, decreases aortic blood flow, compromises left ventricular systolic function, disturbs ventricular geometry, and induces myocardial remodelling between the papillary muscles[79-81]. Despite this evidence, some authors maintain that left ventricular performance and papillary muscle geometry is preserved, leaving the importance of strut chordae somewhat controversial[82].

Understanding the unique duties performed by the numerous chordal attachments has tremendous clinical merit. Many surgical procedures that seek to improve mitral valve competence involve translocating, severing, or shortening specific chordal attachments, whilst others incorporate the use of synthetic chordae to replace those which have degenerated or completely ruptured[83]. Such operations must therefore take into consideration the individual functional roles and mechanical properties of specific chordae to avoid potentially harmful long-term repercussions on valve and ventricular function. Moreover, a better understanding of chordae physiology, structure, and remodelling potential in both health and disease, could help guide such clinical treatments in the future.

1.2.6 Mitral Valve Biomechanics

The mitral valve as a whole experiences a myriad of forces and actively participates in optimizing the unidirectional flow of blood through the heart during the cardiac cycle. Together, the annulus, leaflets, chordae, and papillary muscles must act synergistically to achieve proper function. The opening and closure of the mitral valve is influenced by

blood flow patterns, the development of specific pressure gradients, and the coordinative contraction of the left ventricle and papillary muscles[12]. As the valve opens, the annulus dilates[84] and the leaflets flex down into the ventricle, relieving the majority of tension on the chordae tendineae. A full unloading of all chordae is not achieved, as radial stretch is still present in the strut chordae insertion sites during diastole[85]. Blood shears past the leaflet tissue and fills the left ventricle until the pressure between the left atrium and left ventricle equilibrate, leading to valve closure. The annulus responds by achieving its characteristic saddle shape[86] and minimizing its orifice area[84] to facilitate the configuration and coaptation of the anterior and posterior leaflets, in addition to minimizing excessive leaflet and chordal stresses[87-89]. The central region of the anterior leaflet and the chordae tendineae primarily experience tension, while the majority of the posterior leaflet and the coaptation zone encounter appositional compression[56]. Reasonably so, collagen is dispersed preferentially towards those regions under greater tension[90], whilst areas under compression contain a higher proportion of proteoglycans and GAGs[56,91].

The chordae tendineae experience tension along their length during systole, created at the leaflet interface and by the myocardium. Tension is generated apically through papillary muscle contraction, and, at the same time, tension is created in the basal direction as pressure gradients force leaflet closure[67]. During systole, the marginal chordae encounter tensile forces of approximately 0.1N, while strut chordae face tension of nearly an order of magnitude greater[76,92-94]. Chordae, like other collagenous tissues under tension, exhibit a characteristic non-linear stress-strain curve (Figure 1.7). In the initial phase of elongation, collagen crimp collapses providing low-load tissue extensibility[95]. This is followed by the non-linear "heel" region of the stress-strain curve whereby collagen fibers and fibrils align in the direction of the applied load, giving rise to an increase in modulus[67]. As extension continues, collagen molecules become fully engaged as triple helices and their connecting intermolecular cross-links stretch, resulting in a curve with constant modulus until failure begins[96,97]. The extensibility and stiffness of the chordae must be tactfully regulated to avoid leaflet prolapse and or inadequate closure, which would inevitably cause regurgitation. Moreover, their high crosslink content mitigates chordal creep – a situation that would be functionally unacceptable if

encountered on a physiological time-scale[67].

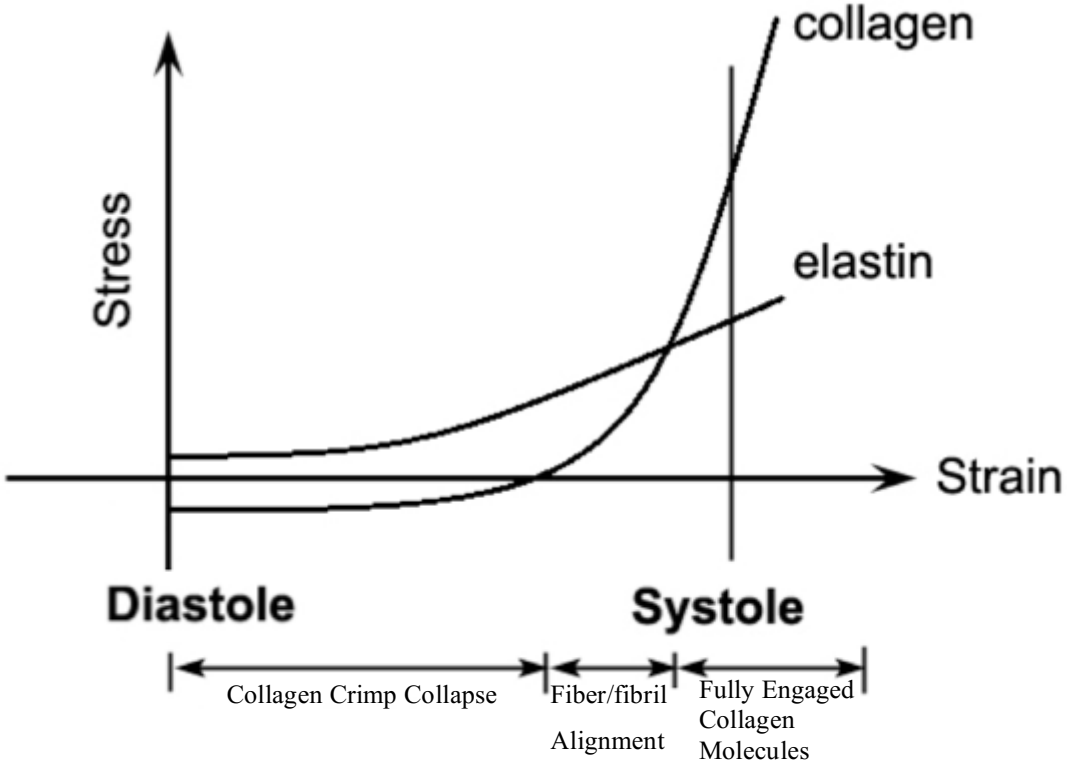

Figure 1.7: General non-linear stress-strain curve for chordae tendineae showing the relationship between tissue loading and the cardiac cycle. As pressure in the ventricle rises during systole, collagen crimp first collapses to provide extensibility at low stresses. The tissue modulus begins to increase as collagen fibers and fibrils begin to align with the applied tension, until all molecules become fully engaged and load-bearing. The tissue is unloaded during diastole where collagen crimp is restored with the help of elastin recoil. Modified from Schoen and Levy (1999)[8].

With such an interconnected and interdependent system of biological components, it's easy to see how even a slight morphological or functional abnormality could commence a deteriorative remodelling process. Changes in ventricular geometry or dimension, annular shape or diameter, and overall leaflet configuration can alter the stresses experienced by the chordae tendineae, as these structures act as the physical link between the myocardial wall and leaflet tissue. Altered mechanical stress can alter VIC behaviour and trigger cardiac remodelling.

1.3 Valvular Interstitial Cells, Extracellular Matrix Remodelling, & Disease

Valvular interstitial cells – the most prominent cell type resident to heart valves – are responsible for maintaining the delicate balance between ECM synthesis and breakdown[98]. They are a heterogeneous population of cells with multiple phenotypes. Although five distinct phenotypes have been described[99], the two most relevant phenotypes herein are the quiescent VICs (qVICs) and the activated VICs (aVICs). The former are fibroblast-like cells with relatively low metabolic activity, while the latter exhibit qualities of myofibroblasts and are involved with proliferation, migration, and extensive ECM remodelling[99]. In healthy human adult heart valves, only 2-5% of the cell population is comprised of aVICs as determined by their characteristic expression of α-smooth muscle actin (α-SMA)[100,101]. The continuous valvular remodelling process is mediated via the secretion of ECM molecules such as proteoglycans and GAGs[102,103], along with the expression of matrix degrading enzymes known as matrix metalloproteinases (MMPs) and their tissue inhibitors[18,98]. VICs modify their surrounding ECM, and in turn, the ever-changing ECM modulates VIC behaviour – a phenomenon known as dynamic reciprocity. Chemical cues such as transforming growth factor-β1 have been shown to activate qVICs and stimulate matrix remodelling[104,105]. Similarly, VICs can sense and respond extraordinarily well to altered mechanical loading environments.

Numerous studies have shown that the VIC phenotype, and by extension, the surrounding ECM, depend heavily upon the type and magnitude of mechanical stress experienced by the VICs. Different regions of the mitral apparatus encounter distinct mechanical forces when the valve is closed: the flat central region of the anterior leaflet and the chordae tendineae are under tension, while the free edge of the anterior leaflet and the majority of the posterior leaflet are in compression[56]. Accordingly, the distribution of collagen, proteoglycans, and GAGs is suited to the local biomechanics. The zones under tensile loading contain more collagen, and the regions under compression have a thicker layer of proteoglycans[56,90] as mentioned above in Section 1.2.6. The local VICs are responsible for this heterogeneity across the valve components;

qVICs are activated by mechanical stimuli to aVICs, that in turn regulate the production of ECM components[101,106]. *In vitro* experiments using 3D collagen gels seeded with VICs demonstrate that both cyclic and static mechanical strain influence proteoglycans and GAG secretion by VICs[107-109]. Furthermore, specific classes of proteoglycans and GAGs are synthesized based upon whether the forces endured are compressive or tensile in nature, creating local regions enriched with molecules optimally suited for that particular mechanical setting[56,91]. Collagen synthesis is also affected by mechanical load. Greater transvalvular pressures and tissue stress can lead to stress dependent biosynthesis of collagen by VICs[110,111]. Once the compensatory remodelling of the ECM is complete and the stress on the valve tissue has been normalized, the aVICs are able to return to their original quiescent phenotype[101,106]. A summary of VIC activity is given in Figure 1.8.

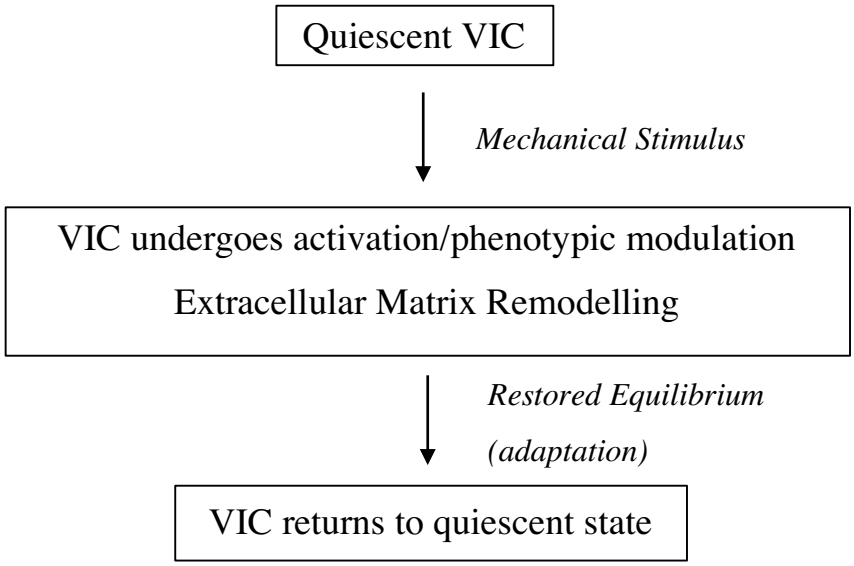

Figure 1.8: Proposed model for heart valve remodelling by VICs. Originally quiescent VICs respond to mechanical changes in their environment by activating then remodelling the surrounding ECM. Upon restoration of the valve's normal stress profile, aVICs return to their quiescent state until another mechanical stimulus is encountered. Modified from Schoen (2005)[112].

A wealth of knowledge exists surrounding cardiac remodelling in response to mechanical stress. Arguably the most well studied response involves the enlargement of the left ventricular myocardium, commonly observed in high performance athletes[113,114],

pregnant women[115-117], and cardiovascular disease[118-120]. Although left ventricular hypertrophy and changes in ventricular geometry have been well described in these populations, our understanding of heart valve remodelling has been – until recently – limited only to that of cardiac pathologies. For example, in left ventricular dysfunction and heart failure, the gross structure and composition of the mitral valve changes significantly with an increase in leaflet area, thickness[121], and collagen synthesis[122], along with a decline in water content[123]. These remodelling events contribute to pathological stiffening and a decrease in the viscous properties of the valvular tissue, often leading to mitral regurgitation[124]. There is strong evidence to show that the pathogenesis of valvular disease is attributable to unfavourable ECM remodelling due to the phenotypic adaptation of VICs under changing hemodynamic conditions and thus, the mechanical loading environment[125]. Myxomatous degeneration of the mitral valve is characterized by fragmented collagen and elastin[55,126-129], excess deposition of proteoglycans and GAGs leading to spongiosa thickening[53,127-131], altered hyaluronan metabolism[132], and changes in matrix degrading enzymes such as MMPs and elastases[133]. Such initial compositional changes lead to a mechanical deterioration of the valve, which then exacerbates the pathological remodelling process through abnormal mechanical feedback to the VIC population[133]. Indeed, diseased valves contain higher quantities of aVICs and are thus more actively remodelled[101,127]. These dramatic revisions to the ECM are more severe in the mitral chordae than in the leaflets and significantly reduce the mechanical load these structures can tolerate[134,135]. In myxomatous or "floppy" mitral valves, the leaflets are thickened and the chordae are frequently elongated and rupture as a consequence of the disrupted ECM, leading to valve incompetency and mitral regurgitation[127,136-139]. It is important to note that the aVIC remodelling taking place in diseased valves is dysfunctional and maladaptive, completely distinct from routine tissue turnover and other remodelling events.

We have clearly seen how VICs can respond to, and consequently remodel their surrounding ECM. This following section will focus on the interplay between pregnancy – a physiological state of volume overload – and the remodelling potential of the mitral valve as it adapts to its novel mechanical environment.

1.4 Cardiovascular Adaptations to Pregnancy

Pregnancy is characterized by a dramatic series of physiological changes that are required to efficiently deliver oxygen and nutrients to the developing fetus, accommodate the developing placenta, and meet the growing metabolic demands of the mother[140,141]. These changes are evident in maternal hemodynamics and cardiac structure. During pregnancy, heart rate and stroke volume (volume of blood expelled by a single ventricle per heartbeat) significantly increase by ~20% and ~30% respectively[140,142-147]. Combined with a decrease in systemic and pulmonary vascular resistance[140,142,144,146,148,149], this leads to an overall 30-50% increase in cardiac output (product of stroke volume and heart rate) for a singleton pregnancy[142-146,149]. Moreover, blood volume increases gradually over the course of gestation, increasing in excess of 40% by term. This increase in blood volume is the result of increased erythrocyte production and plasma volume, collectively leading to a state of volume overload on the heart[140,148,150-153]. All of these parameters are more pronounced in the case of twin pregnancies[154,155] and multiparity (repeated pregnancies)[156].

Volume overload, as we will see, is not unique to pregnancy. This hemodynamic state is present in other diseased states such as valve incompetence (inadequate leaflet coaptation) and heart failure[118,157]. With excess blood volume circulating through the mother and increased mitral valve flow velocities, diastolic filling of the left ventricle is enhanced and preload increases[158]. Through the Frank-Starling Law of the heart, increased preload increases myocardial stretch and thereby improves myocyte contractility from heartbeat to heartbeat. This early physiological compensatory response enables the maternal heart to efficiently oxygenate fetal and placental tissues, triggering more long-term myocardial remodelling.

The maternal heart physically responds to volume overload by increasing left ventricular mass through a process of eccentric hypertrophy[146,147,158,159]. This type of adaptive ventricular remodelling is shared with endurance athletes who similarly require increased preload and cardiac output to meet their heightened metabolic demands[113]. This process unfolds with left ventricular dilation (increased chamber volume) and a proportional increase in wall thickness to accommodate increased preload and diastolic

wall stress. The heart's hypertrophic response is a compensatory attempt to normalize wall stress via the law of Laplace for a thin-walled sphere (stress = (pressure × radius)/(2 × wall thickness))[158,160]. This is achieved by myocyte enlargement in both width and length through the addition of sarcomeres in parallel and in series, respectively[161]. Although some claim eccentric hypertrophy maintains the proportion between wall thickness and ventricular radius as mentioned above[160-162], others claim – and there is some evidence to show – there is a small propensity for the ventricle to preferentially dilate, causing a decline in this ratio[147,163]. A more recent study in 2015 sought to address these reported inconsistencies, and actually found an increase in relative wall thickness during pregnancy[164]. Despite this controversy, all in all, it is well agreed upon that such changes are viewed as an adaptive ventricular remodelling process to meet the changing hemodynamics (volume overload) of pregnancy with overall increases in left ventricular dimensions and mass. Indeed, left ventricular mass and wall thickness can increase in humans by an astounding 52% and 28% respectively, while end-systolic diameter and end-diastolic volume both increase by approximately 20% [142,158,165]. Importantly given the bovine model used herein, pregnant cattle experience similar cardiac expansion. By late pregnancy, bovine heart mass increases by 44%, and overall heart volume increases by nearly 50%[166].

Another important remodelling feature of pregnancy is an increase in mitral valve orifice area. Robson et al. (1989) showed that the mitral valve orifice area increases from 6.44 cm^2 preconception, to 7.22 cm^2 by the 36^{th} week of gestation[142], while others have shown increases in mitral annular diameter of up to 16% by term[167]. Although this annular dilation may seem trivial, small changes in orifice area and annular diameter can have significant impacts on leaflet and chordal stresses. According to the law of Laplace, an increased annular orifice will increase the radius of curvature of heart valve leaflets during closure, significantly increasing the mechanical stress experienced by the leaflet tissue and chordae tendineae as demonstrated through finite element analyses[168,169]. For example, an 18% increase in annular circumference results in a two-fold increase in anterior leaflet stress, and significant increases in both basal and marginal chordal stresses[168]. Heart simulators capable of reproducing physiological conditions and manipulating annular diameter have also showed significant increases in chordal force

with annular dilation[170]. Although not documented explicitly in the literature, maternal annular shape and papillary muscle geometry would likely change in tandem with left ventricular dilation[171], yielding other potential sources of increased mechanical stress on valve leaflets and chordae that, along with the known hemodynamic stresses, could stimulate additional valve remodelling.

In summary, pregnancy is a volume overload state that triggers profound remodelling of the cardiovascular tissues. The relatively early changes in hemodynamics that occur within the first few weeks of pregnancy, stimulate a wave of physical changes to the myocardium (eccentric ventricular hypertrophy), as well as to the valve apparatus (annular dilation) that occur much later at 12 weeks and beyond[143,167]. Together, such extreme changes in cardiac function and structure inevitably increase cardiovascular complications during the gestational period, and can exacerbate or unmask the effects of pre-existing conditions including valve stenosis and regurgitation[172]. These complications can jeopardize maternal and fetal health, the effects of which can continue post-partum [173]. As we will see, there is still much to be known about the physiological changes that occur during pregnancy; the valve tissue itself has astounding remodelling potential yet to be investigated.

1.5 Cardiac Remodelling – Pathological vs Physiological (Pregnancy)

Heart failure is characterized by a disabling loss of functional myocardium, such that its cardiac output is no longer sufficient to meet the body's metabolic demands[157]. Heart failure can develop from a variety of different cardiac issues including myocardial infarction, valve incompetencies, hypertension, and even diabetes[157,174]. The prevalence of cardiovascular disease and heart failure is astounding, collectively killing more people globally than any other illness[175]. With an ageing population in North America, the prevalence of heart failure and its associated health care costs are expected to worsen in the near future. In the United States alone, over 8 million people (1 in every 33) are expected to suffer from heart failure by the year 2030, with medical costs predicated to rise by nearly $50 billion[176].

Heart failure, regardless of the original etiology, results in a volume overload state whereby the body attempts to compensate for decreased ventricular function by increasing preload. Consequently, much of the structural remodelling stimulated by hypervolemia that occurs in heart failure mimics that of pregnancy, namely left ventricular and mitral annular dilation[177]. Another common valvular pathology that results in volume overload is mitral regurgitation, and again, the initial compensatory remodelling response is the same[118]. Over time however in both diseased states, the initial adaptive feedback wans and is replaced by a decompensated phase marked by a vicious deteriorative cycle of remodelling. The chamber and annulus continue to enlarge, intensifying the existing volume overload which then begets further valve and ventricular remodelling[178]. The myocardium eventually becomes fibrotic and loses contractile power and synchrony, leaving the patient with a grave prognosis from this point onward[118,157].

Pregnancy, although similar in its volume overload compensatory phase, ultimately lacks the deteriorative cycle that characterizes heart failure and mitral regurgitation. Somehow, these remodelling pathways diverge (Figure 1.10). If the increase in mechanical stress is mediated via similar volume overload mechanisms, why then, does one sequence remodel adaptively and preserve cardiac function, whilst the other progressively deteriorates towards total heart failure? Although this distinction is becoming clear regarding ventricular hypertrophy through studies on specific molecular pathways[179], this question currently remains unanswered for heart valves and requires a deeper understanding of physiological mitral valve remodelling. Maternal cardiovascular research may hold the key in differentiating between the physiological and the pathological.

An intriguing observation distinguishing pregnancy and heart failure is the incidence of functional mitral regurgitation (regurgitation that occurs secondary to heart failure). This valve incompetency occurs in over 50% of heart failure patients presenting with dilated cardiomyopathies, decreasing their chance of survival significantly[180-182]. Moreover, the mitral valves taken from these patients are mechanically, morphologically, and biochemically compromised. For example, in heart failure, the gross structure and composition of the mitral valve change significantly with an increase in leaflet area and thickness, collagen synthesis and GAG content, along with a decline in water content[123].

These remodelling events contribute to pathological stiffening and a decrease in the viscous properties of the valvular tissue[124].

Despite being in a state of volume overload, clinically significant mitral regurgitation in pregnancy is rare[183,184], and as discussed, does not induce ventricular or mitral valve failure. Even when compared to its counterpart the tricuspid valve, the mitral valve in pregnancy seems astoundingly resilient. Campos et al. (1993) used serial clinical and pulsed-continuous Doppler echocardiographic examinations on 18 pregnant women to determine the prevalence of valvular regurgitation. At full-term, mitral regurgitation was found in only 28% of women, while nearly 95% displayed regurgitant flow through their tricuspid valve[167]. Similarly, a study by Robson et al. (1992) showed that there is no significant increase in left side regurgitation in pregnancy compared to non-pregnant controls; however, regurgitation on the right, lower pressure side of the heart increases by 25% and 46% for the tricuspid and pulmonary valves respectively[185]. Together, these results suggest the mitral valve, despite being under higher transvalvular pressures, is structurally more adaptive and able to tolerate the hemodynamic changes associated with pregnancy compared not only to pathology, but also to valves on the right side of the heart – but why?

1.6 Maternal Mitral Valve Remodelling

Until recently, adult heart valves were thought to be static structures incapable of responding to changes in hemodynamic conditions in a non-pathological setting, i.e. maternal heart valves had no adaptive remodelling capability beyond routine reparative maintenance. This paradigm has now been shifted in light of new evidence that reveals a remarkable capacity for the mitral valve to remodel during pregnancy[166,186,187]. This recent work revolutionizes the current understanding of mitral valve physiology, showing the maternal mitral valve is a dynamic structure that undergoes significant morphological, structural, and biomechanical transformation. The shear novelty of this discovery means there is a profound lack of knowledge surrounding the adaptive remodelling capacity of maternal cardiovascular tissues. The initial study by Wells et al.[166] established a bovine pregnancy model to assess the morphological, structural, histological, and mechanical

changes associated with gestational volume loading and cardiac enlargement on the anterior mitral valve leaflet. Biaxial mechanical testing revealed a biphasic shift in leaflet extensibility; during early pregnancy the leaflet became 30% less extensible, then returned to pre-pregnant values later in gestation[166]. Collagen crimp length increased by an astounding 186%, leading to a 43% decrease in percent crimp area in pregnant animals[187]. Evidence for collagen remodelling was further supported by a 2°C decrease in its denaturation temperature and a significant increase in collagen cross-linking in pregnant animals as measured by HIT analysis[166].

Striking changes were also found following a thorough morphometric analysis of the bovine mitral valve. In pregnant cows there was a 33% increase in mitral anterior leaflet area, ***accompanied by a 22% increase in the number of chordae tendineae attachments to its ventricular surface*** (Figure 1.9). This appeared as a progressive, linear increase in chordae number as gestation advanced. Interestingly, the increase in leaflet area occurred at a different pace than did the increase in chordae, as evidenced by a decrease in chordal density[166]. Such an increase in chordae number has never before been documented in a mature mitral valve – pathological or otherwise.

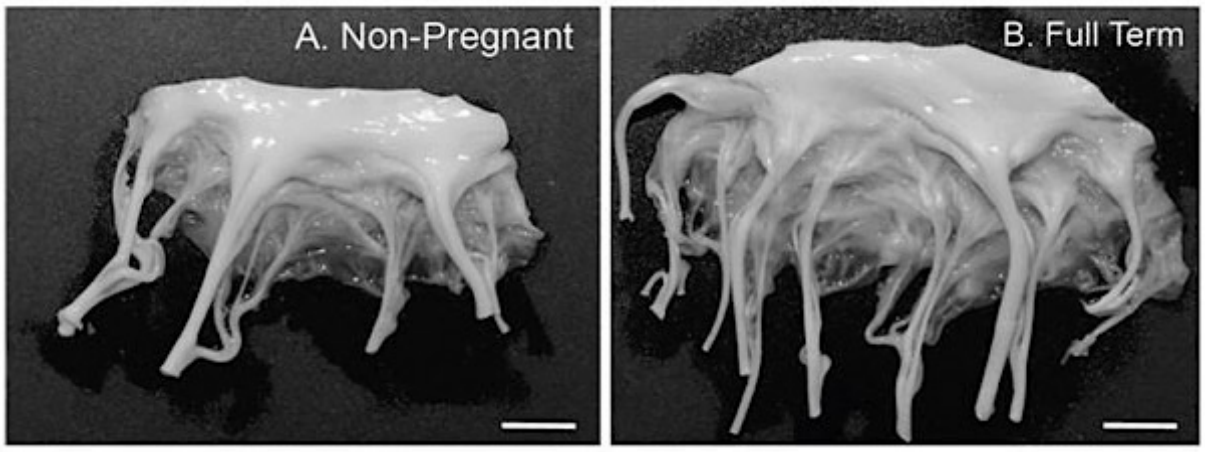

Figure 1.9: The mitral valve anterior leaflet in a non- pregnant heifer (A) and pregnant cow (B). A remarkable increase in leaflet area and number of chordae tendineae attachments can be seen in the full term mitral valve. Scale bars = 1 cm. Modified from Wells et al. (2012) [166].

Follow-up studies by Pierlot et al.[186,187] have further substantiated the tremendous changes in collagen architecture with pregnancy. Both collagen content and concentration

increased, suggesting the presence of newly synthesized collagen in the leaflet tissue, and fiber alignment decreased by 17%. Importantly, the fibrosa (the layer with which the chordae are continuous) was 53% thicker in pregnant cows. Collectively, these studies provided the first ever documentation of mitral valve remodelling during pregnancy – or indeed, in any non-pathological adult state. These structural and biomechanical adaptations are conceivably responsible for maintaining maternal mitral valve competence in the face of intensified hemodynamic and cardiac demand. A comparison of pregnancy and pathology-induced mitral valve remodelling is shown in Figure 1.10.

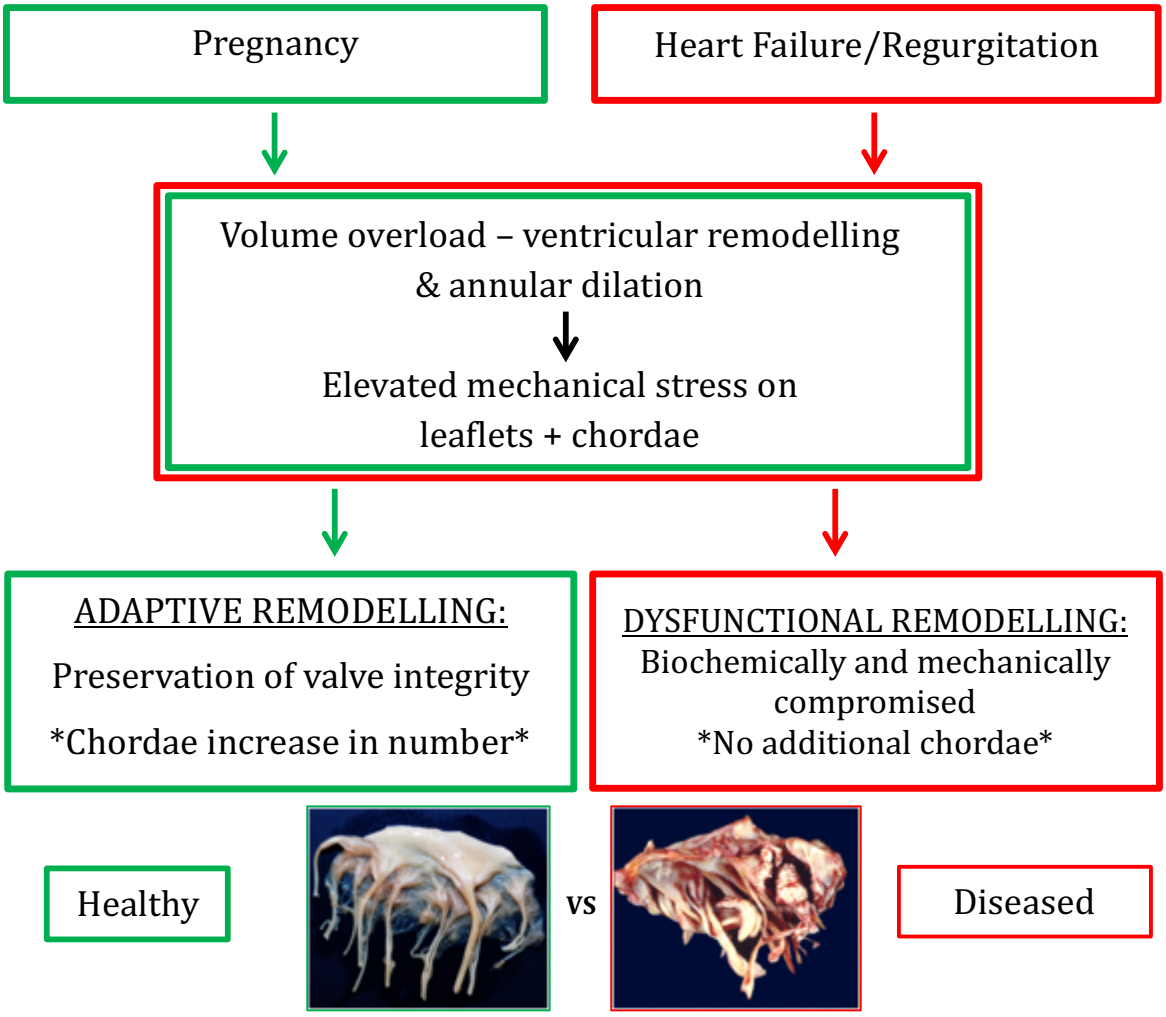

Figure 1.10: An overview of cardiac remodelling in pregnancy and pathology (heart failure and mitral regurgitation). Pregnancy and pathology share a hypervolemic state that initiates ventricular and annular dilation. These remodelling events elevate the mechanical stress experienced by the mitral leaflets and chordae, to which pregnancy and pathology respond uniquely. Dysfunctional remodelling occurs in pathology, leading to a biochemically and mechanically compromised valve with no additional chordae. Adaptive remodelling occurs in pregnancy with an increase in chordae number and a preservation of valve integrity. Heathy bovine mitral valve image (in pregnancy) taken by Caitlin Pierlot; diseased valve image taken from: http://www.slideshare.net/irheum/crystal-arthritis-amh.

Chapter 2
Thesis rationale, objectives, & hypotheses

2.1 **Overview**

Although many of the initial mechanical stimuli and remodelling events are shared between pregnancy and pathology, one extraordinary distinction is the increase in chordae number that occurs throughout pregnancy. This phenomenon has never been documented in a pathological valve, and granted, may be a vital compensatory mechanism by which dysfunctional and adaptive remodelling are distinguished. Indeed, uncompensated deficiencies in chordal branching are believed to leave the leaflet core relatively unsupported and vulnerable to mitral valve prolapse[70]. Increases in leaflet area (as observed in some pathologies) lacking a complimentary increase in chordae number may therefore jeopardize valve integrity and facilitate degenerative processes as the static chordae population must now endure heightened tensile loads. Reasonably, an investigation into chordae multiplication is well warranted.

Being physical extensions of the mitral leaflet itself, maternal increases in leaflet area and stress would necessarily elevate chordal stresses. Given the mechanical burden and known increase in chordae number, it stands to reason that maternal chordae tendineae are actively remodelling in response to the novel hemodynamic environment associated with pregnancy. This, combined with preliminary work describing a decrease in collagen denaturation temperature with an associative increase in chordal diameter during pregnancy[188,189], collectively suggest that chordae tendineae are also remodelling during pregnancy, and that ***chordae increase in number via the splitting of existing tendons***.

Establishing chordae as actively remodelling structures similar to the mitral valve anterior leaflet (e.g. with respect to collagen architecture) is a strong stepping-stone

towards understanding how the chordae increase in number throughout pregnancy. ***The overarching objective of this thesis work was to determine the mechanisms by which maternal bovine chordae tendineae remodel.*** This was achieved through a spatial (papillary muscle to leaflet) assessment of maternal chordae in comparison to non-pregnant controls (heifers). A series of thermal, histological, and immunological experiments were performed to probe for evidence of chordae remodelling. The remodelling evidence collected herein will be discussed in light of the chordal splitting concept as an explanation for the maternal increase in chordae number; we hypothesize that chordal splitting initiates at the leaflet insertion sites as the mitral leaflet expands during pregnancy, and propagates down the chordal length.

2.2 Experiment 1: Chordae Counting

Rationale: Only once has a maternal increase in chordae number been documented[166]. The foundations of this thesis are based upon this concept, and therefore, it requires thorough validation from a secondary observer.

Objective: To verify the maternal increase in chordae number documented previously[166].

Hypothesis: Counting was previously performed based upon chordal diameter, excluding the smallest side branches and any translucent chordae. Herein, *all* chordae will be counted based on type (i.e. basal, marginal, strut), with an expected increase in both marginal and basal chordae as the gestational period progresses.

2.3 Experiment 2: Collagen Thermal Properties

Rationale: Collagen is the primary mechanical component in chordae, allowing it to bear and endure high cycle fatigue loading without failure. Decreases in the thermal stability of this collagenous network can be indicative of collagen remodelling and turnover within the tissue, as seen in previous heart valve studies[45,49].

Objective: To quantify the thermal properties of chordae collagen between heifer and maternal chordae.

Hypothesis: In accordance with other actively remodelling cardiovascular tissues[45,49,166] and with regards to the polymer-in-a-box theory of collagen molecular packing[47], there will be a general decrease in collagen thermal stability. The distribution of thermal stabilities will increase in maternal chordae as a greater population of collagen molecules with relatively low thermal stability is introduced (due to more active collagen turnover).

2.4 **Experiment 3: Collagen Crimp**

Rationale: The crimp length of collagen fibers contributes heavily towards bulk tissue extensibility. In the maternal mitral valve anterior leaflet, crimp length increased by 186% in pregnant animals, with a coinciding 45% decrease in the percentage of leaflet area occupied by crimped tissue[186]. This drastic expansive remodelling suggested an overall lengthening of the leaflet's collagen architecture. As left ventricular dimensions increase in pregnancy, the chordae themselves may also be lengthening and therefore a similar collagen remodelling process may be occurring.

Objective: To quantitatively evaluate changes in crimp length and percent crimp area in chordae between pregnant and non-pregnant animals.

Hypothesis: Given the annular and ventricular remodelling known to occur during pregnancy[142,143,158] and the resulting increase in mechanical stress experienced by the valve tissue[168], chordae in pregnant cows are predicted to remodel in a similar fashion to that of the anterior leaflet: chordae crimp length will increase and percent crimp area will decrease. Additionally, there will be a strong presence of localized, disordered collagen at chordae bifurcations and leaflet insertion sites from pregnant animals as a sign of chordal remodelling.

2.5 Experiment 4: General ECM Histology

Rationale: Under pathological conditions, the ECM composition and tri-layered structure of the mitral valve leaflet can be severely altered under abnormal loading conditions[22,190]. Since the synthesis of ECM components is mechanosensitive, it is likely that there will be a change in the relative quantities of these molecules in the presence of novel hemodynamics and increased mechanical stress as observed in pregnancy. Moreover, proteoglycans and GAGs can influence collagen fibrillogenesis, assembly, and interfibrillar spacing, and function in cellular communication[8,191-194], which would most certainly have implications for chordae remodelling.

Objective: To qualitatively visualize key ECM components (elastin, collagen, GAGs) and cell nuclei for a structural signature of maternal chordae remodelling and/or chordae splitting.

Hypothesis: Chordae bifurcations in pregnant animals are sites of active ECM remodelling and will therefore show an increase in the number of VICs (cell nuclei) and GAGs. As previously described in non-bovine chordae, elastin will be localized to the outer chordal layer in both pregnant and non-pregnant animals, with minimal fibers present within the tissue bulk[52].

2.6 Experiment 5: Immunohistochemistry (α-SMA & Periostin)

Rationale: Immunohistochemistry can reveal important information on cell phenotype and protein expression not captured using general histological stains. In diseased and fetal valves – both actively remodelling tissue – the percentage of aVICs increases significantly, contributing towards extensive structural and compositional changes in the valve tissue[99,101,133,195]. However, the maternal bovine anterior leaflet actually sees a decrease in VIC activation[196]. This experiment will be beneficial in determining whether maternal chordae, which are subject to elevated stress and potentially in the process of splitting, will respond in a similar fashion to the maternal leaflet (no change or a decrease

in VIC activation), or if they will uniquely have more in common with fetal valves (increase in aVICs).

Periostin is a matricellular protein that mediates a wide variety of cell-matrix interactions in cardiac development, wound healing, and disease[197-200]. Periostin is intensely expressed in the chordae tendineae during fetal valve formation, and persists into mature adult tissues[198,201]. Reasonably, as the chordae are made primarily of collagen, periostin is able to directly bind to collagen type I and regulate fibril assembly and cross-linking[202]. Perhaps most importantly for this work, periostin has been deemed crucial for the process of healthy chordae branching throughout fetal development[201]. The re-initiation of chordae multiplication in a mature, adult valve could be the result of elevated baseline periostin expression during pregnancy. An upregulation of this protein in maternal chordae would be strong evidence to support active remodelling of the chordae network.

Objectives:

(i) To detect possible phenotypic changes in VICs in chordae from pregnant cows.
(ii) To determine if maternal chordae remodelling recapitulates fetal remodelling with respect to chordae branching and upregulated periostin expression.

Hypotheses:

(i) Chordae immunostained from pregnant cows will show a global increase in the percentage of aVICs compared to heifers, similar to what is observed in fetal valves where chordae also increase in number. More specifically, aVICs will be most abundant at maternal bifurcations.

(ii) Periostin expression will be upregulated in pregnancy adjacent to maternal bifurcations where chordae splitting is believed to be occurring; heifers will show a more homogeneous periostin expression.

Chapter 3
Materials & Methods

3.1 Tissue Collection

Hearts from never-pregnant, sexually mature female cattle (heifers; 18-30 months) and pregnant cows (18-36 months) were collected fresh from slaughter at a local abattoir (Reid's Meats, Wolfville, Nova Scotia, Canada). Pregnant cattle undergo similar cardiac and hemodynamic adaptations as humans, including blood volume expansion[203] and myocardial remodelling[166,204]. Importantly, their gestational timeframe and habitual singleton pregnancies are also similar to that of humans, making cattle a suitable pregnancy model. The gestational age of pregnant cows was determined using fetal crown-to-rump length (CRL) according to the following formula[205]:

$$\text{Gestational Day} = 8.4 + 0.87(\text{CRL}) + 5.46(\text{CRL})^{1/2}$$

Hearts were transported back to the laboratory in a chilled cooler where the mitral valve anterior leaflet, associated chordae tendineae, and papillary muscles were excised. Valves were then placed between two layers of cheesecloth moistened with Hank's physiological saline solution, double bagged, and stored at -86°C. The University Committee on Laboratory Animals at Dalhousie University approved the harvesting protocol of all experimental tissue.

3.2 Chordae Counting

Preceding storage at -86°C, the number of chordal attachments to the anterior mitral valve leaflet was counted for all harvested valves (n=20 heifers; n=24 pregnant). Gestational ages ranged from approximately 27 to 249 days, corresponding to a fetal length range of 1-89 cm. Chordae were classified as one of three types: strut, basal, or

marginal. By definition, strut chordae are the two largest chordae that insert into the anterior leaflet at approximately the 4 and 8 o'clock positions, most proximal to the annulus[62]. With every valve (both pregnant and non-pregnant) containing two prominent struts, chordae of this type were not relevant to the chordae counting analysis; only very rarely are these chordae not easily identified and paired. The strut chordae were therefore not individually compared between pregnancy groups, and were only included in the total chordae counts. Marginal chordae were defined as any chordae attached to and continuous with the anterior leaflet free edge (frequently appearing translucent), while basal chordae included all remaining chordae attached to the main belly of the anterior leaflet, not classified under the strut or marginal definitions. Each unique attachment into the leaflet (irrespective of its papillary muscle origin) was counted as a single chorda. During the counting procedure, anterior leaflets and associated papillary muscles were pinned to a dissection tray to help spread and visualize the chordae. All tissue structures were kept moist with Hank's physiological saline solution.

3.3 Differential Scanning Calorimetry (DSC)

Frozen mitral valves from heifers and pregnant cows were left to thaw at room temperature in their sealed bags. Valves were subsequently pinned to a dissection tray via the anterior leaflet and papillary muscles, allowing the chordae to become taut. Pinning the valves in this manner generated adequate tension that helped to separate and visualize all valve chordae for sample collection. Samples were collected based on chordae type (strut, basal, marginal) and by specific locations along their length: 1) Bifurcations – where one chorda splits into one or more branches; 2) insertion sites – where the chorda merges with the anterior leaflet; and 3) straight "control" segments (i.e., not bifurcations or leaflet insertion sites). An illustration of the overall sampling method and examples of these harvesting locations are provided in Figure 3.3 and Figure 3.1 respectively. A total of 7 heifer valves (18-30 months old) and 6 late pregnant maternal valves (18-30 months old; approximately 218-231 days gestation) were used. Straight segments were harvested a minimum distance of 1 cm from chordae bifurcations and leaflet insertion sites. Each bifurcation and straight segment sample had its distance from the leaflet surface

measured by following the longest chorda back to its leaflet attachment point (Figure 3.1). Multiple samples (typically between 2-4, dependent upon maximum number of viable samples harvestable from the valve for DSC) of each chordae type and location (e.g., more than one strut bifurcation) were harvested from a single valve; the data obtained for repeated samples were averaged to give a single data point for each combination of chordae type and location per valve.

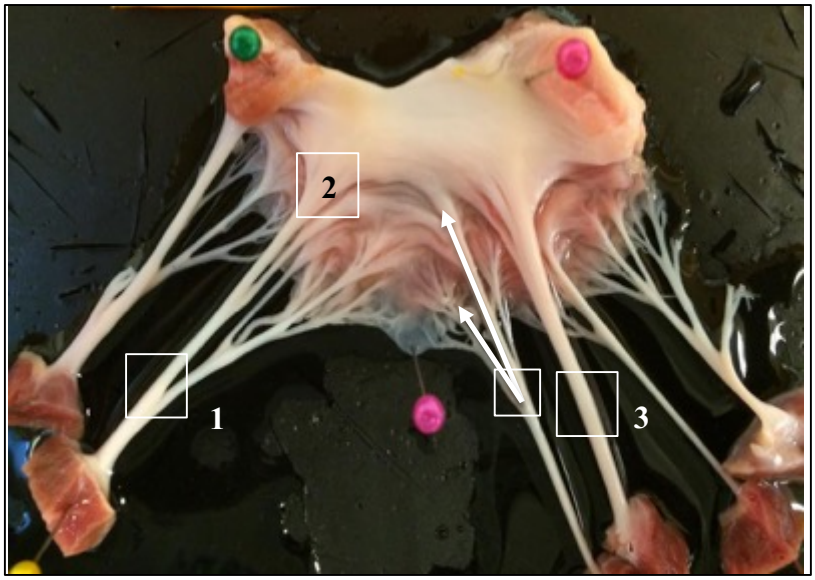

Figure 3.1: Excised bovine mitral valve anterior leaflet showing examples of the sampling locations for differential scanning calorimetry and bifurcation distance measurements. Sampling locations: (1) bifurcation, (2) leaflet insertion site, and (3) straight segments. White arrows originate at a single bifurcation sample and follow both branches towards their leaflet attachment point; the longest distance from the bifurcation was used as that bifurcation's distance from the leaflet.

DSC was performed using a Q200 differential scanning calorimeter (TA Instruments, New Castle, DE) initially calibrated with an Indium standard. Chordae samples were weighed following the removal of excess surface water by gentle blotting, then hermetically sealed into aluminum DSC pans. All samples were equilibrated to 20°C, ramped to 85°C at 5°C/min, and run against an empty aluminum reference pan. Data were recorded at 10 Hz, with the resulting endotherms being analyzed using Universal Analysis 2000 software (version 4.5A, TA Instruments). The parameters of interest included: onset temperature (T_{onset}), peak temperature (T_{peak}), full width at half

maximum (FWHM), and specific enthalpy. T_{onset} is the temperature at which the least thermally stable collagen molecules within the sample begin to denature, calculated as the intersection between the endotherm's baseline and a tangent line drawn to the endotherm's downward slope. T_{peak} is defined as the temperature of maximum heat flow into the sample, where the majority of collagen molecules are uncoiling. The FWHM describes the distribution of thermal stabilities in the sample (e.g. a chordae sample yielding an endotherm with a larger FWHM has a broader range of collagen thermal stabilities). The FWHM was calculated as the difference in temperatures where the heat flow on the downward and upward slopes of the endotherm were equivalent, at half the maximum heat flow into the sample extrapolated from baseline. The specific enthalpy is defined as the total energy required for sample denaturation and was calculated by measuring the area under the DSC endotherm (using sample wet weight). A generic endotherm with parameter labels is provided in Figure 3.2.

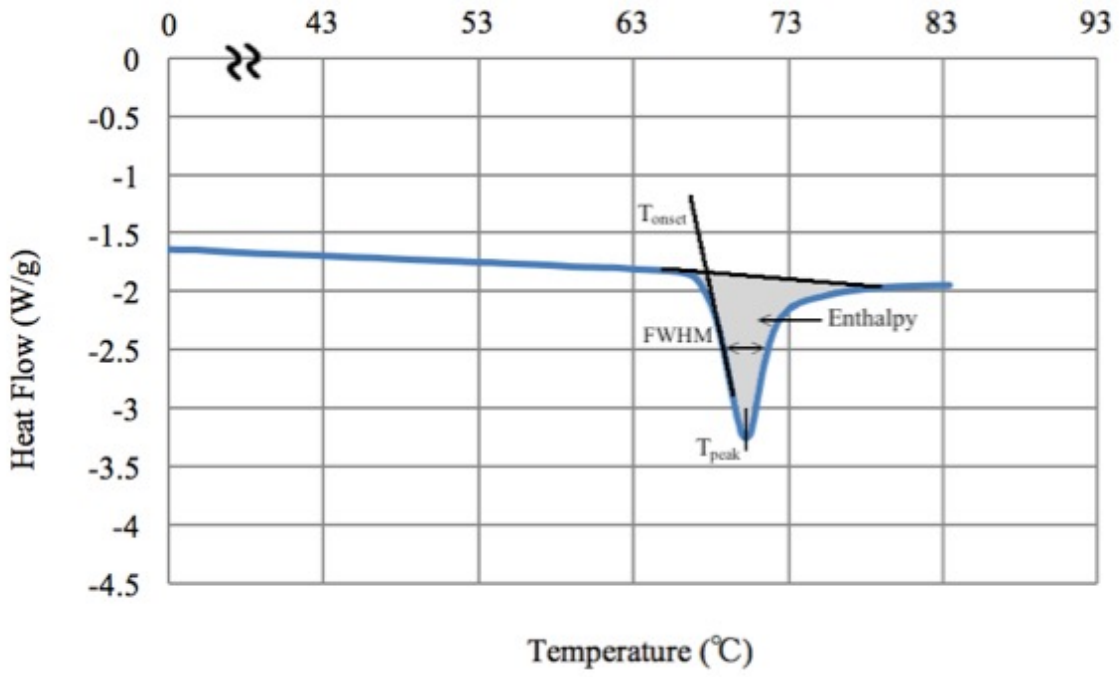

Figure 3.2: Differential scanning calorimetry endotherm of a bovine chorda showing the four parameters of interest: The temperature of onset (T_{onset}), peak temperature (T_{peak}), the full width at half maximum (FWHM), and the specific enthalpy.

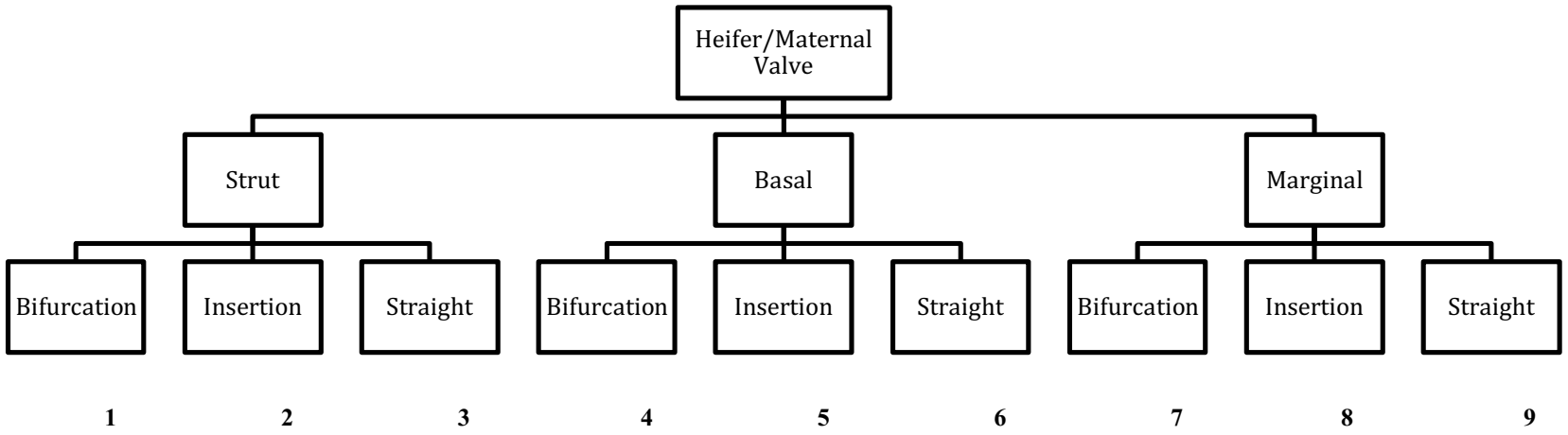

Figure 3.3: Sampling protocol for differential scanning calorimetry. From each heifer and maternal valve, 3 types of chordae were collected: strut, basal, and marginal. For each type of chorda collected there were also 3 sampling locations: bifurcations, insertions, and straight segments. Multiple samples of the same chordae type and location (e.g. more than one strut bifurcation) were harvested for each valve. The data obtained for repeated samples were averaged giving a single data point for each combination of chordae type and location, giving a total of 9 data points per valve.

3.4 Histology

Mitral valve anterior leaflets from heifers (n=4) and pregnant (n=4) animals (gestational ages of approximately 88, 194, 202, and 229 days) were cut in half with a scalpel between the strut chordae from the annular attachment to the free edge, allowing them to fit neatly into large histology cassettes for tissue fixation. The leaflet tissue, all associated chordae tendineae, and papillary muscles from each half-valve were then fixed for 6 days in 10% neutral buffered formalin. Following fixation, chordae of each type (strut, basal, marginal) capturing bifurcations, straight segments, and leaflet insertion sites were dissected, placed in individual tissue cassettes, and stored in 70% ethanol until paraffin embedding. An average of 9 unique chordae samples from heifer valves and 10 unique samples from maternal valves were taken and therefore a grand total of 35 non-pregnant [(4 valves) x (~9 sample regions per valve)] and 39 pregnant [(4 valves) x (~10 sample regions per valve)] distinct chordae regions were assessed for each histological approach outlined below. Each bifurcation sample had its distance from the leaflet surface measured by following the longest chorda back to its leaflet attachment point (as described above in the DSC protocol). Chordae tissue was serially sectioned longitudinally into 5μm sections, mounted on charged slides (25x75x1mm, Globe Scientific, Inc.), and dried at 57°C for a minimum of 24 hours prior to deparaffinization and subsequent staining. Embedding and sectioning were performed by the Histology Research Services Laboratory (Faculty of Medicine, Dalhousie University).

3.4.1 Picrosirius Red

Chordae collagen crimp was enhanced by staining slides with Picrosirius Red. Slides were first deparaffinized with 4 xylene rinses lasting 5 minutes each, then rehydrated using a series of 5 minute washes in graded ethanol solutions: 3 washes at 100%, 2 washes at 95%, and 2 washes at 70%, followed by a final rinse in tap water. Direct Red 80 (Sigma-Aldrich) and saturated picric acid (Sigma-Aldrich) were used to prepare a 0.1% Picrosirius Red solution that was then applied to the slides for 1 hour while shielded from light. After 1 hour slides were rinsed in 0.5% acetic acid followed by

a brief rinse in tap water. Slides were then dehydrated once again in a series of graded ethanol solutions, and cleared with 20 dips in each of 4 xylene baths. Glass coverslips (24x60mm, VWR) were secured with mounting media (Cytoseal XYL, Thermo Scientific) and left to adhere for 24 hours in a fume hood.

3.4.2 Movat Pentachrome

Extracellular matrix components (collagen, elastin, GAGs) and cell nuclei were revealed using a Russell-Movat Pentachrome Stain Kit (American MasterTech, Lodi, California). Slides were first deparaffinized with 4 xylene rinses lasting 5 minutes each, then rehydrated using a series of 5 minute washes in graded ethanol solutions: 3 washes at 100%, 2 washes at 95%, and 2 washes at 70%, followed by a final rinse in tap water. Slides were then placed in distilled water for 5 minutes, during which time a fresh solution of Verhoeff's Elastic Stain was prepared using equal parts Universal Iodine Solution^{TM}, 10% ferric chloride, 10% alcoholic hematoxylin, and 100% ethanol. Slides were left in the Verhoeff's solution for 20 minutes concealed from light, and then rinsed in lukewarm running tap water for 5 minutes, followed by a brief rinse with distilled water. Slides were differentiated using a direct application of 2% ferric chloride until elastic fibers were sharply defined (verified using light microscopy), rinsed with distilled water, and placed in sodium thiosulfate for 1 minute. After a 5-minute tap water rinse and a 3-minute application of 3% acetic acid, slides were placed directly into a 1% Alcian Blue solution for 30 minutes. Warm running tap water was used to wash the slides for 1 minute, followed by another rinse with distilled water. The slides were then stained with Crocein Scarlet – Acid Fuchsin for 2 minutes, rinsed through 3 changes of distilled water, and dipped 5 times in 1% acetic acid before differentiation with 2 changes of phosphotungstic acid (5 minutes each). Slides were dipped 5 more times in 1% acetic acid, dehydrated through 3 changes of fresh 100% ethanol, and placed in Alcoholic Saffron Solution for 15 minutes. Once removed, slides were dehydrated once more through 3 changes of 100% ethanol, cleared through 3 changes of fresh xylene, and mounted (Cytoseal XYL, Thermo Scientific) with glass coverslips (24x60mm, VWR).

Slides were imaged using a Nikon Eclipse E600 light microscope equipped with a polarized light filter and 10 MP AmScope digital camera.

3.4.3 Immunostaining (α-SMA)

Slides were deparaffinized and hydrated following the same protocol outlined for Picrosirius Red (above). To recover any compromised antigenicity of α-SMA due to the formalin-based fixation, the tissue was pretreated with heat-induced epitope retrieval. The formation of formalin-protein crosslinks, which can modify the molecular confirmation of proteins and ultimately mask target antigens, can be reversed using high temperature heating and/or strong alkaline buffers[206-209]. It was discovered that superheating (124.5°C for 30 seconds) chordae slides with tris-ethylenediaminetetraacetic acid (tris-EDTA) at pH 9 destroyed tissue morphology and therefore the water bath was henceforth maintained at 80°C for 50 minutes, following the inverse relationship observed between antigen retrieval temperature and time[208-210] frequently used on tissue slides prone to dissociation under intense heat[211,212].

Immunohistochemistry was carried out using the labeled streptavidin-biotin method (LSAB+System-HRP, Dako, K0690). The hot buffer was gradually brought to room temperature with tap water before the slides were rinsed with phosphate buffered saline (PBS) and treated with 2% hydrogen peroxide to block endogenous peroxidases that can contribute to non-specific background staining. Slides were then rinsed in PBS and treated for 10 minutes with Serum-Free Ready-To-Use Protein Block (Dako, X0909) to prevent endogenous biotin protein from binding with later applications of the streptavidin-horseradish peroxidase (HRP) conjugate. The primary antibody (monoclonal mouse anti-human smooth muscle actin, M0851, Dako) diluted 1:200 in PBS was then applied and left to incubate for 30 minutes at room temperature, followed by two sequential 30-minute room temperature incubations of the secondary biotinylated antibody (Biotinylated Link Universal, Dako) and streptavidin-HRP (Dako) respectively. Visualization was achieved using a 7-minute application of diaminobenzidine (Liquid DAB+Substrate Chromogen System, Dako, K3468), and after a brief rinse in tap water, slides were finally counterstained using Mayer's hematoxylin solution (Sigma-Aldrich),

dipped in Scott's water, dehydrated through a graded series of ethanol solutions, cleared with xylene, and mounted (Cytoseal XYL, Thermo Scientific) with glass coverslips (24x60mm, VWR). Each run included a negative chorda control subjected to the same procedure outlined above, but lacking primary antibody.

3.4.4 Immunostaining (Periostin)

Slides were deparaffinized and hydrated following the same protocol outlined for Picrosirius Red (above). Slides were then rinsed with PBS and submerged in 2% hydrogen peroxide for 15 minutes to block endogenous peroxidases. After another wash in PBS, slides were treated for 10 minutes with Serum-Free Ready-To-Use Protein Block (Dako, X0909). Excess protein block was removed and slides were then incubated in primary antibody (polyclonal goat anti-human periostin (S-15): sc-49480, Santa Cruz Biotechnology, Inc.) diluted 1:200 in PBS overnight. The following day, slides were thoroughly rinsed in PBS and incubated for 1 hour with secondary polyclonal rabbit anti-goat-HRP (P0449, Dako). Slides were then rinsed in PBS, incubated for 3 minutes in DAB for visualization (Liquid DAB+Substrate Chromogen System, Dako, K3468), rinsed with tap water, counterstained with Mayer's hematoxylin solution (Sigma-Aldrich), and dipped in Scott's water for bluing. Slides were finally dehydrated through a graded series of ethanol solutions, cleared with xylene, and mounted (Cytoseal XYL, Thermo Scientific) with glass coverslips (24x60mm, VWR). Positive human placenta controls and negative chordae controls (omitting primary antibody) were included with each run. A Nikon Eclipse E600 light microscope and 10 MP AmScope digital camera were used to image all periostin slides.

3.4.5 Image Analysis – Movat Pentachrome

A semi-quantitative analysis classifying elastin morphologies at chordae bifurcations was conducted. Bifurcations were assigned a score from 0 to 3 with the following criteria: (0) No elastin present; (1) only small, fragmented elastic fibers present with no defined directionality; (2) elastin on one or both sides of the bifurcation had

begun extending longitudinally into the common trunk segment; and (3) elastin propagation from both sides of the bifurcation had joined below the bifurcation. Examples of each numerical score are provided in Figure 3.4.

3.4.6 Image Analysis – Collagen Crimp

Images of slides stained with Picrosirius Red were taken at 400x magnification using a Nikon Eclipse E600 light microscope equipped with a polarized light filter and 10 MP AmScope digital camera. Slides were analyzed for collagen crimp length (distance measurement of adjacent crimp peaks) and percent crimp area using open source ImageJ software (National Institute of Health) as described previously[186]. For both crimp length and percent crimp area, 5 consecutive images were taken running longitudinally along the length of each chorda (only straight segments were imaged, i.e. bifurcation and leaflet insertion site crimp were not quantitatively assessed). The distance between the chorda section being imaged and the leaflet surface was estimated using the pre-measured bifurcation distances (obtained from the original histological sample preparation) and step-wise field-of-view movements at 100x magnification (2.2 mm increments) from these bifurcation landmarks. For crimp length measurements, a line through the center and parallel with the principal crimp direction was placed over each image and each discernable peak-to-peak crimp length along this line was recorded. Crimp area was measured by placing a grid (600 μm^2/square) over each of the 5 images and grid points were counted (i) in contact with crimped tissue, (ii) uncrimped tissue, and (iii) empty space (the latter was omitted from the total grid count). The ratio of crimped grid points to the total grid count was used to calculate the percentage of crimped chordal area. Crimp length and percent crimp area measurements were averaged over all 5 images.

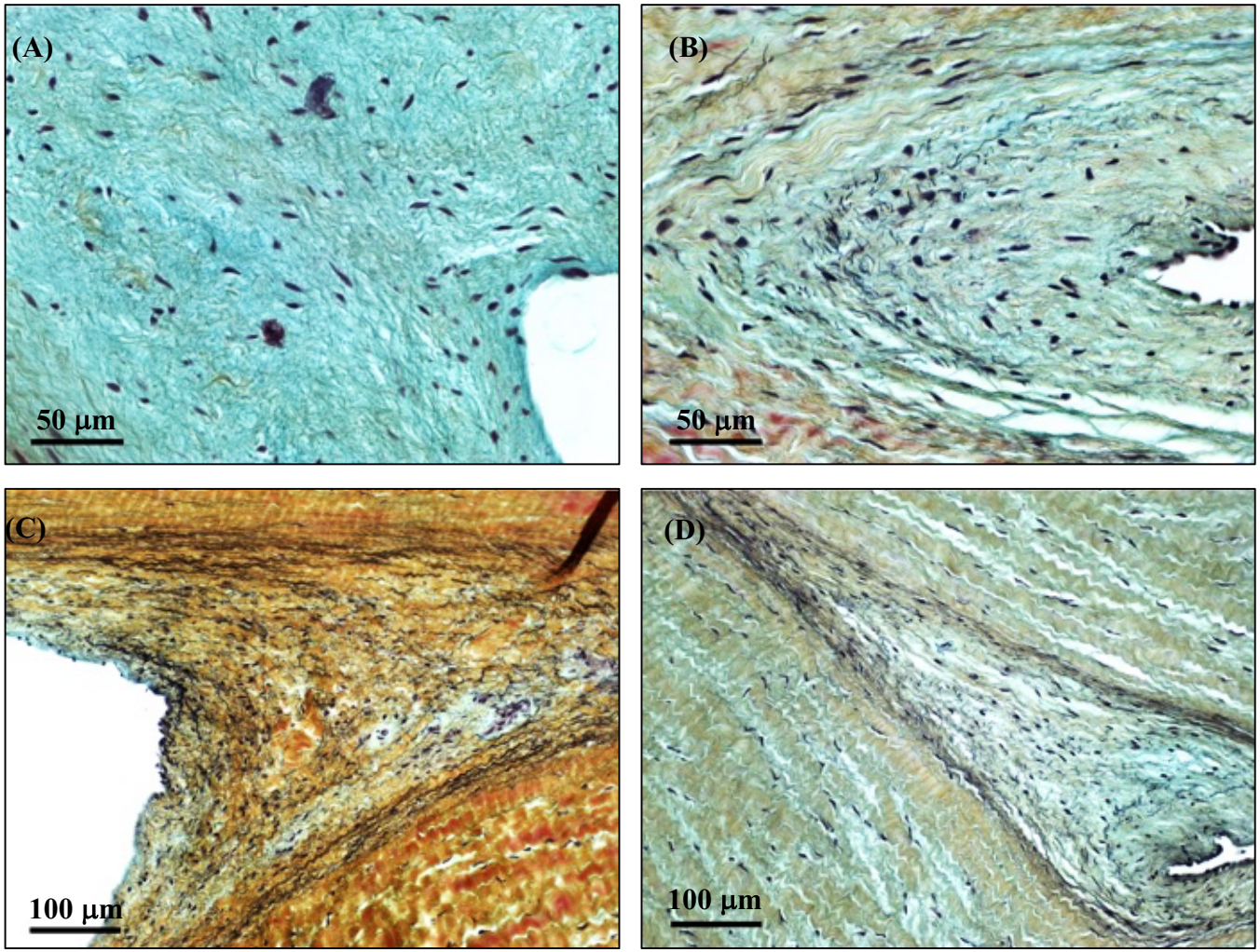

Figure 3.4: Movat Pentachrome-stained longitudinal section showing examples of characteristic elastin morphologies at chordae bifurcations and their corresponding semi-quantitative numerical scores. Letters A, B, C, and D correspond to numerical scores of 0, 1, 2, and 3 respectively. Yellow=collagen, blue/green=GAGs, black lines=elastin fibers, purple elongations/circles=cell nuclei

3.4.7 Image Analysis – α-SMA (Cell Phenotype & Density)

The presence of α-SMA positive VIC nuclei was assessed at chordae bifurcations and straight segments. One image at 400x magnification was taken at each bifurcation tip, with a total of 36 bifurcations from 3 heifer valves and 59 bifurcations from 3 maternal valves. Each image was taken such that the outside edge of the microscope's field of view was in-line with the bifurcation tip, maximizing the captured bifurcation area. Bifurcations frequently contained a considerable amount of empty white space (non-tissue); this area fraction was removed when calculating the number of cells per unit area. Straight segment images were also taken at 400x magnification, but at a distance of approximately 0.33cm (3 fields of view at 200x magnification) below the bifurcations in the center of the chordae tissue. In some cases, where collagen disruption was visible extending down from the bifurcation at 0.33 cm or beyond, an image was taken at the next nearest point where natural collagen crimp resumed. A total of 33 straight segment images from 3 heifer valves and 59 straight segments images from 3 maternal valves were taken. The Cell Count plug-in feature in ImageJ (National Institute of Health) was used to manually count and classify cell nuclei as either α-SMA positive (appear brown with DAB staining) or negative (appear purple/blue with hematoxylin counterstain) as seen in Figure 3.5. First, all nuclei in the image (positive *and* negatively stained cells) were selected and recorded under an arbitrary "Type 1 Counter" in ImageJ. Following this, a second "Type 2 Counter" was used to count and record α-SMA positive cells only. The ratio of positively stained cells to total cells was used to calculate the percentage of aVICs. All cell counting data obtained from bifurcations belonging to the same valve were averaged. This procedure was repeated for straight segments. All images were taken at 400x magnification using a Nikon Eclipse E600 light microscope equipped with a polarized light filter and 10 MP AmScope digital camera.

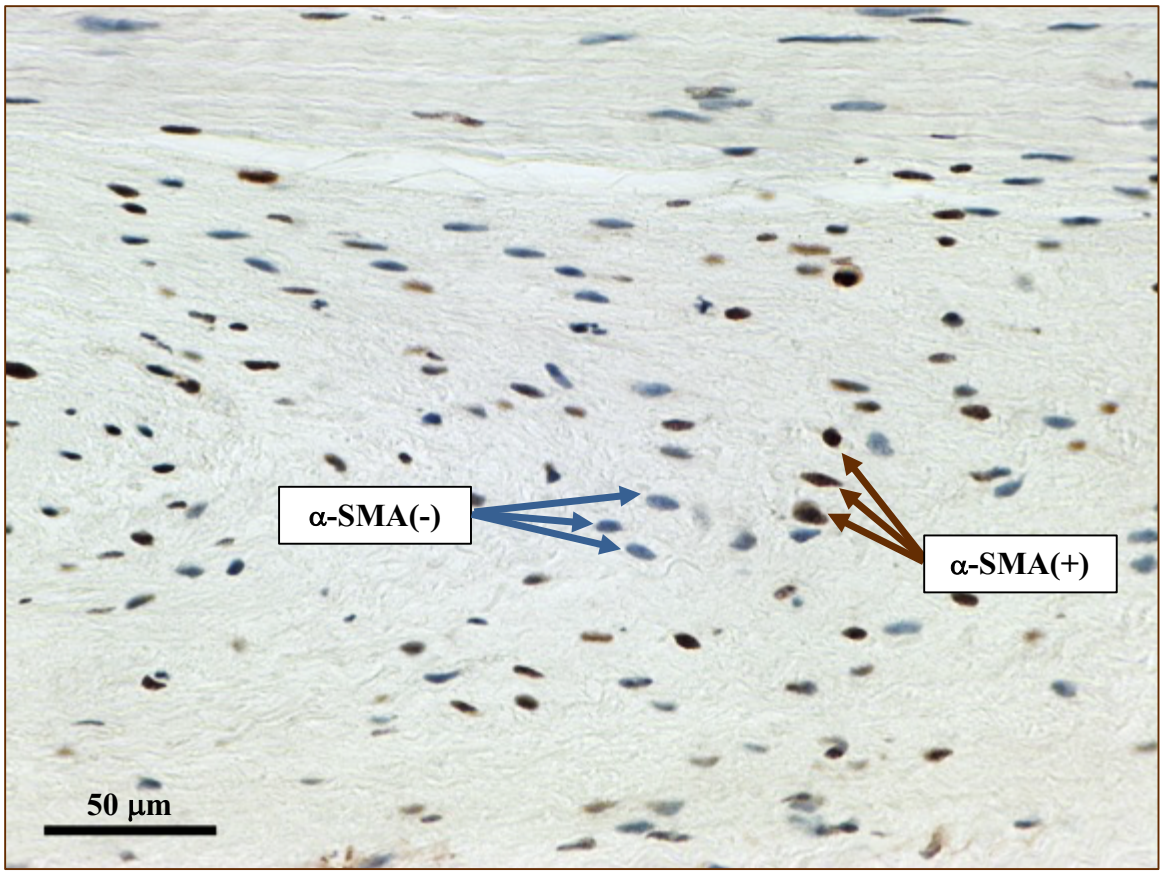

Figure 3.5: α-SMA immunostained longitudinal section of a bovine chorda showing valvular interstitial cell nuclei stained brown with DAB (α-SMA positive), and α-SMA negative cells counterstained blue/purple with hematoxylin. Two counter types were used to count and classify cell nuc1ei for cell density and phenotype measurements: Type I Counter was used to count all nuclei in the image and Type 2 Counter was used to exclusively count α-SMA positive cells.

3.5 Statistical Analyses

All statistical analyses were performed using JMP Software (Version 12.1.0) with *p*-values ≤0.05 considered statistically significant. Values are expressed as the mean ± standard error (SE). For chordae counting, *t*-tests were used to compare the means of basal, marginal, and total number of chordae between heifers and pregnant animals. The relationship between CRL and chordae number in pregnant cows for basal, marginal, and total chordae counts was evaluated using a least-squares linear regression and tested for significance using an ANOVA. Based on the protocol for DSC sample collection (i.e. by chordae type and location), multiple samples were harvested from each valve and

therefore a repeated measures full factorial (3-way ANOVA) was performed with sampling location and chordae type as the within-subject factors, and pregnancy state as the between-subject factor. This was followed by post-hoc Tukey honest significant difference testing. Values of T_{onset}, T_{peak}, FWHM, and specific enthalpy were plotted as a function of distance from the leaflet surface using a least-squares linear regression and were tested for significance with an ANOVA. Marginal chordae and leaflet insertions sites were excluded from the regression as insertion sites and marginal chordae samples were never harvested further than 1cm from the leaflet tissue and therefore an accurate survey of thermal stability variation with distance could not be obtained. A 2-way repeated measures ANOVA was conducted for chordae crimp measurements (crimp wavelength and percent crimp area) with pregnancy state and chordae type as the main effects of the model, and crimp wavelength was plotted against distance from the leaflet surface using a least-squares linear regression tested with an ANOVA. The same approach was used to test for differences in cell density and VIC activation, except location (bifurcations and straight segments) and pregnancy state were used as the main factors of the 2-way repeated measures ANOVA. Differences in elastin morphologies (classified using semi-quantitative categorical data) between non-pregnant and pregnant animals were tested for significance with a Chi-squared test.

Chapter 4
Results

4.1 The Number of Chordae Attachments Increases In Pregnancy

The number of basal, marginal, and total chordal attachments increased significantly in pregnant animals by 17%, 21%, and 18% respectively (Figure 4.1). As seen in Figure 4.2-Figure 4.4, there was no relationship between maternal chordae number and pregnancy duration (based on fetal CRL).

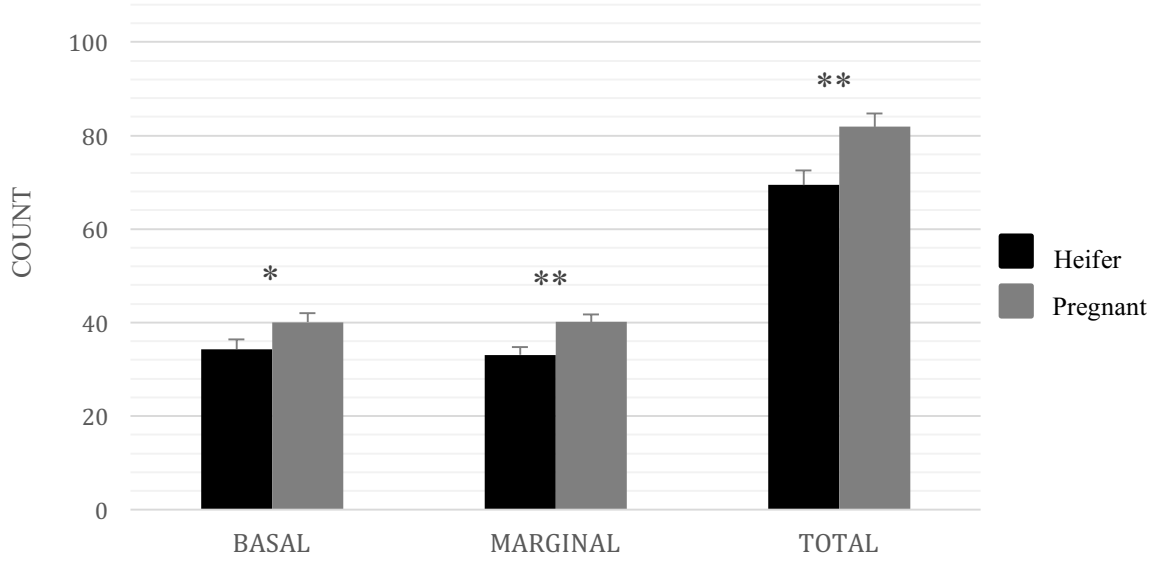

Figure 4.1: Number of basal, marginal, and total chordal attachments to the anterior mitral valve leaflet in non-pregnant heifers (n=20 valves) and pregnant cows (n=24 valves). Total chordae number is the sum of all basal and marginal chordae, with the addition of two strut chordae (as each valve always contains only two struts). Values are shown as the mean ± SE. *=p<0.05, **=p<0.006.

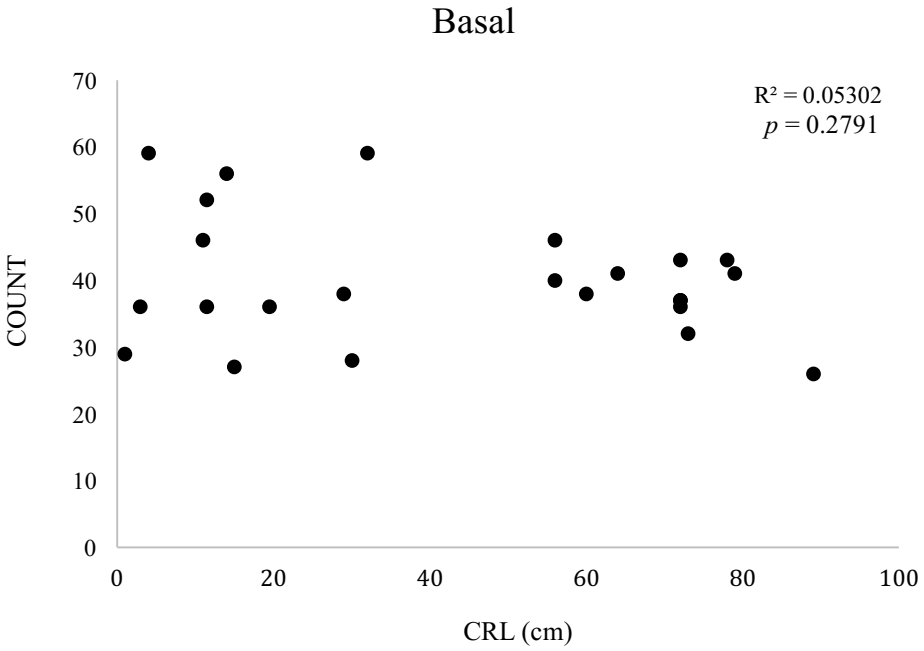

Figure 4.2: Number of basal chordal attachments to the anterior mitral valve leaflet in pregnant cows (n=24 valves) plotted against fetal crown-to-rump length (CRL) in cm.

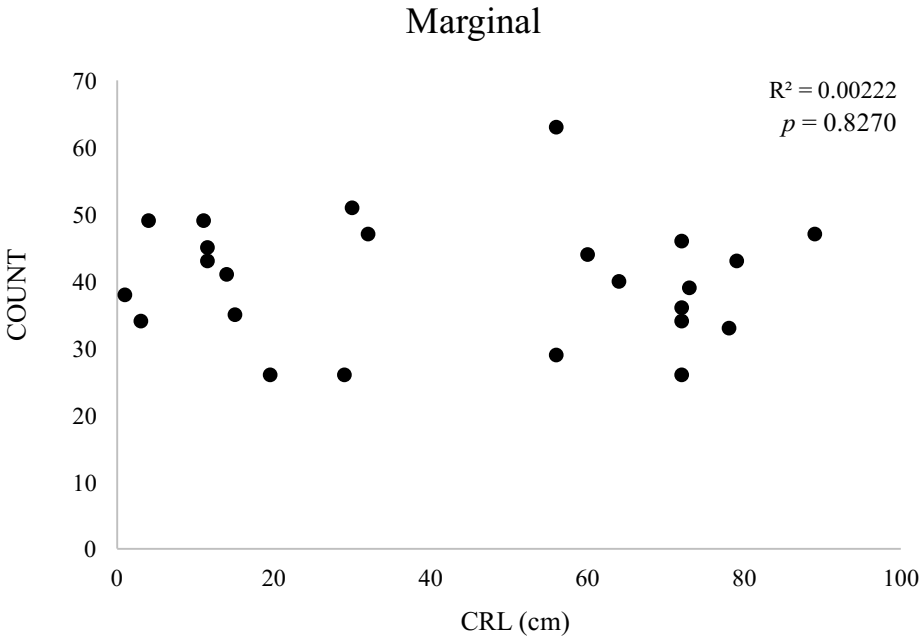

Figure 4.3: Number of marginal chordal attachments to the anterior mitral valve leaflet in pregnant cows (n=24 valves) plotted against fetal crown-to-rump length (CRL) in cm.

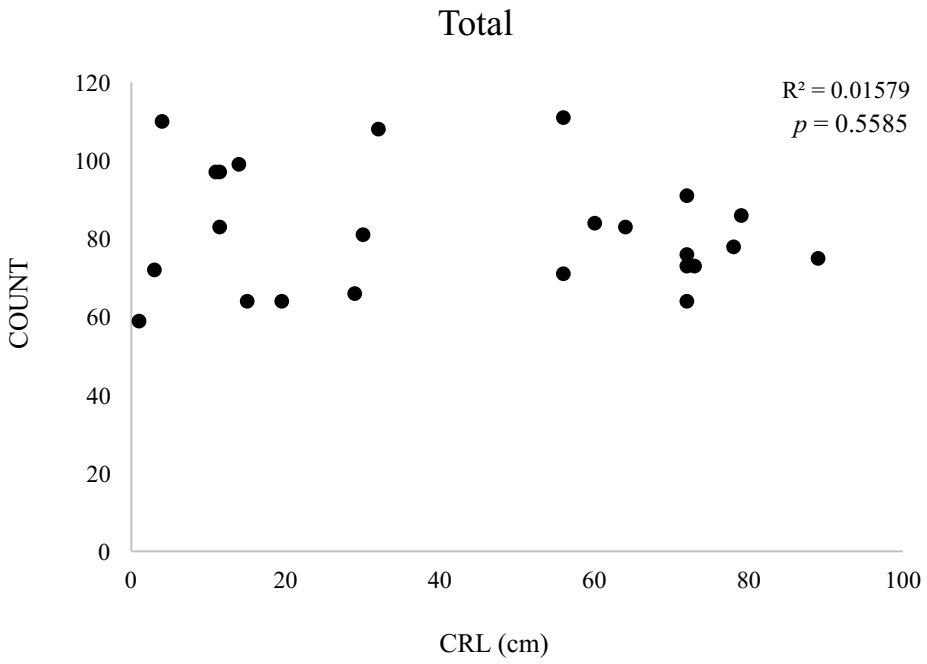

Figure 4.4: Total number of chordal attachments to the anterior mitral valve leaflet in pregnant cows (n=24 valves) plotted against fetal crown-to-rump length (CRL) in cm.

4.2 Collagen Thermal Properties Remain Largely Unchanged In Pregnancy, But Change Significantly With Chordae Type (DSC Results)

(i) *Effects of Pregnancy & Sampling Location*

Representative DSC endotherms for heifer and maternal chordae are provided in Figure 4.5. As evidenced by similar values of T_{onset} (68.4ºC vs 68.8ºC), T_{peak} (70.6ºC vs. 70.6ºC), and specific enthalpy (4.07 J/g vs. 4.67 J/g) between chordae taken from heifers and pregnant cows respectively, the thermal stability of bovine chordae did not change appreciably with pregnancy. However, the FWHM was significantly lower by approximately 0.3ºC in pregnancy, indicating a more homogeneous population of collagen molecules in maternal chordae (Figure 4.6). A 3-way repeated measures ANOVA revealed a significant interaction between pregnancy and sampling location for

T_{onset} (p=0.0049). Although T_{onset} did not differ significantly between heifers and pregnant cows at any sampling location, a post-hoc comparison of location within maternal chordae revealed a significantly higher T_{onset} for straight segments than for insertion sites (Figure 4.7). This finding suggests either (i) a molecular stabilization of a sub-population of maternal straight segment collagen, or (ii) a relative loss of thermal stability at insertion sites. Unlike T_{onset}, neither T_{peak}, specific enthalpy, nor the FWHM changed significantly with sampling location in pregnancy.

(ii) *Effects of Chordae Type*

Representative endotherms for each chordae type are provided in Figure 4.8. Unrelated to pregnancy state, thermal stability changed significantly with chordae type. Strut chordae were the least thermally stable with values of T_{onset} and T_{peak} of 67.6ºC and 69.6ºC respectively, while marginal chordae were the most thermally stable, with values of T_{onset} and T_{peak} over 2ºC higher (Figure 4.9, Figure 4.10). This trend was reversed with enthalpy, where the strut chordae showed the highest enthalpy at 5.88 J/g and the marginal chordae showed the lowest at 2.56 J/g (Figure 4.11). In each case, basal chordae had intermediate values of T_{onset}, T_{peak}, and specific enthalpy between that of the marginal and strut chordae (Figure 4.9-Figure 4.11). The FWHM was unchanged between strut and basal chordae (2.42ºC vs. 2.45ºC), but both were significantly lower than the FWHM for marginal chordae (2.83ºC) as seen in Figure 4.12. The higher T_{onset} and T_{peak} observed in marginal chordae suggests a more tightly packed collagen network relative to the strut and basal chords, while the broader FWHM indicates a more heterogeneous collagen population. The lower enthalpy of denaturation for marginal chordae (despite an increased thermal stability) could speak to their hydration state – being less hydrated than other chordae types.

(iii) *Effects of Sampling Distance*

When the DSC thermal parameters were plotted against sample distance from the leaflet surface, no significant trends were found in chordae taken from pregnant cows. Unexpectedly in heifers however, T_{onset} and T_{peak} decreased with increasing sample distance from the leaflet, while enthalpy significantly increased (Figure 4.13-Figure

4.15). This suggests a tighter molecular packing of collagen molecules near the leaflet surface in heifers, possibly due to a spatially heterogeneous cross-link profile along the chordal length.

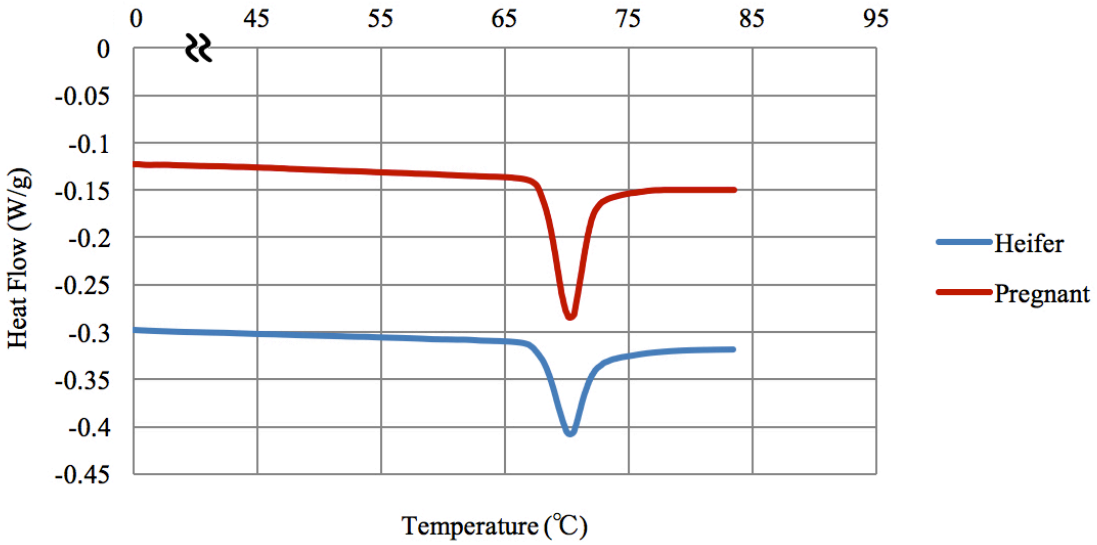

Figure 4.5: Representative differential scanning calorimetry endotherms for bovine mitral chordae taken from heifers and pregnant cows. A narrowing of the endotherm trace (lower FWHM) is evident; curves were similar with respect to all other thermal parameters (T_{onset}, T_{peak}, and specific enthalpy). Baselines have been Y-scale adjusted to separate individual endotherms.

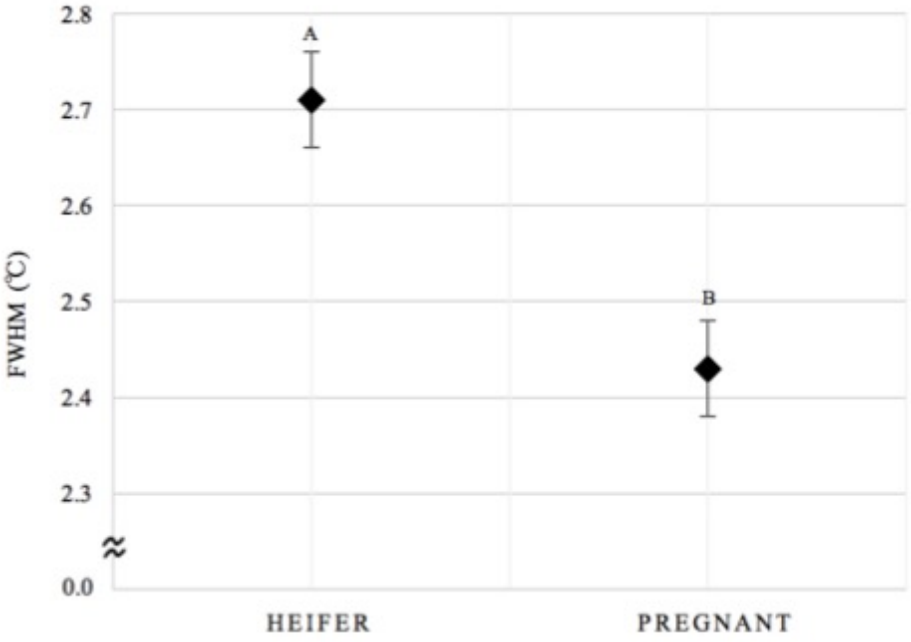

Figure 4.6: Differential scanning calorimetry endotherm full width at half maximum (FWHM) for anterior mitral valve chordae taken from non-pregnant heifers (50 samples from 7 valves) and pregnant cows (49 samples from 6 valves). Values are expressed as mean ± SE. Dissimilar letters indicate statistical significance (p<0.005).

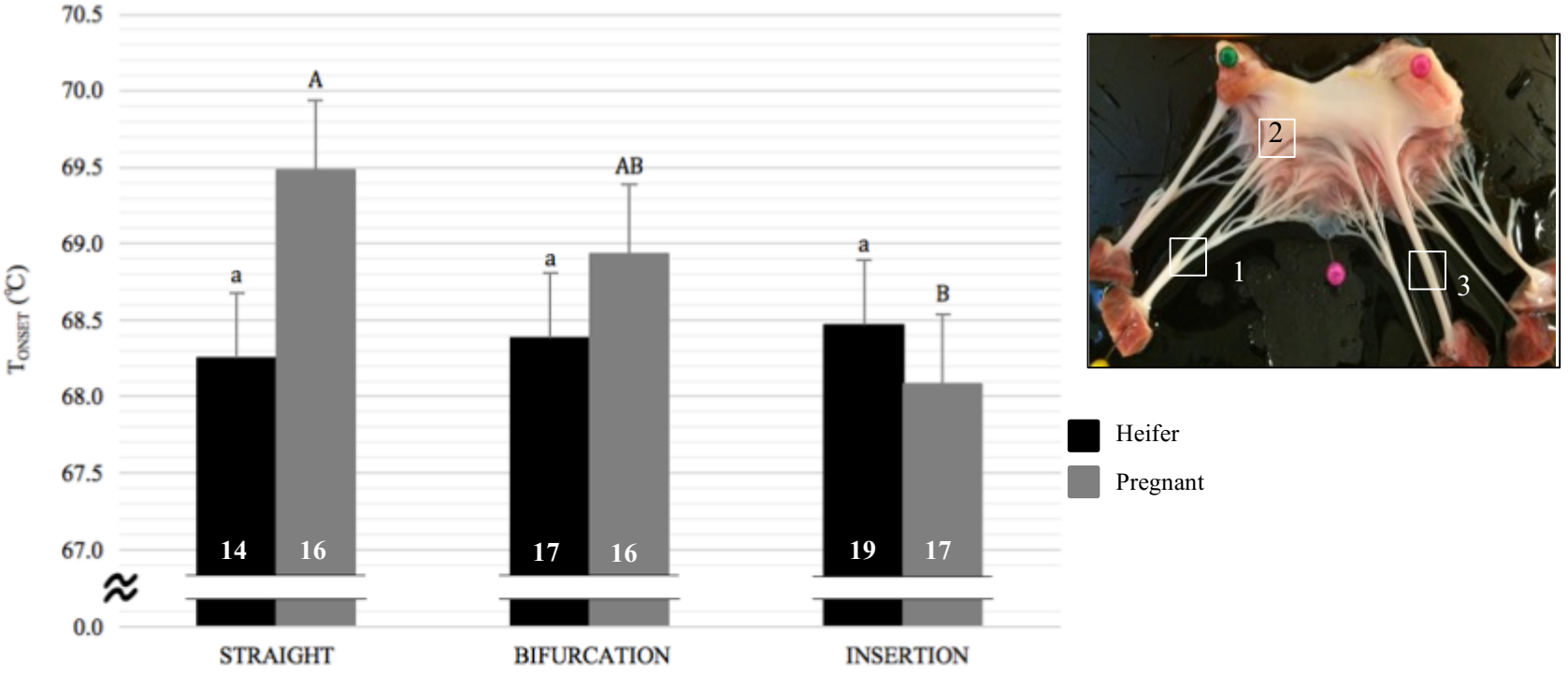

Figure 4.7: Differential scanning calorimetry endotherm onset temperature (T_{onset}) for anterior mitral valve chordae in non-pregnant heifers and pregnant cows. Samples were grouped and compared based on their location as either: (i) A "bifurcation" (region where 2 or more chordae branch); (ii) an "insertion" (where the chorda merges with the leaflet tissue), or (iii) a "straight" segment (i.e. not a bifurcation or insertion). Rightmost portion of the figure provides examples of bifurcation (1), insertion (2), and straight (3) chordae samples. A 3-way repeated measures ANOVA revealed a significant interaction between pregnancy and sample location (p=0.0049). Values are expressed as mean ± SE. Dissimilar letters with the same case indicate a significant post-hoc difference (p<0.005). Bars show specific n-values (used in post-hoc statistical testing) taken from a total of 7 heifer and 6 maternal valves (with chordae types pooled together as there was no effect of pregnancy for any chordae type).

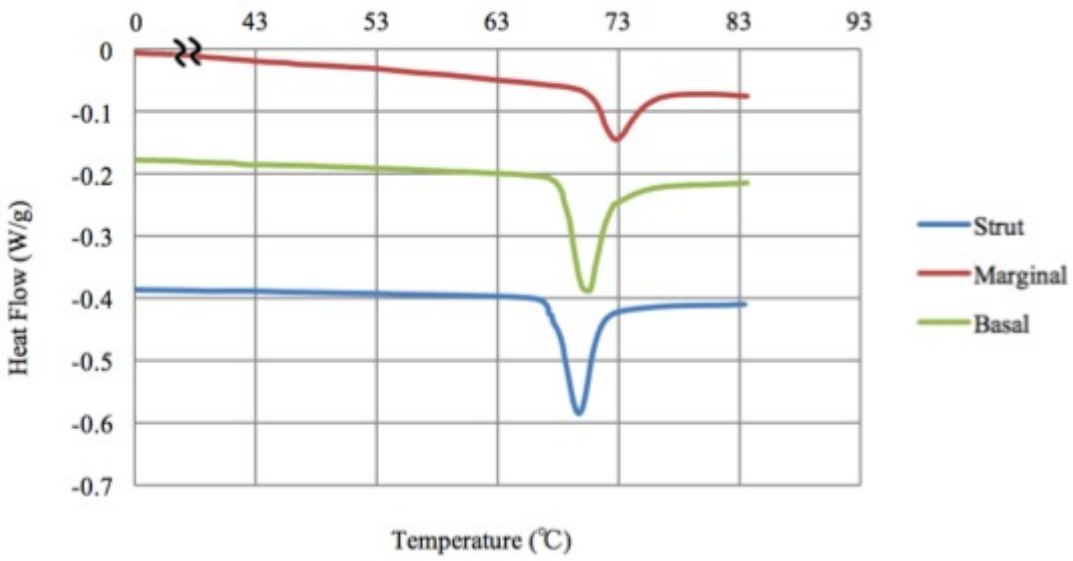

Figure 4.8: Representative differential scanning calorimetry endotherms for bovine mitral chordae tendineae. An overall rightward shift (increase in thermal stability) is visible in the endotherms from strut, to basal, to marginal chordae. Baselines have been Y-scale adjusted to separate individual curves.

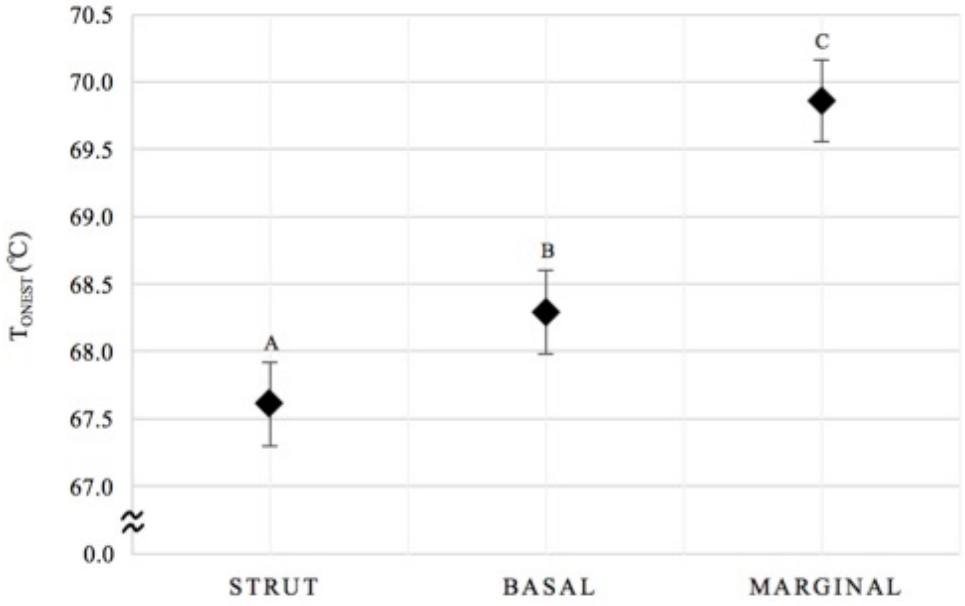

Figure 4.9: Differential scanning calorimetry endotherm onset temperature (T_{onset}) for anterior bovine mitral valve strut, basal, and marginal chordae. A total of 34 strut, 31 basal, and 34 marginal samples pooled from 7 heifer and 6 maternal valves were used in the analysis. Values are expressed as mean ± SE. Dissimilar letters indicate statistical significance between chordae types (p<0.001).

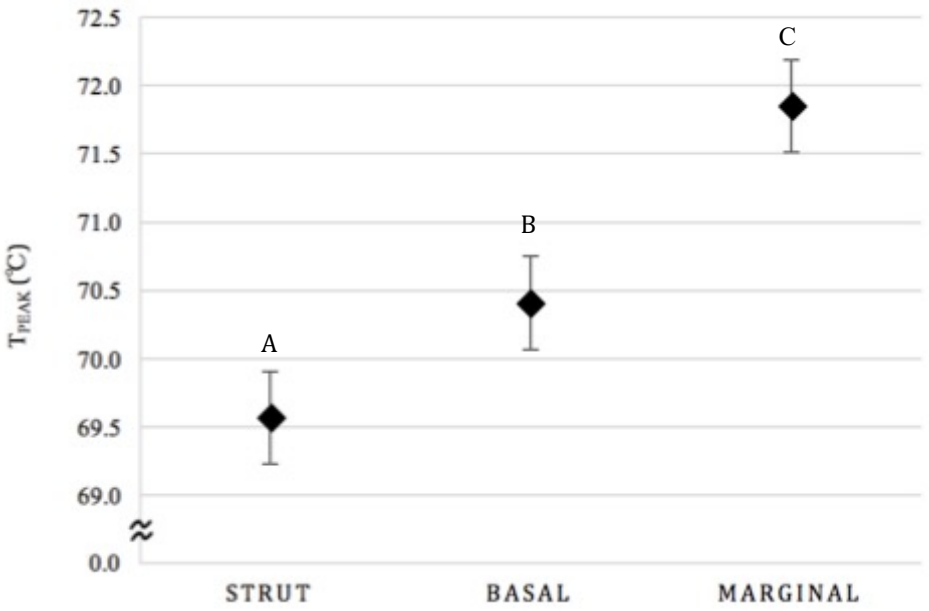

Figure 4.10: Differential scanning calorimetry endotherm peak temperature (T_{peak}) for anterior bovine mitral valve strut, basal, and marginal chordae. A total of 35 strut, 33 basal, and 33 marginal samples pooled from 7 heifer and 6 maternal valves were used in the analysis. Values are expressed as mean ± SE. Dissimilar letters indicate statistical significance between chordae types (p<0.001).

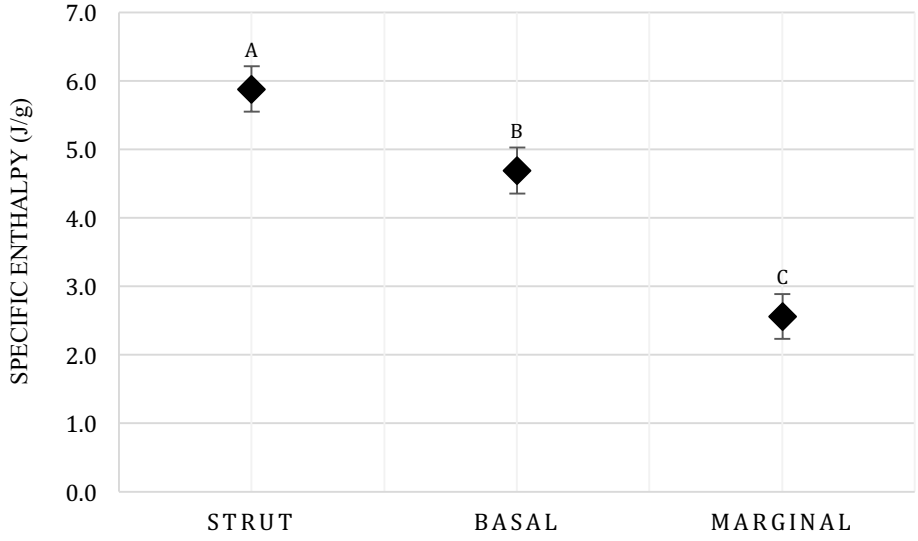

Figure 4.11: Differential scanning calorimetry endotherm specific enthalpy (based on sample wet weight) for bovine anterior mitral valve strut, basal, and marginal chordae. A total of 34 strut, 31 basal, and 34 marginal samples pooled from 7 heifer and 6 maternal valves were used in the analysis. Values are expressed as mean ± SE. Dissimilar letters indicate statistical significance between chordae types (p<0.001).

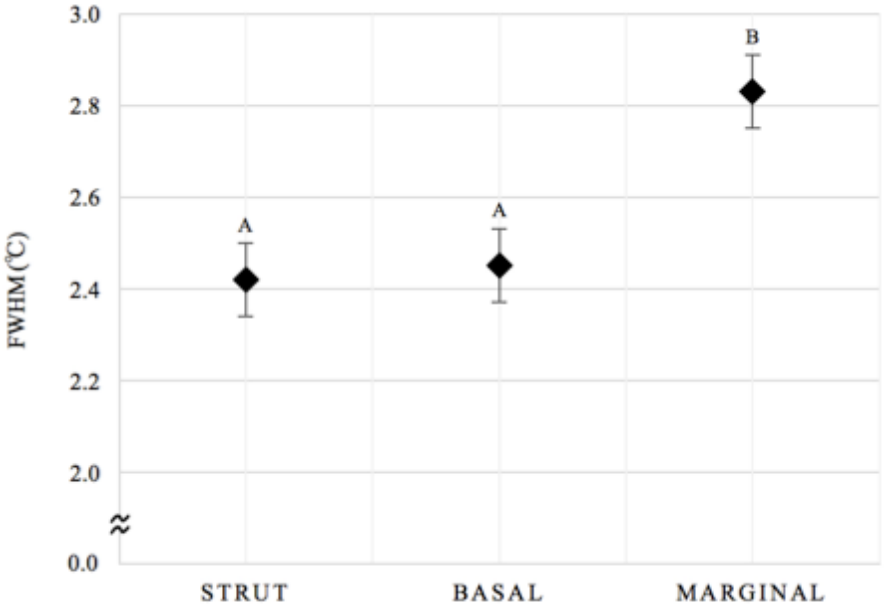

Figure 4.12: Differential scanning calorimetry endotherm full width at half maximum (FWHM) for anterior bovine mitral valve strut, basal, and marginal chordae. A total of 34 strut, 31 basal, and 34 marginal samples pooled from 7 heifer and 6 maternal valves were used in the analysis. Values are expressed as mean ± SE. Dissimilar letters indicate statistical significance between chordae types (p<0.05).

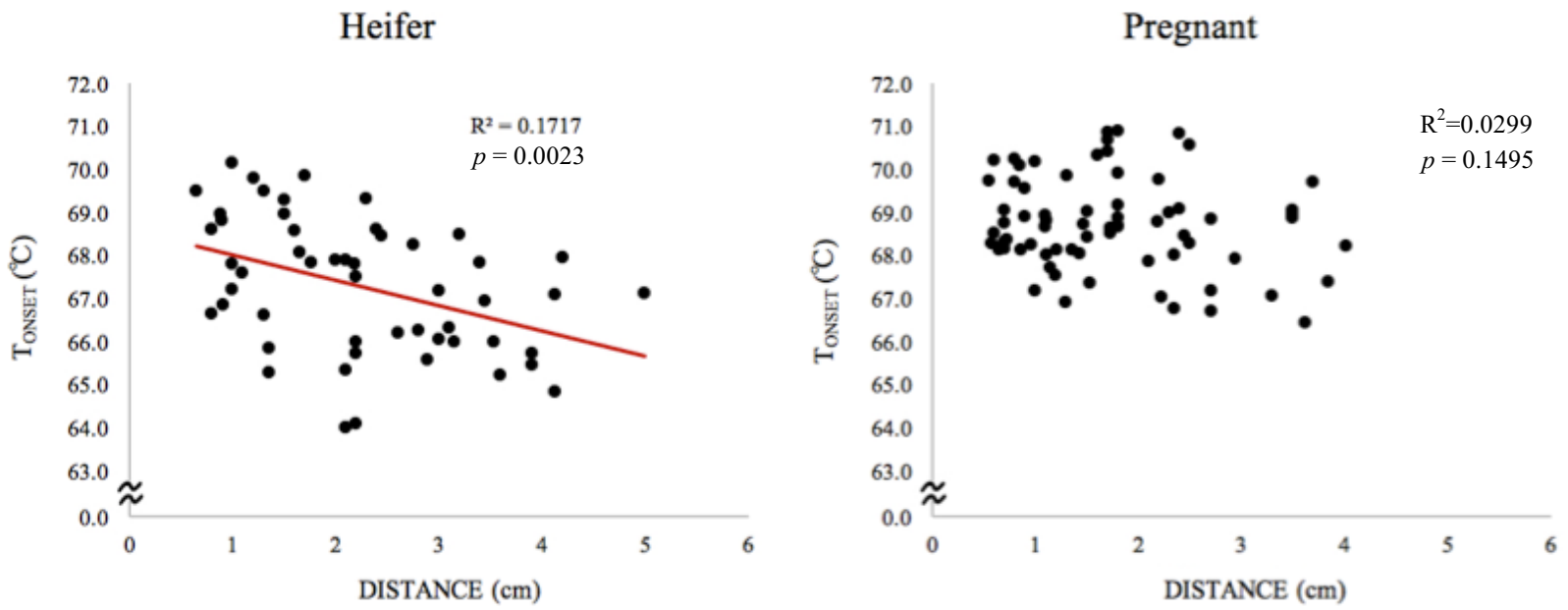

Figure 4.13: Differential scanning calorimetry endotherm onset temperature (T_{onset}) for anterior mitral valve chordae taken from non-pregnant heifers (52 samples taken from 6 valves) and pregnant cows (71 samples taken from 6 valves) plotted against each sample's distance from the leaflet surface.

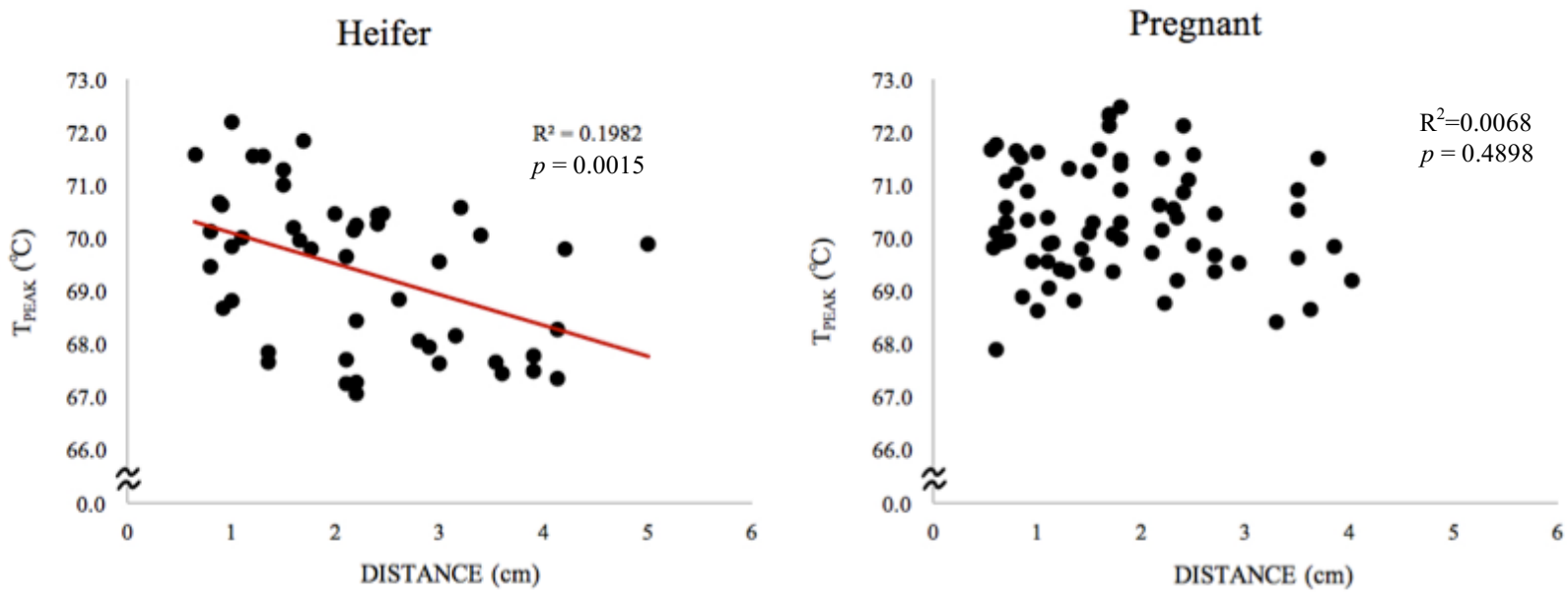

Figure 4.14: Differential scanning calorimetry endotherm peak temperature (T_{peak}) for anterior mitral valve chordae taken from non-pregnant heifers (48 samples taken from 7 valves) and pregnant cows (72 samples taken from 6 valves) plotted against each sample's distance from the leaflet surface.

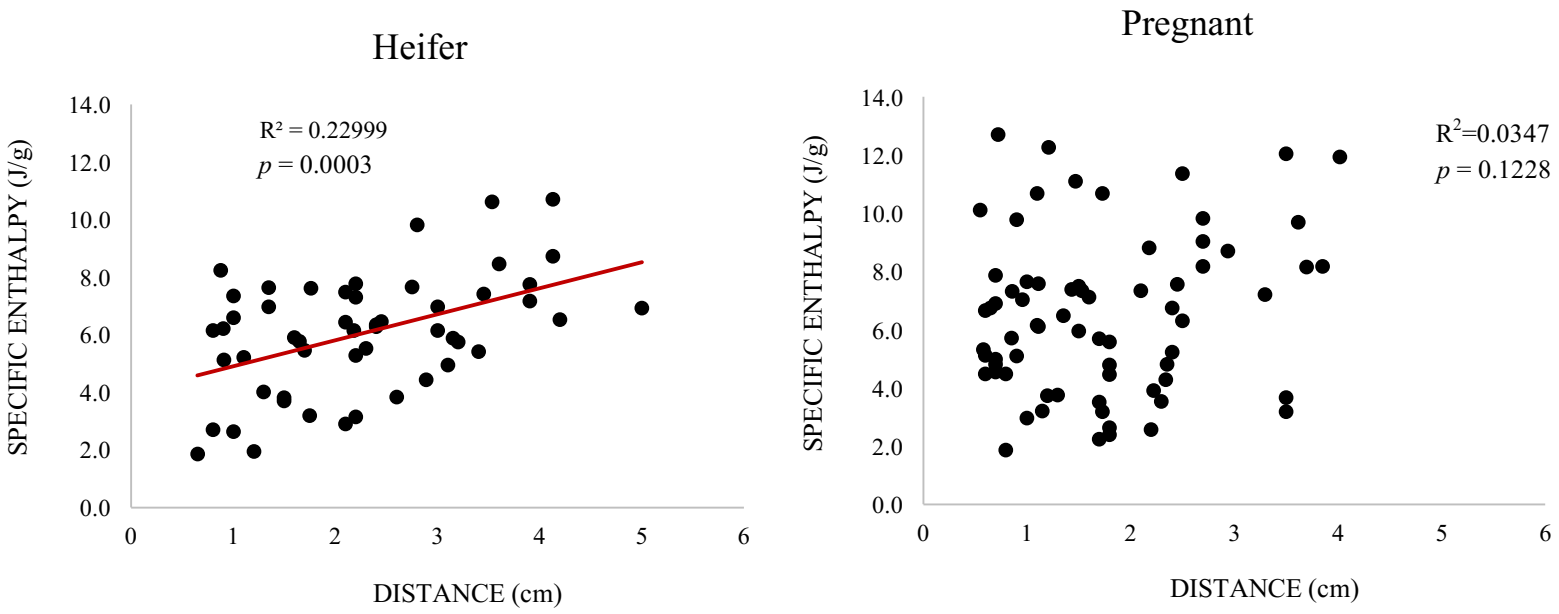

Figure 4.15: Differential scanning calorimetry endotherm specific enthalpy (based on sample wet weight) for anterior mitral valve chordae taken from non-pregnant heifers (52 samples taken from 7 valves) and pregnant cows (70 samples taken from 6 valves) plotted against each sample's distance from the leaflet surface.

4.3 Chordae Collagen Crimp Is Unchanged Between Heifers and Pregnant Cows

(i) *Effects of Pregnancy*

Collagen crimp wavelength and percent area occupied by crimp (measured at straight segments only) were unchanged between pregnant and non-pregnant animals; all straight segments were highly crimped (>98%) and the average crimp wavelengths were 20.1μm and 21.3μm for non-pregnant and pregnant animals respectively.

(ii) *Effects of Chordae Type & Sampling Distance*

Marginal chordae crimp wavelength was 16.2μm, approximately 32% shorter than that of both strut and basal chordae (Table 4.1, Figure 4.16). A surprising relationship between crimp wavelength and distance from the valve leaflet was discovered in strut and basal chordae (Figure 4.17, Figure 4.18), but was absent in marginal chords (Figure 4.19). For strut and basal chordae, crimp length increased with increasing distance from the leaflet, doubling in length from approximately 15μm near the leaflet surface to over 30μm approaching the papillary muscles.

(iii) *Effects of Sampling Location*

Collagen crimp was frequently disrupted at bifurcations and leaflet insertion sites in both heifers and pregnant cows. Picrosirius Red stained sections viewed under polarized light showed a complete loss of crimp at select bifurcations as evidenced by a loss of birefringence. The orientation of some collagen fibers was also skewed relative to the longitudinal axis, curling into or away from the bifurcation (Figure 4.20). Crimp disruption at bifurcations was, at times, only localized to the bifurcation tip, while in others crimp disruption propagated deep (>6mm) into the tissue bulk. Crimp progression into the leaflet tissue was characterized by a 'smearing', or an apparent flattening of crimp in some fibers; crimp directionality was no longer simply longitudinal, but rather frequently fanned out as the chordae merged with the leaflet (Figure 4.21).

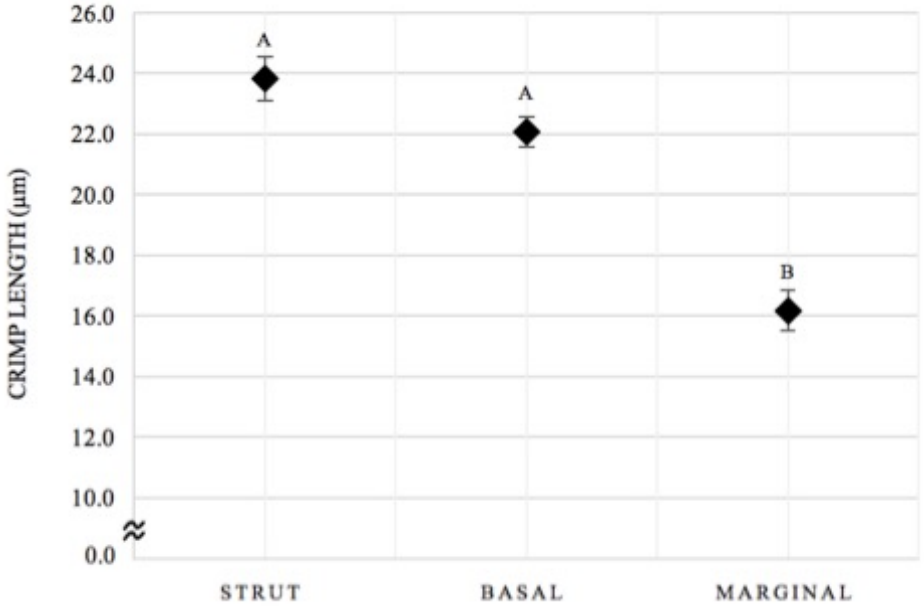

Figure 4.16: Collagen crimp length in bovine anterior mitral valve strut, basal, and marginal chordae. A total of 37 strut, 82 basal, and 46 marginal samples pooled from 4 heifer and 4 maternal valves were used in the analysis. Values are expressed as mean ± SE. Dissimilar letters indicate statistical significance between chordae types (Strut vs. marginal $p<0.001$; basal vs. marginal $p<0.005$).

Table 4.1: Summary of collagen crimp length and percent area occupied by crimp in anterior mitral valve strut, basal, and marginal chordae from non-pregnant heifers and pregnant cows. A total of 15 strut, 30 basal, and 20 marginal samples from 4 heifer valves, and 22 strut, 52 basal, and 26 marginal samples from 4 maternal valves were used in the analysis. Values are expressed as mean ± SE. There were no significant differences in any crimp measurement between heifers and pregnant animals. Crimp length was significantly shorter in marginal chordae in comparison to that in strut and basal ($p<0.005$).

	Strut		**Basal**		**Marginal**	
	Length (μm)	*Area (%)*	*Length (μm)*	*Area (%)*	*Length (μm)*	*Area (%)*
Heifer	23.4 ± 0.9	98.9 ± 0.9	21.4 ± 0.6	98.1 ± 0.6	15.8 ± 0.8	97.4 ± 0.9
Pregnant	24.1 ± 1.1	99.3 ± 0.6	22.5 ± 0.7	98.1 ± 0.4	16.5 ± 1.0	97.4 ± 0.6

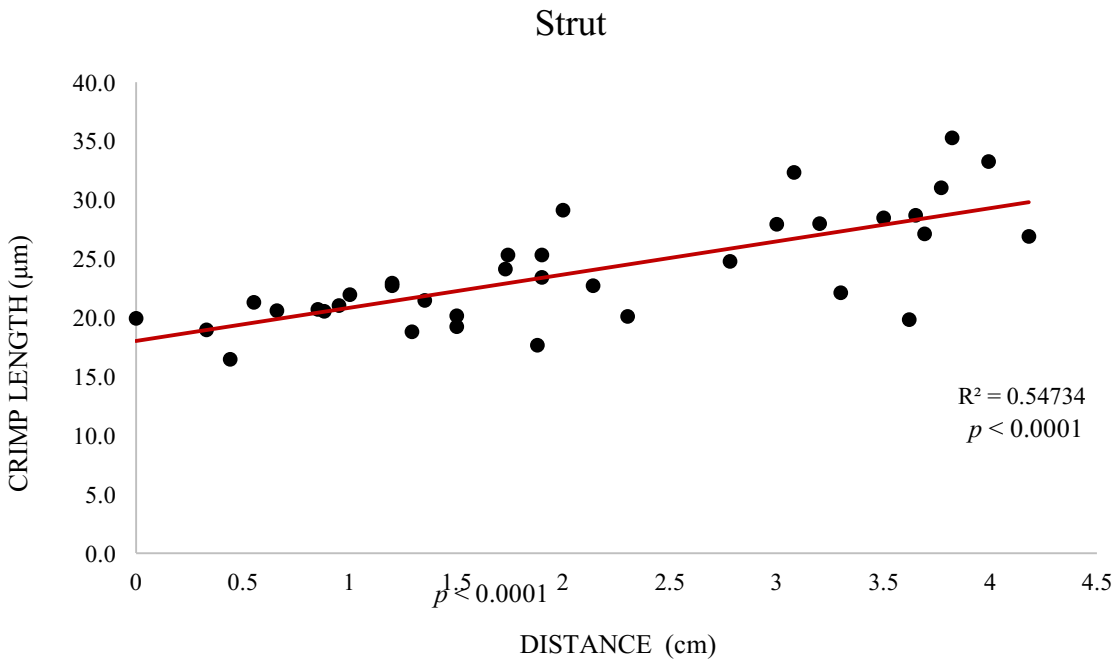

Figure 4.17: Collagen crimp length in bovine anterior mitral valve strut chordae plotted against distance from the valve leaflet. A total of 36 strut straight segments were pooled from 4 heifer and 4 maternal valves.

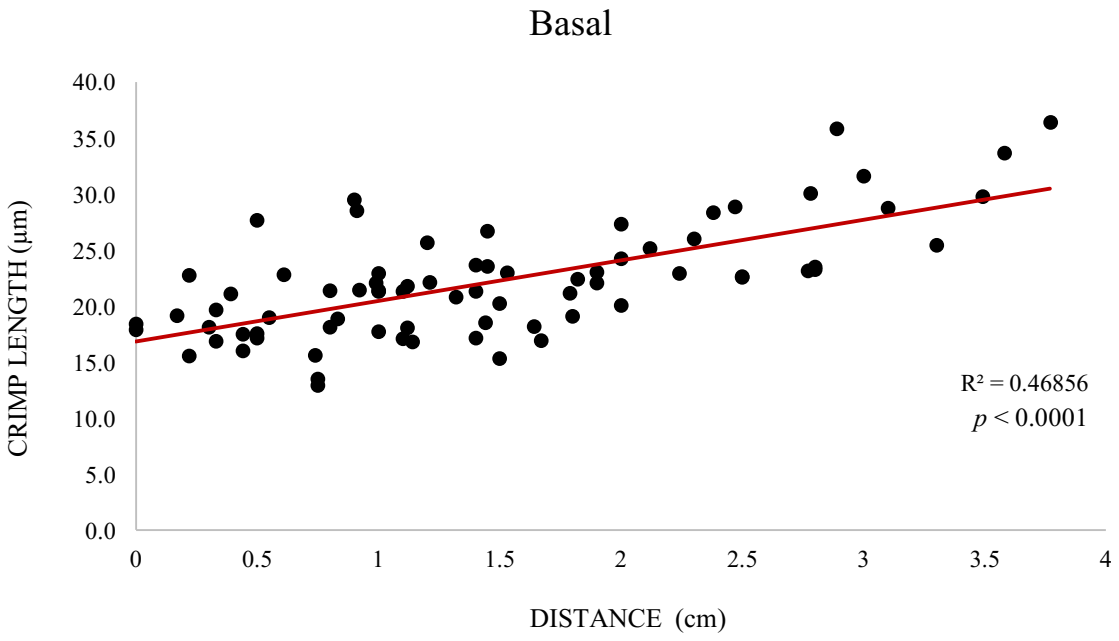

Figure 4.18: Collagen crimp length in bovine anterior mitral valve basal chordae plotted against distance from the valve leaflet. A total of 75 basal straight segments were pooled from 4 heifer and 4 maternal valves.

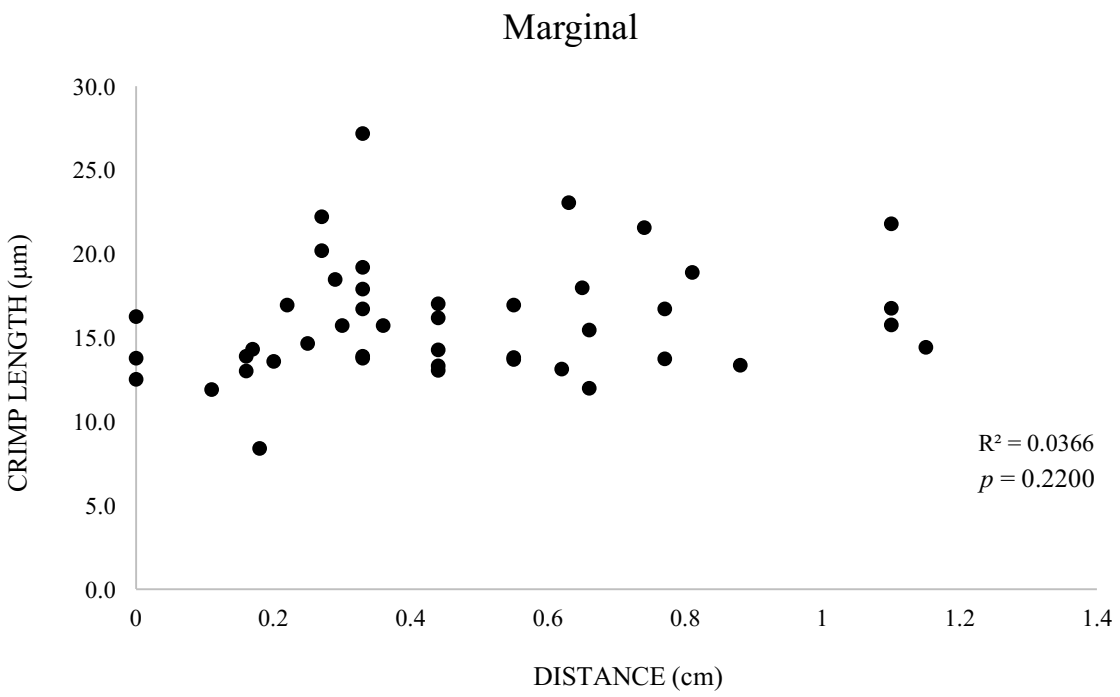

Figure 4.19: Collagen crimp length in bovine anterior mitral valve marginal chordae plotted against distance from the valve leaflet. A total of 44 marginal straight segments were pooled from 4 heifer and 4 maternal valves.

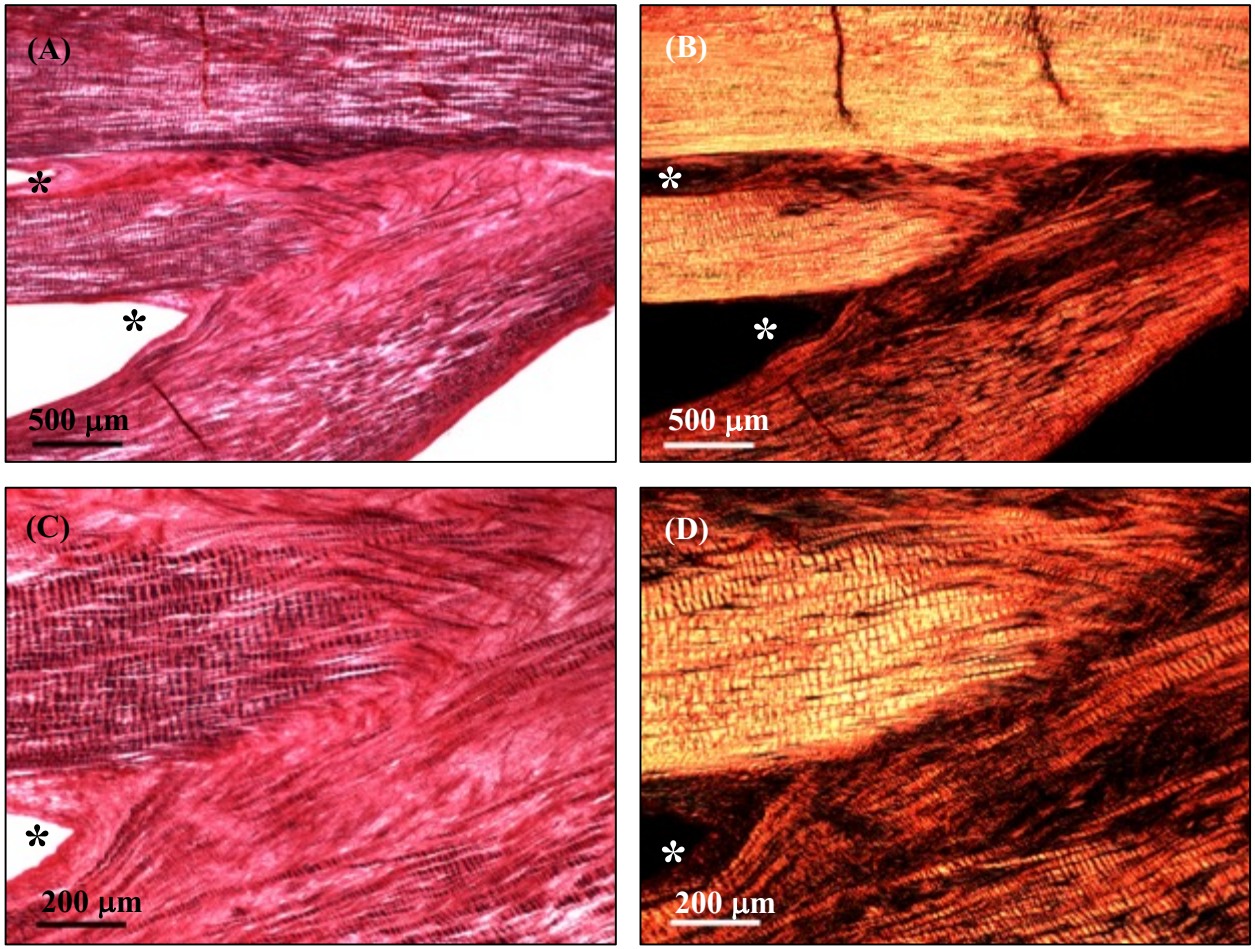

Figure 4.20: Picrosirius Red-stained longitudinal section taken through a chorda bifurcation viewed with brightfield illumination (A, C) and their identical images viewed with polarized light (B, D). Collagen crimp is disrupted at chordae bifurcations as evidenced by a visible loss of fiber banding (indicative of collagen crimp) and a loss of birefringence when viewed under polarized light (black regions within the tissue). C and D are higher magnification views of A and B respectively. Bifurcation tips are marked with an asterix (*).

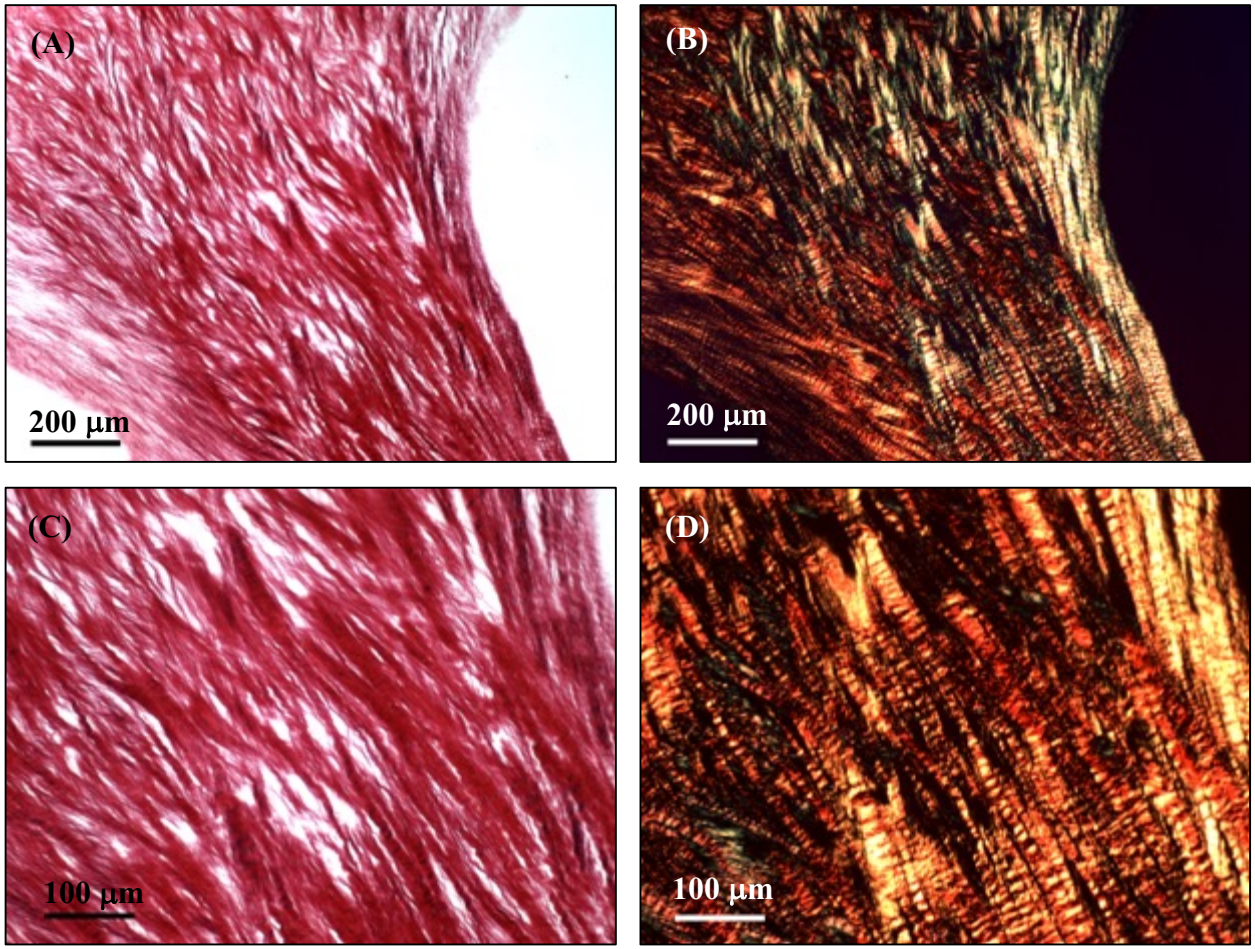

Figure 4.21: Picrosirius Red-stained longitudinal section taken through the leaflet-chordal interface viewed with brightfield illumination (A, C) and their identical images viewed with polarized light (B, D). Collagen fibers fan out as they progress into the leaflet tissue and there is a visible 'smearing' of collagen crimp. C and D are higher magnification views of A and B respectively.

4.4 Movat Pentachrome Reveals Unique Bifurcation Composition With High Cell Density And Elastin Propagations

In both pregnant and non-pregnant animals, straight chordae segments (i.e. not bifurcations or insertion sites) were composed primarily of collagen intermixed with GAGs (Figure 4.22). A dense staining of elastin was present at the periphery, with relatively sparse elastic fibers towards the tissue center. Elastin fibers were typically thicker near the tissue edge, and finer within the tissue bulk. VICs were scattered evenly throughout the tissue and appeared wedged between collagen fibers as their shape was rather elongated, reflecting the waves of collagen crimp. A monolayer of endothelial cells was also visible lining the outside chordal wall. Tissue at leaflet insertion sites had a similar composition, although GAGs appeared more abundant.

All observations noted at chordae bifurcations were seen in both pregnant and non-pregnant animals. Bifurcations contained the highest density of GAGs and cell nuclei (Figure 4.23). Certain GAG-rich bifurcations were visibly delaminated from the surrounding bifurcation tissue. In contrast to the cells in the surrounding tissue, cells located at bifurcations frequently took on a circular morphology. Elastic fibers, which were principally located only in the peripheral chordal layer, were relatively small and fragmented at select bifurcations, while completely absent from others (Figure 4.24 ‘A’). Some bifurcations were unique in that they showed a longitudinal propagation of elastin into the bifurcation tip. At times the elastin only extended a short distance into the bifurcation tip (Figure 4.24 ‘B’), while in others, elastin from both sides of the bifurcation propagated deep into the tissue bulk and joined together (Figure 4.24 ‘C’). A semi-quantitative analysis classifying these different bifurcation elastin morphologies revealed no differences in the frequency of any morphology between non-pregnant and pregnant animals (Table 4.2). When viewed under polarized light, bifurcations varied considerably in their birefringence, indicating different levels of collagen organization or the absence of collagen altogether (Figure 4.25).

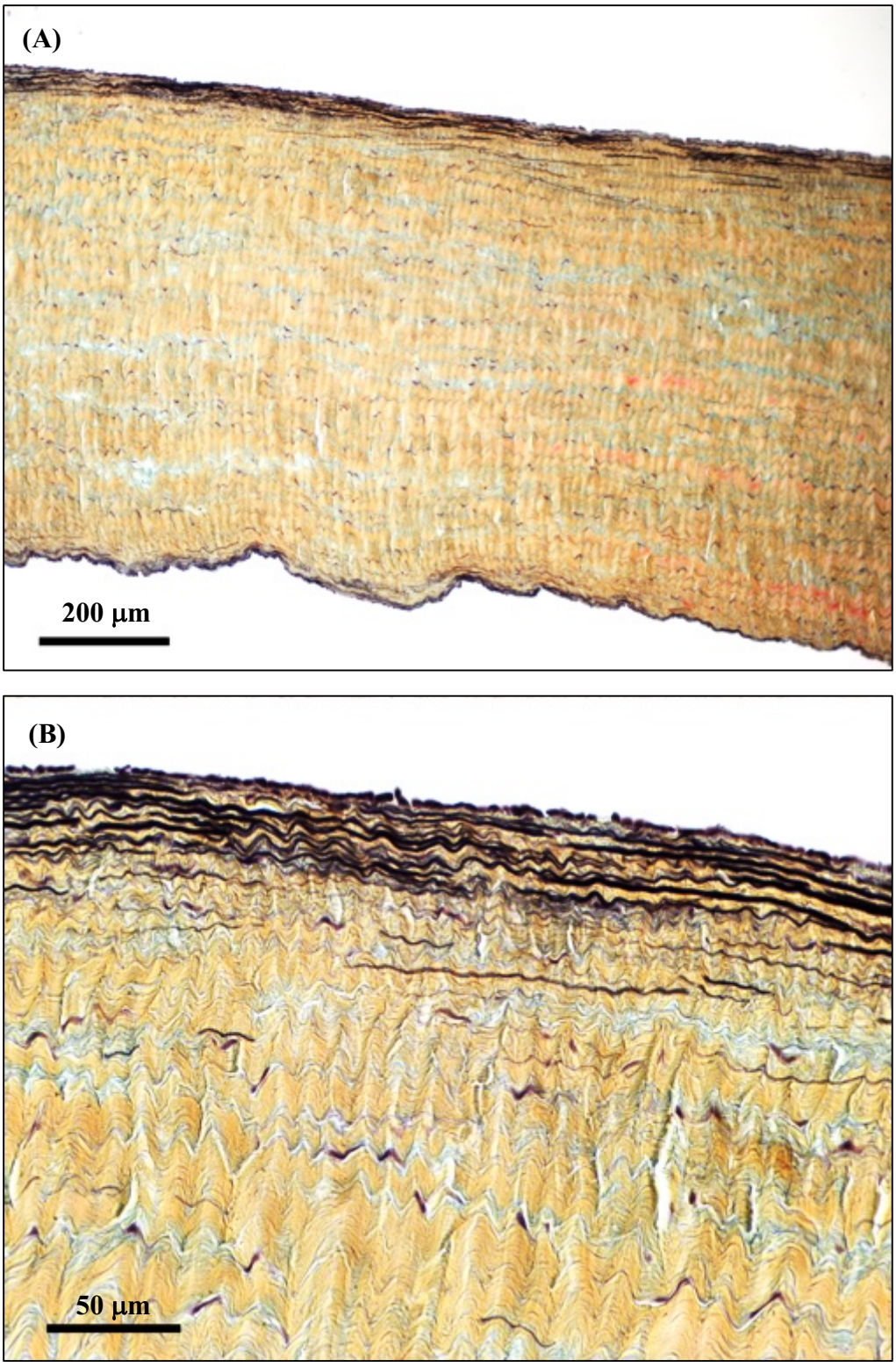

Figure 4.22: Movat Pentachrome-stained longitudinal section of a typical chorda straight segment. (A) Low magnification overview; (B) High magnification image emphasizing the dense layer of elastin observed at the periphery. Yellow=collagen, blue/green=GAGs, black lines=elastin fibers, purple elongations/circles=cell nuclei.

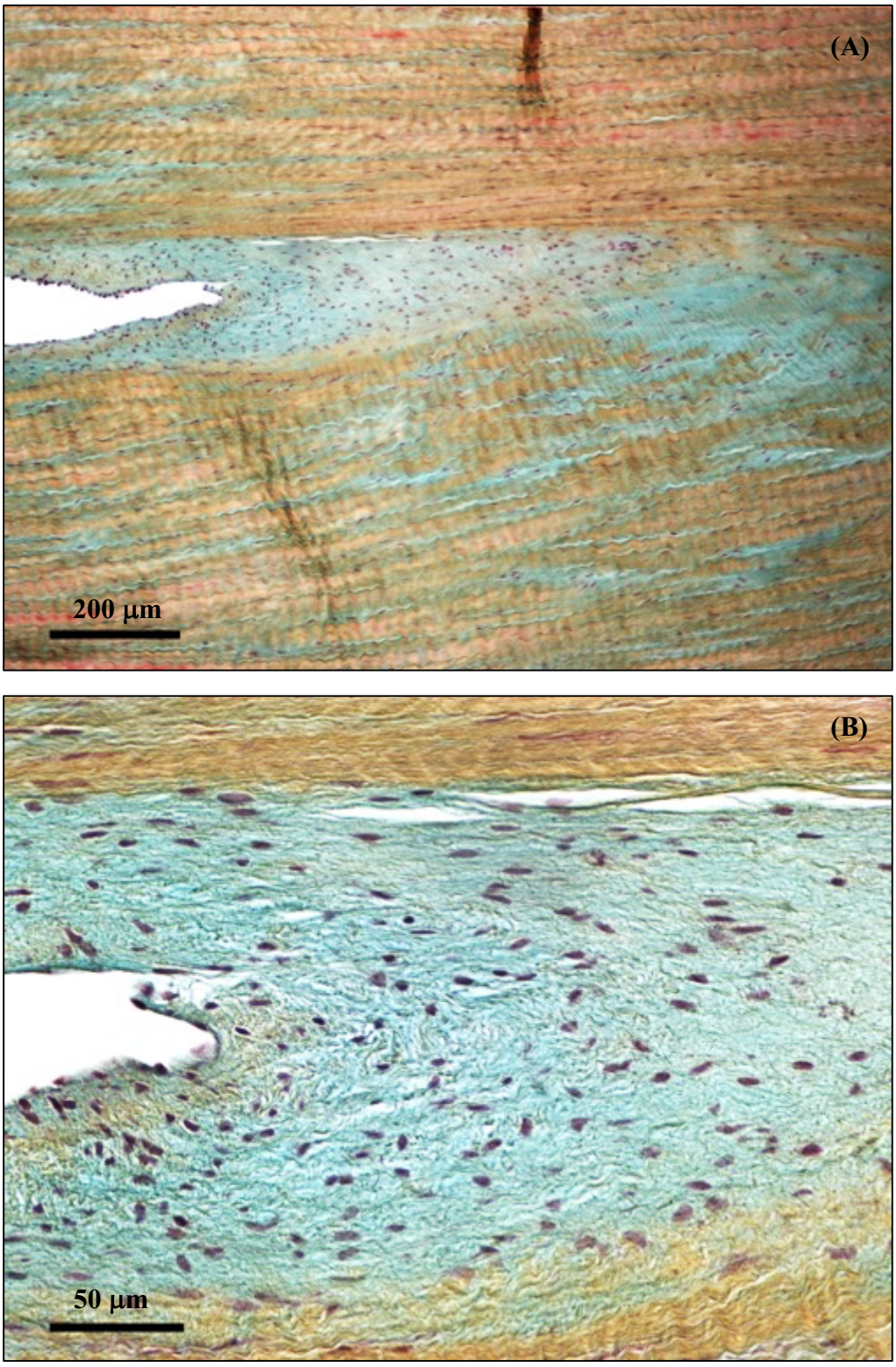

Figure 4.23: Movat Pentachrome-stained longitudinal section through a chorda bifurcation showing its unique composition relative to straight tissue segments. (A) Low magnification overview of a bifurcation in comparison to surrounding tissue; (B) High magnification image showing the dense cellularity and GAG presence typically seen at bifurcations. Yellow=collagen, blue/green=GAGs, purple elongations/circles=cell nuclei.

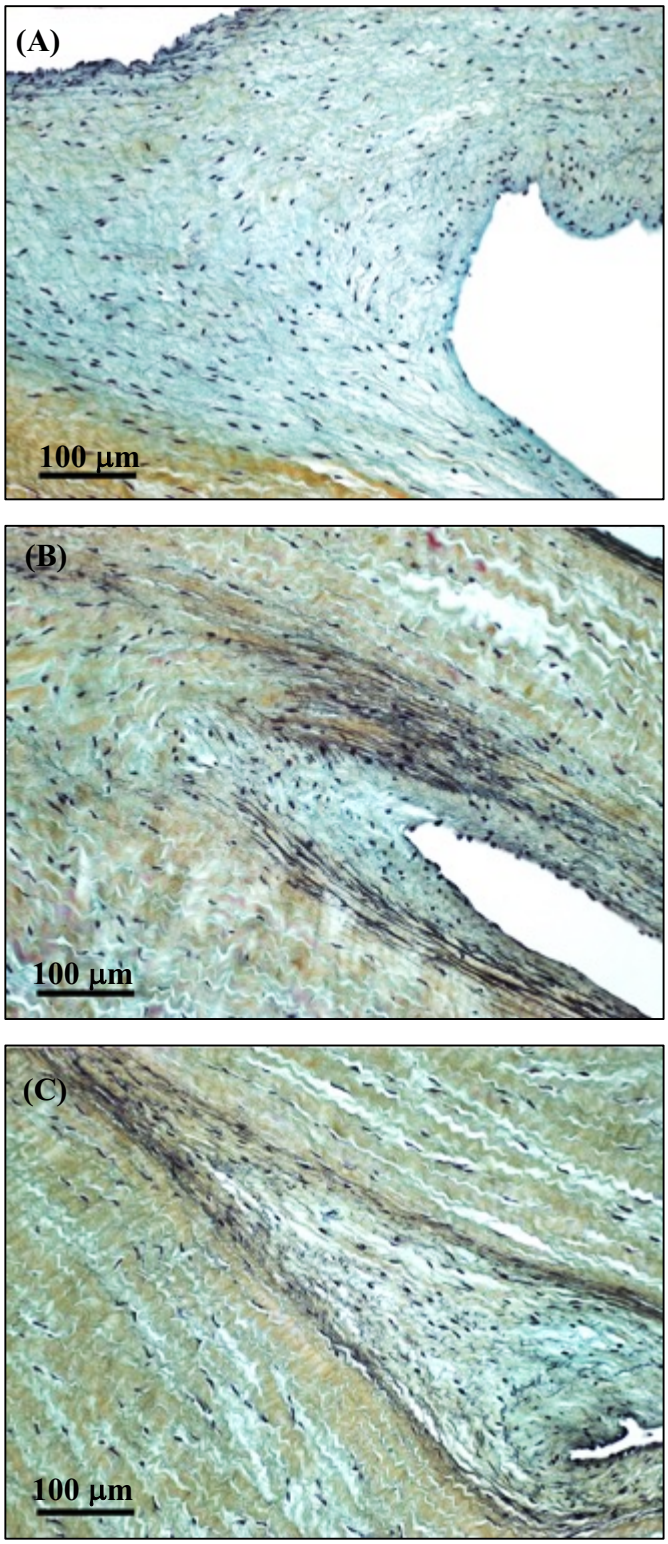

Figure 4.24: Movat Pentachrome-stained longitudinal sections through chordae bifurcations showing a progressive presence of peripheral elastin into the bifurcation. (A) No elastin present, (B) elastin present and extending into the bifurcation, and (C) elastin present propagating deep into the bifurcation joined from both sides. Yellow=collagen, blue/green=GAGs, black lines=elastin fibers, purple elongations/circles=cell nuclei.

Table 4.2: The presence of elastin at chordae bifurcations was semi-quantitatively grouped according to one of four morphologies: (0) No elastin present (Figure 4.24 'A'); (1) only small, fragmented elastic fibers present with no defined directionality; (2) elastin on one or both sides of the bifurcation had begun extending longitudinally into the bifurcation tip (Figure 4.24 'B'); and (4) elastin propagation from both sides of the bifurcation had joined below the bifurcation (Figure 4.24 'C'). Chi-squared test revealed no significant differences between elastin morphologies in non-pregnant heifers (n=4 valves) and pregnant cows (n=4 valves) (p>0.9280).

Presence of Bifurcation Elastin					
Numerical Score	**0**	**1**	**2**	**3**	**Total**
Heifer	7	37	13	6	63
Pregnant	9	43	20	8	80
Total	16	80	33	14	143

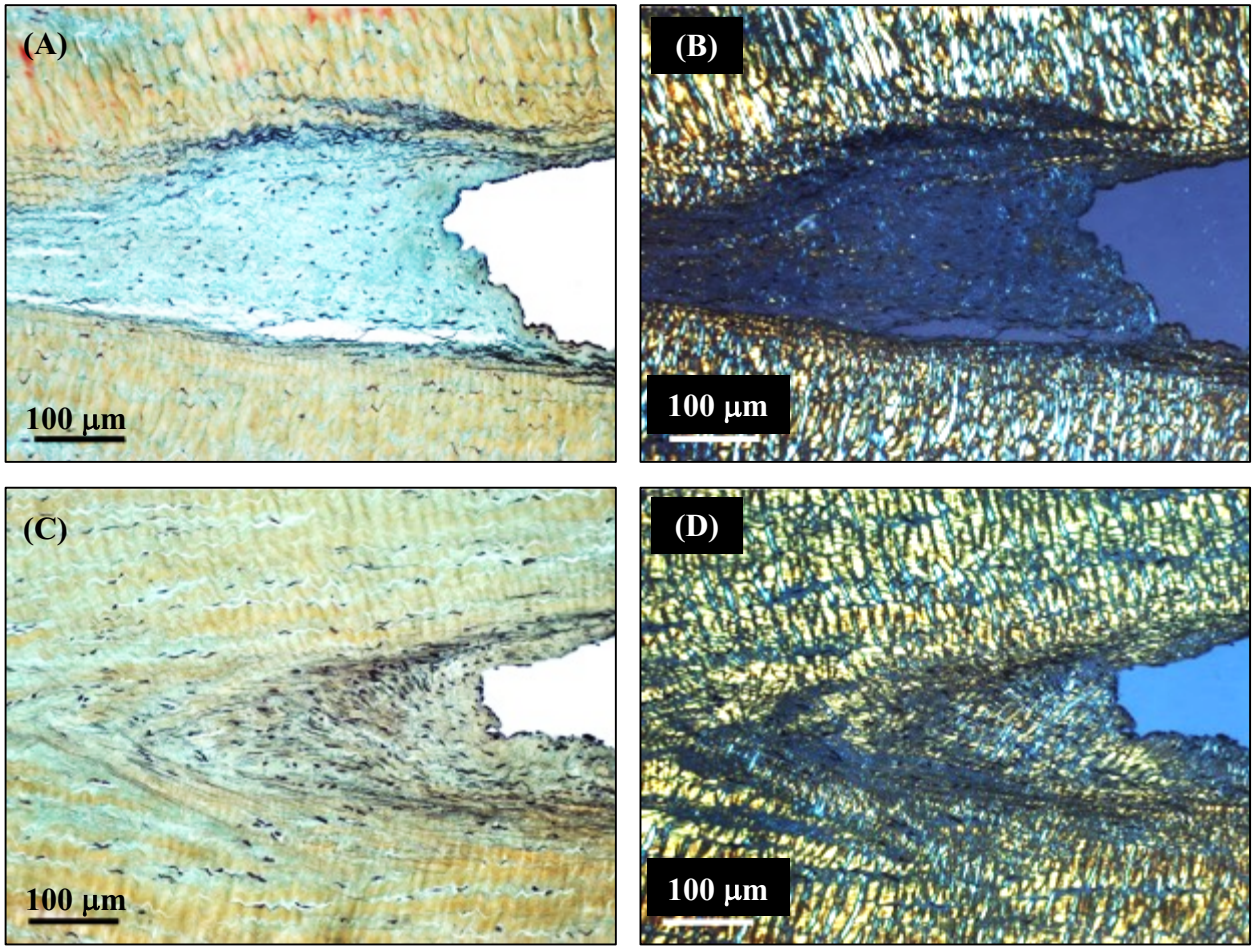

Figure 4.25: Movat Pentachrome-stained longitudinal sections through chordae bifurcations showing their diversity with respect to collagen content and organization. (A) GAG rich bifurcation viewed under brightfield illumination shows nearly a complete loss of birefringence under polarized light (B), while others display less GAG staining (C) and maintain the birefringence of the surrounding collagen crimp into the bifurcation (D). Yellow=collagen, blue/green=GAGs, black lines=elastin fibers, purple elongations/circles=cell nuclei.

4.5 Chordae Bifurcations are VIC Rich and Display Intense Periostin Expression

The density and distribution of VICs were unchanged between non-pregnant and pregnant animals (Table 4.3). As seen quantitatively in Figure 4.26 and histologically in Figure 4.27, VIC counting revealed a 4-fold increase in cell density at chordae bifurcations compared to straight segments (15.5 cells/0.01mm^2 vs. 3.7 cells/0.01mm^2).

Qualitatively, aVICs (α-SMA+) were found globally in the chordae tissue throughout straight segments, bifurcations, and leaflet tissue in both non-pregnant and pregnant animals. In some cases, clusters of aVICs surrounded tissue perforations located below bifurcations (in the common trunk segment). These areas also lacked collagen birefringence – strong evidence of ECM remodelling and/or collagen degradation in heifers and pregnant animals (Figure 4.28, Figure 4.29). Similarly, the number of α-SMA+ cells/0.01mm^2 and the % α-SMA+ cells were unchanged between pregnancy states (Table 4.3). The number of α-SMA+ cells/0.01mm^2 tended to be higher (p<0.095) at bifurcations relative to straight segments.

Periostin expression was abundant throughout chordae and leaflet tissue in both heifers and pregnant cows. At select bifurcations and around the outmost chordal layer, periostin expression was more intense – again, irrespective of pregnancy state. The intensity of periostin staining was strongly associated with the presence of elastin and was frequently observed overlapping with elastin propagations into the tissue bulk (Figure 4.30).

Table 4.3: Summary table of cell density and phenotype at straight segments and bifurcations for heifers (n=3 valves) and pregnant cows (n=3 valves). Values are shown as the mean ± SE. There were no significant differences in any cell density/phenotype measurement between heifers and pregnant animals. Total cell density was significantly higher at bifurcations in comparison to straight segments (p<0.0001).

	Straight		Bifurcation	
	Heifer	*Pregnant*	*Heifer*	*Pregnant*
Total Cell Density (per 0.01mm^2)	3.9 ± 0.7	3.4 ± 0.5	14.4 ± 0.8	16.5 ± 1.7
α-SMA + Cells (per 0.01mm^2)	0.2 ± 0.1	0.4 ± 0.3	1.0 ± 0.6	2.7 ± 1.7
% α-SMA + Cells	4.3 ± 1.7	7.1 ± 4.3	7.1 ± 4.1	14.4 ± 8.3

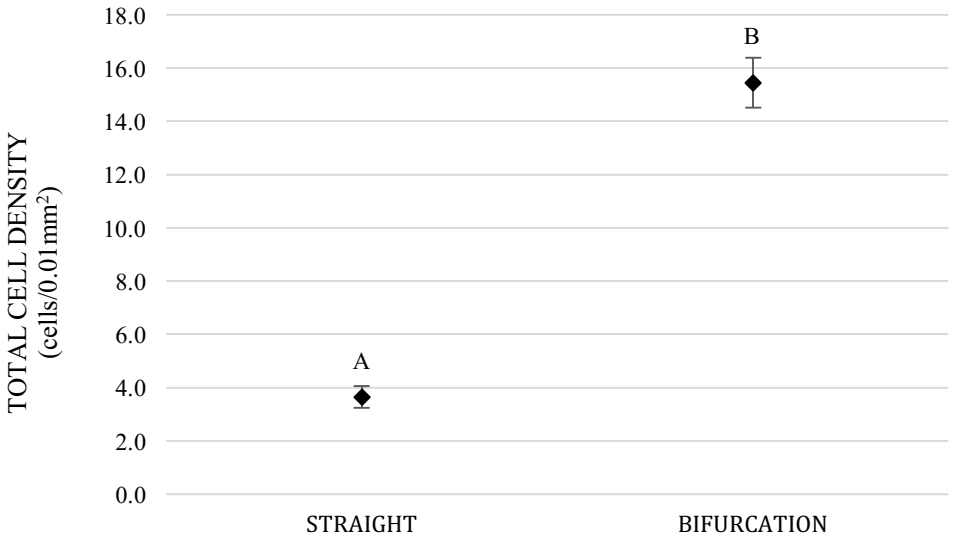

Figure 4.26: Total cell density (expressed per 0.01mm^2) at straight segments and chordae bifurcations counted from images of α-SMA immunostained longitudinal sections of bovine mitral chordae. A total of 95 bifurcations and 92 straight segments pooled from 3 heifer and 3 maternal valves were used in the analysis. Dissimilar letters indicate statistical significance (p<0.0001). Values are shown as the mean ± SE.

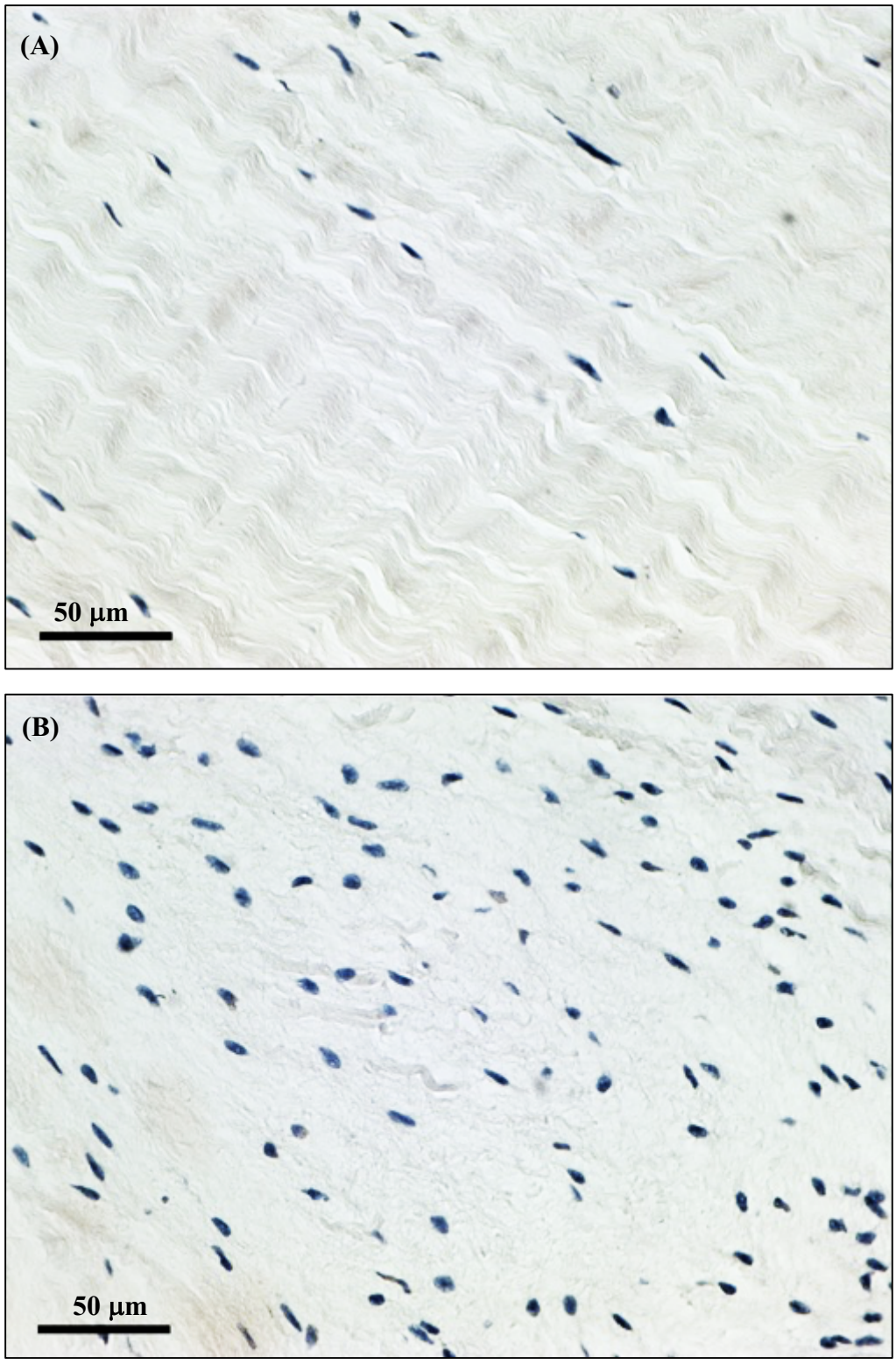

Figure 4.27: α-SMA immunostained longitudinal sections of bovine mitral chordae showing (A) a typical straight segment and (B) a typical bifurcation with respect to the number of VIC nuclei present in each location.

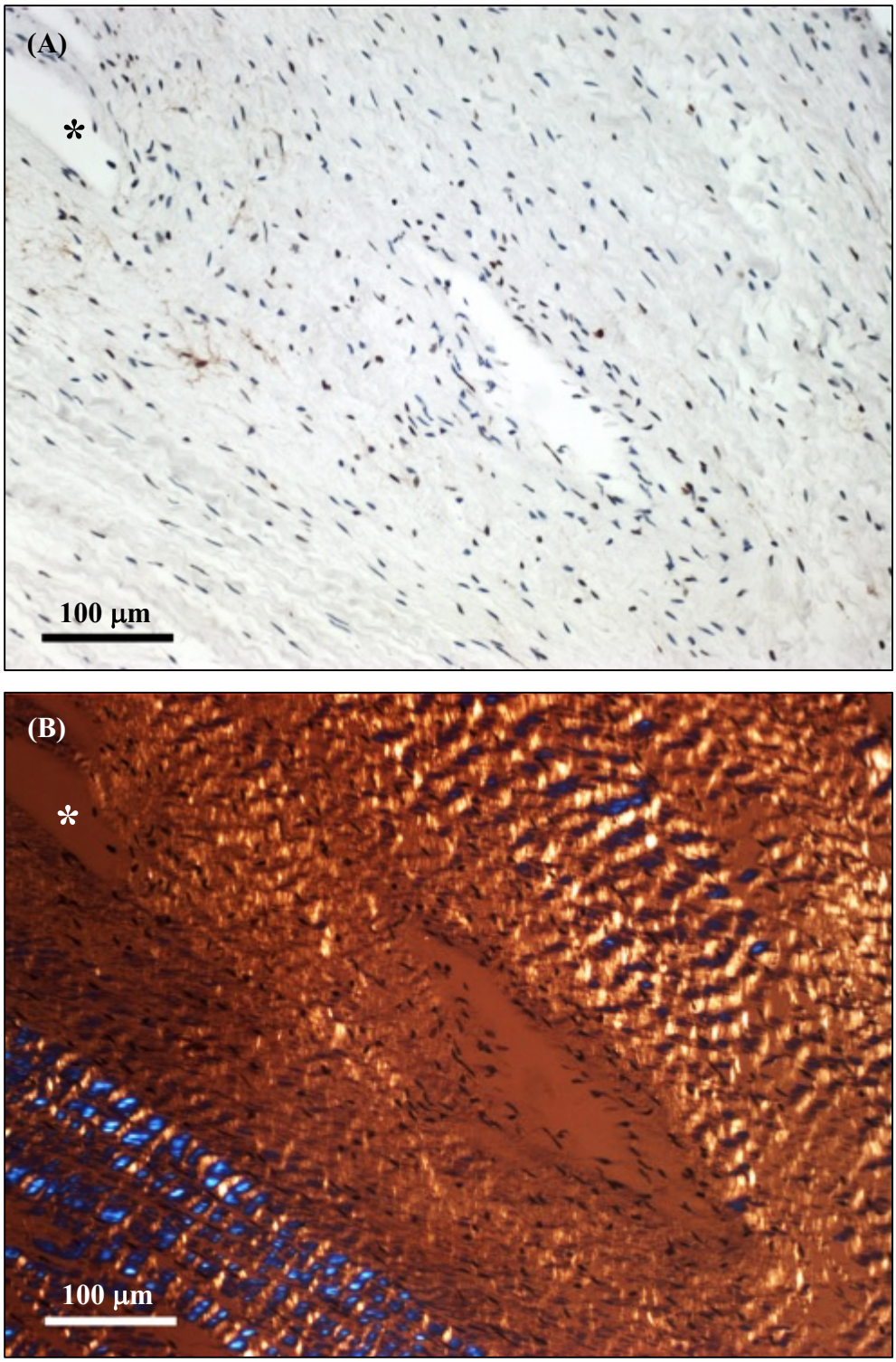

Figure 4.28: α-SMA immunostained longitudinal sections taken through the same chorda bifurcation from a non-pregnant heifer under (A) brightfield illumination and (B) polarized light. A tissue perforation can be seen below the bifurcation near aVICs, with a decrease in surrounding collagen birefringence. aVICs appear brown (stained with DAB) and qVICs are counterstained purple with hematoxylin. Bifurcations are marked with an asterix (*).

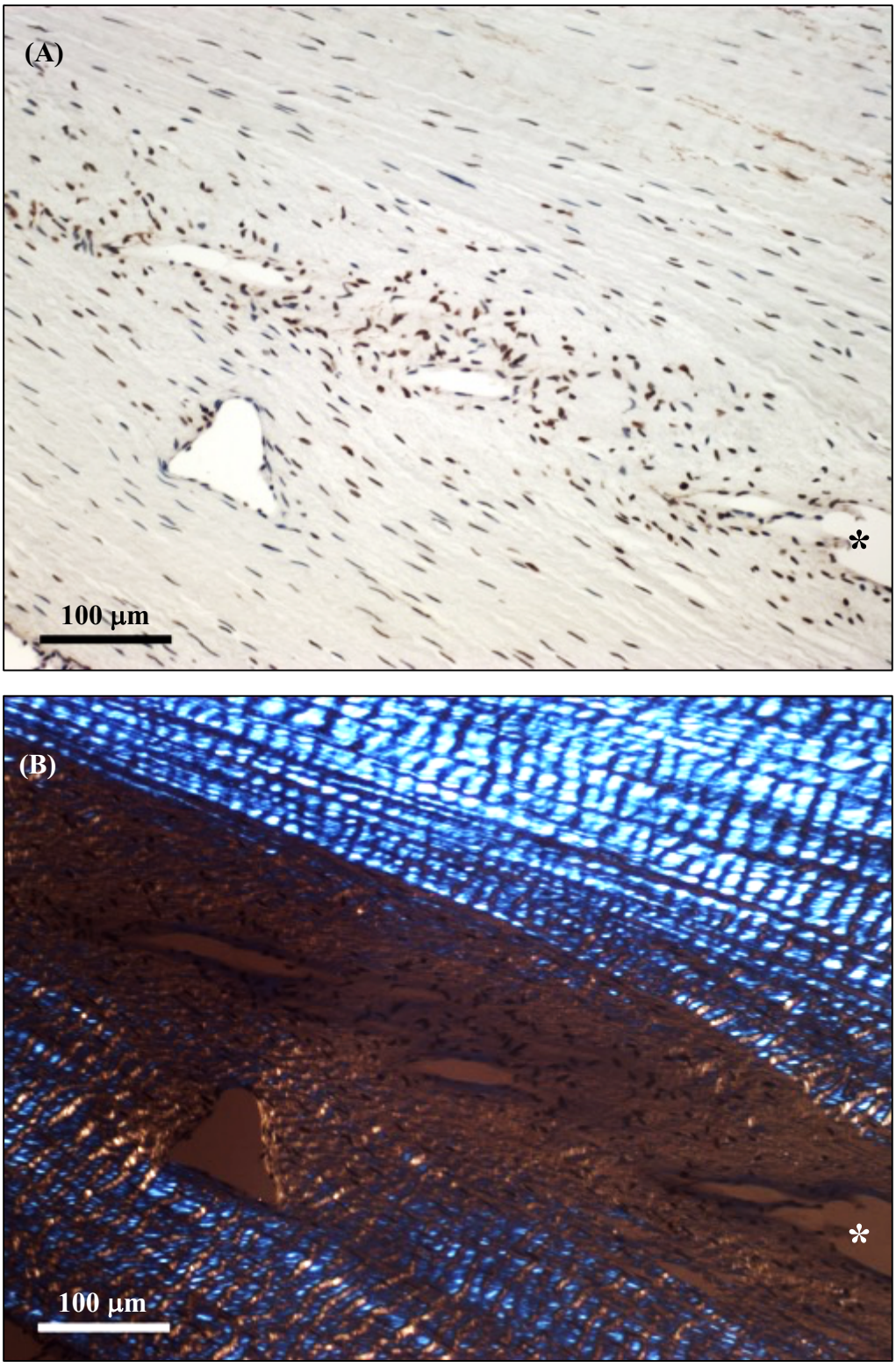

Figure 4.29: α-SMA immunostained longitudinal sections taken through the same chorda bifurcation from a pregnant cow under (A) brightfield illumination and (B) polarized light. Multiple tissue perforations can be seen below the bifurcation surrounded by a dense cluster of aVICs, with a loss of collagen birefringence. aVICs appear brown (stained with DAB) and qVICs are counterstained purple with hematoxylin. Bifurcations are marked with an asterix (*).

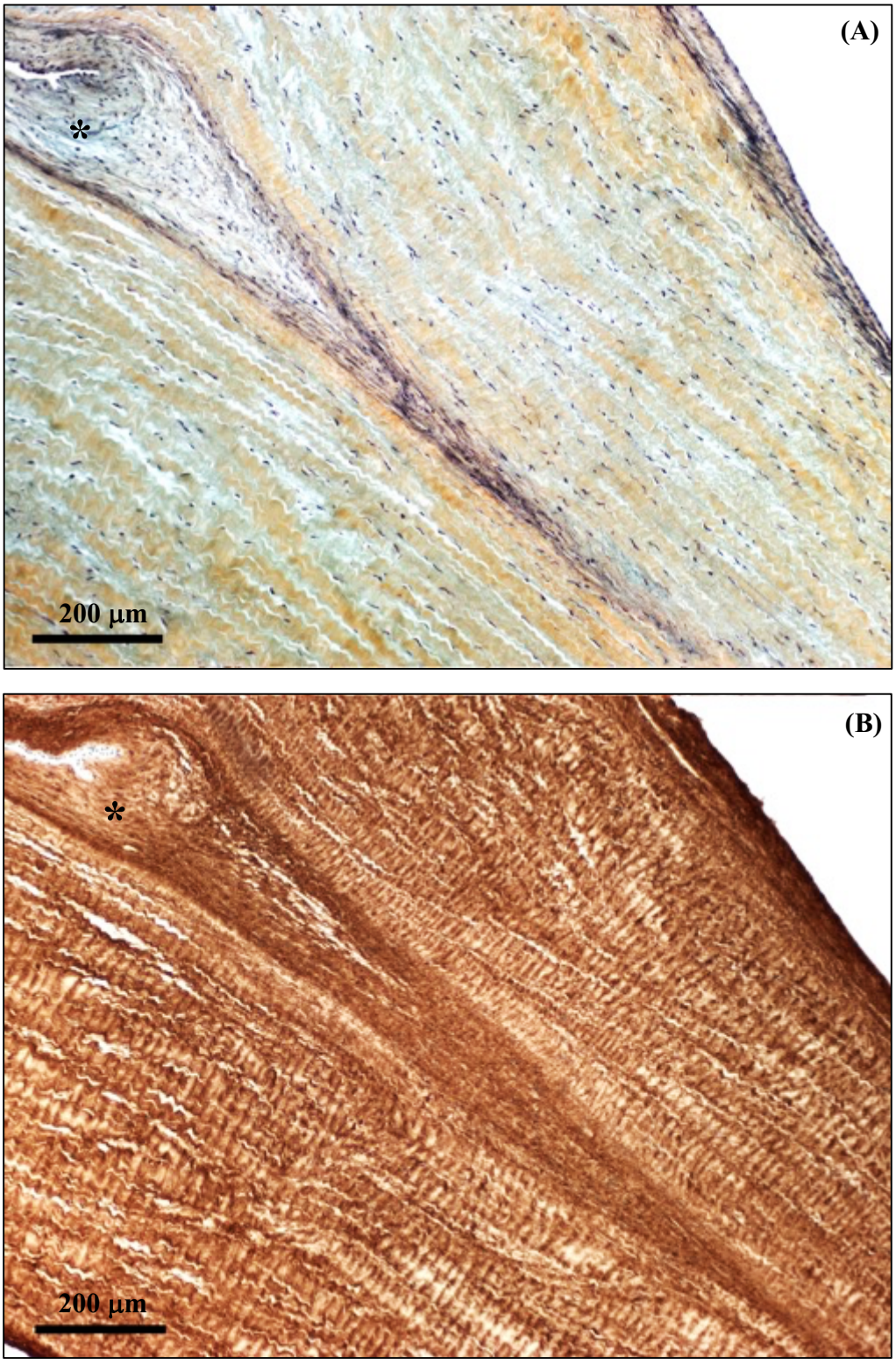

Figure 4.30: Movat Pentachrome (A) and periostin-stained (B) longitudinal sections through the same chorda bifurcation. Periostin expression is more intense (darker brown DAB staining) in areas with elastin, both at the bifurcation and around the outmost chordal layer. Bifurcations are marked with an asterix (*). Yellow=collagen, blue/green=GAGs, black lines= elastin fibers, purple dots=cell nuclei.

Chapter 5
Discussion

This study is the first of its kind to investigate the remodelling potential of maternal chordae tendineae. The objective of this work was to uncover the molecular, cellular, and tissue-level contributions responsible for the chordae multiplication observed in pregnancy using a thorough thermal and histological analysis. The thermal stability of collagen in chordae taken from pregnant cows was surprisingly similar to that of heifers, despite a comprehensive spatial (leaflet to papillary muscle) sampling process. Chordae bifurcations were shown to be unique from the surrounding tissue, containing higher concentrations of GAGs and cell nuclei, and, under some circumstances, a deep progression of elastin fibers into the tissue center – features all shared between non-pregnant and pregnant animals. Furthermore, both quantitative and qualitative collagen crimp measurements, α-SMA analyses, and periostin staining profiles were unexpectedly similar between pregnancy groups. The astonishing closeness of heifer and maternal chordae unveiled herein is far unlike previous observations of the mitral valve *leaflet*, which detailed profound morphological, biochemical, and biomechanical differences. The remodelling of chordae tendineae in the maternal bovine heart is, by comparison, an undoubtedly unique process.

5.1 **Chordae Number**

The original, pioneering maternal mitral valve remodelling study by Wells et al. (2012)[166] showed a 22% increase in the number of chordal attachments to the anterior leaflet in pregnancy, likely in response to the elevated mechanical stresses that accompany annular orifice expansion and ventricular dilation. The current investigation supported this finding, showing an overall 18% increase in the total number of chordal attachments, despite drastically different counting methods. Wells et al. (2012) classified and counted chordal attachments based on their diameters: chordae between 1-3mm

("secondary chords") made one grouping, and chordae <1mm ("tertiary chords") formed the other, while any translucent chordae and the finest side branches were excluded from their counts. Counting in this study was more comprehensive and inclusive based on chordae type: either basal or marginal (strut chordae were negligible in chordae counts as there is always 2 per valve) with all smallest side branches and translucent chordae included. Indeed, marginal chordae are certainly the smallest of all types, with an average diameter in pigs of approximately 0.69 mm[72] with many appearing translucent. On the basis of size and opacity, it's likely that the methods used by Wells et al. (2012) inherently omitted many marginal chordae from the overall chordae counts, and rather incorporated primarily basal chordae simply grouped into different size categories. Therefore, a more accurate data comparison would be the 17% increase in basal chordae observed here, compared to their 22% increase observed by late pregnancy. The counts of this study were also not binned by gestational age (i.e., early and late pregnancy groups), which could explain the slightly lower increase observed, as counts from early pregnant animals would be mixed with those from late pregnant cows.

In fact, when plotted against crown-to-rump lengths, there was no significant relationship observed between the number of chordal attachments and gestational age, unlike the linear increase observed previously[166]. The large valve-to-valve variation in heifer chordae numbers is likely responsible for this poor correlation. In non-pregnant animals of the same age, chordae counts differed considerably; in some cases, the percent difference between total chordae numbers between similarly aged heifers was over 45%. Such drastic differences in starting chordae numbers upon conception, and depending upon when the maternal valves were harvested during gestation, likely masked any potential correlation of total chordae number with gestational age. Additionally, the reproductive history of pregnant cattle was unknown, i.e. there was a potential for previous pregnancies. This may have influenced the counting data, as its currently uncertain whether the increase in maternal chordae number is reversed post-partum, or if this structural elaboration remains a permanent feature of the valve. For future experiments, chordae number relationships throughout pregnancy should rather be based upon specific cardiac dimensions such as heart mass, ventricular diameter, or annular orifice circumference – obtaining reproductive histories as possible.

Having defined marginal chordae data with respect to chordae counts is beneficial, as we now know that the increase in chordae number appears globally over the anterior leaflet, and is not merely restricted to the basal chords. This increase not only makes sense in terms of coping with heightened mechanical load, but also in terms of maintaining proper valve anatomy and function. An increase in leaflet area without a corresponding increase in basal chordae would leave the leaflet belly relatively unsupported and vulnerable to inappropriate bulging. There is evidence to show that deficiencies in chordae branching patterns could lead to a weakened central leaflet core, leaving an individual more susceptible to eventual mitral valve prolapse[70]. The remarkable lack of mitral regurgitation in pregnancy[185] could consequently be the result of adaptive chordae multiplication that serves to mechanically support the expanding leaflet tissue. However, chordal *density* decreases throughout gestation, leaving fewer chordae per unit area of anterior leaflet[166]. The increase in marginal chordae, whose duty is to maintain leaflet coaptation, could compensate for the decrease in chordal density in the face of intensified hemodynamics to preserve valve integrity. The tricuspid valve, although to a lesser extent than the mitral valve, also undergoes a significant increase in leaflet area[196], yet 95% of woman experience regurgitant flow through their tricuspid valves during pregnancy. The number of tricuspid chordae have not been counted and compared to non-pregnant animals; it's possible that there is a lack of adaptive chordal remodelling on the right side of the heart that contributes to such tricuspid insufficiencies. This is supported by a recent study comparing all four heart valves during pregnancy. Pierlot et al. (2015) showed that although the tricuspid valve does indeed experience pregnancy-induced remodelling, this response is significantly diminished in comparison to the pulmonary, aortic, and mitral valves[196].

The only other scenario under which chordae multiplication has been documented (albeit vaguely), is during fetal development. As the fetus develops and grows, many hemodynamic and structural changes take place that mimic those seen in the maternal heart. Blood pressure increases with gestational age from 28 mmHg at 20 weeks to 45 mmHg at 40 weeks, aortic diameter increases, arterial compliance increases, and peripheral resistance decreases[213,214]. Furthermore, combined cardiac output and blood volume both increase as the fetus grows[214-216] and undeniably, the fetal heart also

increases in size as it approaches full-term. The drastic increase in heart size during development inevitably leads to concomitant enlargements of the mitral apparatus including the annulus, valve leaflets, and chordae tendineae. Collectively, these developmental hemodynamic and structural changes (for the same reasons outlined for pregnancy) would lead to increased mechanical stress on the mitral valve and have implications for fetal mitral valve remodelling. Indeed, multiple studies have shown that embryonic hemodynamic conditions, shear stress, the heart's own mechanical contractions, and overall increased mechanical stress on primordial leaflet tissue influence the development of the endocardial cushion (a structure in the earliest stages of heart development giving rise to the mature heart valve) and stimulate normal valvulogenic events[217-220].

The chordae tendineae have received relatively little research attention during fetal and postnatal development, with only limited studies describing their detailed formation and growth. In humans, chordae first appear in the fetal heart at 10 weeks into the gestational period[221]. They form via gap formations in the ventricular layer of the endocardial cushion, which at this stage is resting on top of and continuous with that of the papillary muscles. The cushion tissue around the gaps continues to lengthen and migrate away from the papillary muscles, forming tissue strands linking the to-be leaflet tissue and papillary muscles. At 15-19 weeks, a mini-mature valve has now formed with multiple chordae extending from the papillary muscles to the leaflets[221]. Scanning electron microscopy of developing chordae inside the chick embryo has been described similarly[222]. Tissue connecting the valve cusps to the papillary muscle develops a series of ridges. The ridges themselves later become isolated chordae tendineae, whilst the valleys between develop perforations and eventually disappear. Endocardial cells are present nearby perforations, suggesting a programmed cellular event. Perhaps most interestingly with regards to the current study, is a "scission" of the first-to-form primary chords. Once the primary chordae form, secondary and tertiary chords develop through subdivisions, or splitting of the existing chordae[222]. The central hypothesis of this work was that the maternal increase in chordae number results from the splitting of existing chordae. It was believed that a recapitulation of developmental chordal scission and subdivision-like events could be reactivated in the maternal heart stimulated by similar

volume loading and cardiac expansion to that observed in the fetus. However, histological signatures of chordae splitting at bifurcations were seen in non-pregnant *and* pregnant animals (discussed later below), suggesting that this initial developmental mechanism may persist into adulthood as a means of routine tissue turnover even in non-pregnant animals, and may instead be just *enhanced* in the maternal heart. Surely, a better understanding of fetal chordae splitting would help us expand our knowledge of maternal chordae physiology.

5.2 **Thermal Stability**

Collagen remodelling – in a variety of different tissues including heart valves – can be detected via changes in its thermal properties. This concept is based off the polymer-in-a-box theory for the thermal stabilization of collagen molecules[47]. This mechanism relies on the molecular packing and overall lateral spacing of neighbouring molecules within the fiber lattice. One region of collagen type I in particular – the thermally labile domain – is a small (65 residue) hydroxyproline-free sequence where α-chain dissociation is believed to initiate[223]. When neighbouring collagen molecules are more closely packed, the configurational entropy of the thermally labile domain is reduced, requiring a greater energetic input to unfold and initiate collagen denaturation[47]. Actively remodelling tissues are believed to have an increased lateral spacing, and thus commence denaturation at lower temperatures. Any newly synthesized collagen also takes time to be cross-linked in place and mature, and therefore this population inevitably displays a lower thermal stability as intermolecular cross-links themselves draw molecules closer together[224]. Indeed, Aldous et al. (2009, 2010)[45,49] showed a clear relationship between molecular stability of heart valve collagen and their respective mechanical loading environments. Fetal aortic and pulmonary valves experience similar transvalvular pressures. Once born, the transvalvular pressures in the neonate change dramatically: transvalvular pressure becomes higher across the aortic valve relative to the pulmonary valve. They showed that during the fetal-to-neonatal transition, aortic valve collagen was less thermally stable than its left-side counterpart[49]. In line with these observations, a prior study showed an inverse relationship between *in vivo* transvalvular

pressures and denaturation temperature across all four adult valves in the bovine heart, where valves experiencing higher transvalvular pressures displayed the lowest denaturation temperatures[45]. Overall they concluded that heart valves – in addition to their constant cyclic loading environment – experience load-dependent collagen turnover. Higher loads increase the accumulation of molecular damage, which leads to molecular destabilization through increased lateral spacing and active cellular remodelling.

The chordae, due to increased orifice area and ventricular dilation, would experience higher mechanical loads in pregnancy. In accordance with the aforementioned studies, one would expect the thermal stability of collagen in maternal chordae to decrease; however, this was not observed in the present investigation. The thermal stability as measured by T_{onset}, T_{peak}, and specific enthalpy, was surprisingly unchanged between heifers and pregnant cows. The FWHM however was decreased in pregnancy (discussed later below). It's currently unclear as to why no decrease in thermal stability was detected between pregnancy groups. One possibility is that the mechanism underlying the increase in chordae number does not manifest itself as such, and does not require substantial collagen remodelling throughout the bulk of the tissue to occur. The remodelling may very well be extremely localized only to the proceeding split. In this scenario, DSC would consequently be an insignificant metric. Perhaps DSC detectable levels of collagen remodelling are simply not occurring in maternal chordae and the process of chordae remodelling is more passive in nature, mediated through primarily non-cellular mechanisms such a tissue micro-tearing at the leaflet surface due to increased mechanical loading.

It's curious however, that T_{onset} was significantly lower for insertion sites compared to straight segments in pregnant animals only. Temperature of onset (T_{onset}) represents the temperature at which the least thermally stable collagen molecules within the sample begin to unfold. Initially a lower T_{onset} seems reasonable, as the insertion sites (being adjacent to the leaflet) are regions of more active collagen turnover and would therefore display a lower thermal stability (see below). Yet, insertion site thermal stabilities were similar between heifers and pregnant animals. Based on the average values for T_{onset}, it appears the maternal straight segments actually became more thermally stable relative to all other sampling locations, losing a sub-population of their

least thermally stable collagen. This could suggest a structural reinforcement of straight segments through increased molecular cross-linking prior to chordal splitting to help compensate for the increased maternal mechanical load. It's important to note that all maternal DSC chordae samples were acquired from late-pregnant cows (over 7 months into gestation). Biphasic shifts in leaflet extensibility were observed in the mitral anterior leaflet, whereby the initial decrease in leaflet extensibility reversed to pre-pregnant values by late-pregnancy[166]. Since all the maternal DSC data were acquired based on a narrow range of late-pregnant cows, it's quite possible that early shifts in collagen thermal stability may be occurring during the first few months of gestation and begin to reverse near term. Any changes of this nature would have been missed in the current investigation.

In contrast to the chordae, significant shifts in collagen thermal stability were seen in the mitral anterior leaflet[166,187] during pregnancy. As measured by HIT analyses, there was over a 2°C decrease in collagen denaturation temperature. Once again, this was attributable to increased collagen turnover as a result of increased mechanical loading. It's curious that two such interconnected and dependent structures – the chordae tendineae and the leaflet – could exhibit such drastically different thermal responses in pregnancy. Granted, the denaturation response observed for the leaflet was measured using HIT, while the results herein were determined using DSC. Fundamentally, HIT and DSC measure collagen denaturation on different size and timescales. In HIT, a tendon sample is submerged in a water bath and isometrically constrained between two clamps. When the water bath is heated through to its denaturation temperature, the input of thermal energy drives the molecular uncoiling of the tendon collagen. The tendon however is isometrically constrained and therefore resists the shrinkage associated with collagen denaturation, generating a measurable tension via the coupled force transducers. HIT therefore measures the tendon tension generated due to the energetically favourable uncoiling of collagen α-helices. DSC on the other hand, records the heat flow necessary to denature collagen molecules within a given (unconstrained) sample. If anything, DSC is a more sensitive means by which to examine collagen denaturation, as changes in heat flow prior to and at the very commencement of denaturation can be measured, whereas measureable tension in a bulk tendon sample in HIT is undetectable at this stage[225].

Consequently, the difference in methodologies employed to evaluate thermal changes in maternal mitral valve collagen between leaflets and chordae should not explain their seemingly unique thermal denaturation responses, but rather emphasizes their exclusive remodelling profiles in pregnancy. The principal tensile loading patterns endured by the chordae are unlike the multi-modal cyclic loads imposed on the leaflet which include tensile, compressional, shear, and flexural forces[11]. Such a barrage of mechanically diverse forces, all of which are potentially amplified during pregnancy, could drive more physiological remodelling than observed in the chordae tendineae.

If chordae are indeed splitting at the leaflet interface and propagating down, it was predicted that chordae sampled closer to the leaflet surface may have been more recently remodelled and thus, display a lower thermal stability compared to more mature samples taken near the papillary muscles. This was not what was discovered. Instead, there was an unexpected correlation between T_{onset}, T_{peak}, and specific enthalpy with sampling distance from the leaflet surface – in non-pregnant animals only. Values of T_{onset} and T_{peak} *decreased* with distance in heifers, while specific enthalpy increased; there were no significant thermal trends with distance observed in pregnancy. Although statistically significant, only 17-23% of the data's variability was explained by the linear model in heifers, suggesting this relationship be interpreted with a level of caution. It hints at however, that there is a greater degree of molecular stabilization towards the leaflet. This could be the result of a spatially heterogeneous population of collagen cross-links with distance. In accordance with the polymer-in-a-box theory, such cross-links would grant variable degrees of lateral spacing between neighbouring molecules (influencing intermolecular hydration) and differentially influence the onset of thermal denaturation[224]. The absence of these thermal trends in pregnancy could stem from the significantly lower FWHM. Endotherm FWHM describes the distribution of thermal stabilities within the sample. At first, it's curious how a significant change in the FWHM could occur given the other three thermal metrics (T_{onset}, T_{peak}, specific enthalpy) were found to be insignificant; however, the FWHM parameter itself is inherently based upon both the downward (heat flow increasing) and upward slope (heat flow decreasing) of the DSC endotherm. Small, insignificant changes in T_{onset} and T_{peak} could collectively influence and sum to a significant change in the FWHM. There was also no metric to

specifically assess the back portion of the curve, which may have had an impact on the FWHM result. Regardless of the influence, a lower FWHM in pregnancy is indicative of a more homogeneous population of collagen molecules and therefore, any thermal differences with distance once observed in the heifers may have equilibrated towards the end of gestation. Unfortunately, the cross-link profile of bovine chordae – or that of any other species – remains unknown, and therefore such a hypothesis remains mere speculation.

The biomechanical properties, composition, structure, and functional roles of different chordae types is becoming well known. However, to the author's knowledge, this work has shown the first-ever evidence for differences in thermal properties by chordae type. Relatively low values of T_{onset} and T_{peak} affirmed strut chordae as the least thermally stable, while the same parameters for marginal chordae were over 2°C higher. Basal chordae showed an intermediate thermal stability between that of the strut and marginal chords. Once again, a look into *in vivo* loading patterns may explain the thermal variation between chordae types. Numerous porcine studies have investigated the magnitude of peak systolic tensile load experienced by the anterior strut and marginal chordae using miniature force transducers. An *in-vivo* porcine model by Lomholt et al. (2002) showed that strut chordae encountered tension over 3-fold higher than marginal chordae (0.7N vs. 0.2N)[76]. He and Jowers (2009) used intact porcine mitral valves (left inside the heart, connected to a water reservoir through the aorta) to compare strut and marginal chordal loading. They similarly concluded that the strut chordae experience significantly higher tensile loads than marginal chordae (1.0N vs 0.1N)[93]. As discussed previously, higher *in vivo* loading within heart valve tissue leads to higher collagen turnover and decreased molecular stabilization, seemingly explaining the trend in thermal stabilities observed between the strut and marginal chordae. However, these biomechanical studies only report tension magnitudes and do not consider chordal stresses (accounting for differences in the cross-sectional area of the individual chordae types). Using average porcine chordal cross-sectional areas given for strut (2.05mm^2) and marginal (0.38mm^2) chordae provided by Liao and Vesely (2003)[72] and the measured force values provided above, chordal stresses can be calculated. When using the force measurements given by He and Jowers (2009), the strut chordae see nearly double the

mechanical stress of the marginal chordae (0.49 MPa vs. 0.26 MPa); however, using the force data from Lomholt et al. (2002), strut and marginal chordae experience a stress of 0.34 MPa and 0.53 MPa respectively. It's therefore difficult to state for certain whether mechanical loading (and thus tissue remodelling rate) can be attributed to the observations in the thermal data. In addition to the imposed cyclic tensile stresses, specific loading times and patterns could impact tissue remodelling and thus thermal stabilities. For example, strut chordae experience peak loading during systole, but also remain weakly loaded near the insertion zone during diastole[85]. Marginal chordae are the first to be loaded during systole as the coaptation surface first forms, but as ventricular pressure rises, progressively thicker basal and strut chords are recruited to alleviate marginal stresses[226]. These differential loading profiles would likely influence the accumulation of molecular damage and tissue remodelling between chordae types.

Alternatively, differences in tissue hydration could explain the differences in thermal stability observed between chordae types. The few studies that have investigated chordae water content have shown minimal differences in hydration between types. Grande-Allen et al. (2004)[56] showed a small, but significantly lower water content in basal chordae compared to marginal (73% vs. 77%), while Liao and Vesely (2004)[54] showed the water content was equal between strut, basal, and marginal chordae at 78%, 77%, and 77% respectively. Based on the current literature, differential water content between the three chordae types would likely not explain the current results; however, the tissue preparation prior to the DSC run itself may have influenced tissue hydration. Strut chordae are the largest chordae, followed by the intermediately sized basal chordae, and finest marginal chords. This pattern was correspondingly upheld in DSC sample collection, with significantly different (p<0.0001) average sample masses (± SD) found for strut (8.4 ± 3.4), basal (3.7 ± 2.6), and marginal (1.3 ± 1.0) chordae. With a higher surface area to volume ratio, the marginal chordae samples were more vulnerable to drying out when blotted and weighed for DSC before being hermetically sealed into their DSC pans. Despite attempts to minimize their air exposure time, it's possible marginal chordae lost considerable water content before commencing the DSC temperature ramp. In fact, a loss of hydration in the marginal chordae explains the trend in all four DSC parameters in accordance with a paper by Miles and Ghelashvili (1999)[47]. In their study,

they progressively dehydrated rat tail tendons for DSC and discovered that with decreasing hydration, both T_{peak} and the FWHM increase, while the enthalpy of denaturation decreases – mimicking the results observed herein for marginal chordae relative to strut and basal chords. This was based upon fiber dehydration causing a loss of hydrogen bonding between α-chains (and thus fewer needing to be broken to achieve denaturation), and decrease in the interaxial spacing (in accordance with the polymer-in-a-box theory) between collagen molecules in the fiber, which is directly related to its volume fraction of water[47]. With their initial wet weights known, the chordae samples could be freeze-dried and weighed to determine their respective water contents to help elucidate any differences in tissue hydration. The significantly different sample masses between chordae types (mentioned above), could also be a confounding factor in the DSC analysis itself. Grossly different sample masses would effectively alter the DSC scanning rate, possibly changing the overall DSC endotherm and consequently, any quantitative parameters. Future work could include testing a range of chordae sample masses of the same chordae type (e.g. multiple sample masses of strut chordae only) to see how the DSC measurements change with varying sample mass.

Unfortunately, DSC yields no direct, tangible information with regards to collagen cross-linking which could also explain these thermal trends. The higher modulus observed in chordae with smaller cross-sectional areas (marginal) has largely been attributed to their smaller crimp period, relatively small fibril diameters, high fibril density, and increased proteoglycan/GAG content[54,72]. Alternatively, the cross-link population in marginal chordae could be relatively more mature and thus contribute to their observed tissue stiffness and coincident increase in thermal stability. A stiffer tissue and possibly more mature cross-link population would be beneficial to the marginal chordae, as their role is to maintain proper leaflet coaptation; a more compliant tissue may leave the valve more susceptible to improper closure. A future detailed profiling of chordae collagen cross-link population through liquid chromatography analyses would certainly be valuable.

5.3 **Collagen Crimp**

In late pregnancy there is a dramatic increase in collagen crimp length and loss in the percentage of leaflet area occupied by crimped tissue. Near-term collagen crimp length is nearly 3-fold longer than what is observed in non-pregnant animals, and this is accompanied by a 45% decrease in crimp area[186,187]. This remarkable transformation of collagen architecture, along with an increase in collagen content, is thought to contribute to leaflet expansion, which itself compensates for annular dilation (recovering some of the leaflet's functional reserve) and likely facilitates leaflet coaptation. Despite such changes in the leaflet, collagen crimp wavelength and percent area were unchanged in maternal chordae. The eccentric hypertrophy and ensuing papillary muscle displacement that presumably follows left ventricular dilation during pregnancy, must, inevitably, result in a lengthening and/or stretching of the maternal chords (providing the papillary muscles themselves do not grow). Although this elongation was hypothesized to be achieved partially through a collapse and loss of collagen crimp in maternal chordae, this appears not to be the case. It's possible that an increase in collagen synthesis could contribute to their necessary lengthening while maintaining overall crimp wavelength. This contradicts the thermal data however, which suggests no significant increase in newly synthesized collagen in maternal chords. A more accurate assessment of newly synthesized collagen would need to be performed using a Sircol assay for acid and pepsin-soluble collagen to test this hypothesis, along with corresponding length measurements of maternal chordae. Sampling directly at the papillary muscle-chordae interface was not performed here, and may be a region of future interest with respect to collagen synthesis and potential chordae lengthening.

In patients with functional mitral regurgitation, the idea of compensatory leaflet enlargement is not a novel concept[121,227]. In these patients, pathological ventricular remodelling occurs, leading to papillary muscle displacement and a tethering of the mitral valve leaflets. Tethering moves the coaptation surface below the annulus, restricting leaflet closure and resulting in inappropriate retrograde flow. The observed increase in leaflet area in patients with functional mitral regurgitation is believed to be an adaptive remodelling response to re-establish proper leaflet closure and prevent mitral

regurgitation[121,227]. Only recently has the notion of chordae elongation been proposed as an adaptive mechanism to reduce mitral regurgitation. A study by Obase et al. (2015)[228] measured chordal lengths in patients with functional mitral regurgitation relative to healthy controls. Their results suggested that chordae have the capacity to elongate to reduce regurgitation, in a similar fashion to how the leaflet area expands. No mechanistic insight was provided as to how this elongation may occur; however, in the future, this process could be compared to the expected chordal elongation in pregnancy. Along with the documented increase in leaflet area and chordae number, chordal elongation could be a significant contributor to maternal mitral valve competence and unquestionably deserves future research attention.

The working concept of maternal chordae splitting as a mechanism for the increase in chordae number may in fact not influence crimp wavelength and percent crimp area at all; the lack of change in these parameters between heifers and pregnant cows does not exclude this interpretation. If splitting occurs at leaflet insertion sites and at existing bifurcations propagating towards the papillary muscle, the crimp wavelength of the existing, potentially splitting chordae could simply be maintained amongst the two, newly split chords. Such a division may simply not yield any detectable changes in the crimp measurements. Alternatively, if the new chordae develop *de novo* at the leaflet surface, then one might expect changes in crimp patterns. Dickinson and Vesely (2012)[229] reported microstructural changes in rat chordae during postnatal development, evaluating crimp wavelength with chordal maturation. The first chordae to develop (postnatal day 3) lacked crimp, and consisted of a thin homogeneous collagen core. As time progressed the chordae matured, developing their characteristic collagen crimp, with a progressive increase in fiber alignment and density until postnatal day 30 where they then fully resembled adult chordae. The crimp wavelength was also observed to increase significantly with age. Accordingly, a similar process might be unfolding in newly evolved maternal chordae. It's worth noting that there was a subset of small, short chordae near the leaflet whose crimp periods could not be measured as a clear crimp pattern was not discernible. In light of the evidence by Dickinson and Vesely (2012)[229], these chordae very well may have been new, recently-born branches that had yet to undergo fiber maturation. Despite the comprehensive histological sampling protocol

employed in this work on a valve-to-valve basis, the entire valve (and all its chordae) could not reasonably be sampled within the timeframe for this project. With that in mind, the necessarily limited regions selected for histology were likely overwhelmed by existing mature chords and as a result, no detectable changes in crimp parameters between pregnancy states. Additionally, the timeframe of maturation (less than 30 days in rats), could have also contributed to the difficulty of capturing this phenomenon using such a discrete sampling procedure, as opposed to a more idealized longitudinal approach.

The study by Dickinson and Vesely (2012)[229] mentioned above was motivation to record the distance at which crimp measurements were taken from the leaflet. If the increase in chordae number is more of a *de novo* construction off existing chordae at the leaflet surface rather than a splitting event, then the crimp period (based on postnatal microstructural changes in the rat chordae crimp described above) would be shorter in smaller chordae in close proximity to the leaflet surface. Although our findings did not support this hypothesis, crimp wavelength did unexpectedly show a trend with distance unrelated to pregnancy state: as distance from the leaflet surface increased, so too did the crimp wavelength in both strut and basal chordae. This was not a subtle change, but rather a near doubling in crimp wavelength for basal and strut chordae respectively. Marginal chordae, being anatomically smaller and never inserting directly into the papillary muscles, only rarely had crimp values recorded greater than 1cm away from the leaflet and hence, no trend with distance was observed. This report of a spatially non-uniform crimp wavelength is previously unreported in the chordae literature. In terms of valve biomechanics, this arrangement could be profitable. A smaller crimp period in close proximity to the leaflet – and thus a larger reserve of stored tissue – could ease stress transfer from the chordae to the leaflets during valve closure.

The crimp wavelengths of different chordae types have been previously reported; however, the results found in this work conflict with the existing literature. It has been reported in pigs that smaller diameter chordae (marginal) have significantly longer crimp lengths than do larger diameter (strut) chordae, accounting for differences in their extensibility[72]. The opposite trend was discovered via the polarized light analyses of this work. Strut and basal chordae had similar crimp lengths at approximately 23μm, while

marginal chordae were significantly shorter at 16μm. One possible explanation for this discrepancy could lie in where their samples were taken along the length of each chorda. This work has clearly shown that crimp wavelength depends upon sampling distance from the leaflet. Thick, straight segments of chordae are preferable for histological sectioning and subsequent analyses and therefore, may have been preferentially harvested. This may have influenced the distances at which chordae crimp was measured in the previously published study[72]. With respect to chordal mechanical properties, a shorter crimp length for marginal chordae, as determined herein, would, according to the work by Liao and Vesely (2003)[72], result in a less extensible structure. However, this was based on the assumption that the amplitude of collagen crimp was the same between all chordae types, which may very well not be the case. Therefore, the longer crimp length observed in the current work in strut and basal chordae could still follow their well-known trend of increased extensibility by having a more pronounced crimp amplitude relative to the marginal chordae. Unfortunately, crimp amplitude is a difficult metric to quantify histologically as it will change based upon the fiber orientation relative to the cutting plane when sectioned.

Chordae collagen crimp was quantitatively assessed at straight tissue segments, but was also qualitatively assessed at leaflet insertions sites and bifurcations. Overall general descriptive chordae histology is scarce in the literature; histology capturing insertions sites is increasingly rare, while histology directed at chordae bifurcations has never been published. Collagen fibers at leaflet insertion sites were splayed and fanned out as they merged with the leaflet tissue, showing a smearing and loss of crimp in select fibers. These results match nicely with the work of Chen et al. (2004)[230], that investigated the collagen structure of the porcine mitral valve leaflet-strut chordae transition zone. In their work, they reported a spatial variation of collagen fiber orientation and degree of alignment moving progressively from the annulus, to the leaflet, and finally into the chordae. They too, describe the collagen fibers as fanning out towards the leaflet at the chordal insertion site, providing a mechanically advantageous distribution of load into the adjacent leaflet tissue.

Chordae bifurcations – in both pregnant and non-pregnant animals – displayed a unique orientation of collagen fibers and in some cases, a lack of collagen content and/or

organization altogether as evidenced under polarized light. In short, polarized light microscopy works in the following way. When the microscope's light source hits the first polarizer, only light in a single plane is transmitted through to the given sample. Tissues rich in fibrillar collagens are optically anisotropic materials that are capable of rotating plane-polarized light; this rotation is dependent upon the orientation of collagen in the tissue. Light rotated by the sample reaches the second filter positioned at 90° with respect to the first polarizer, ensuring only re-directed light is transmitted. A loss of birefringent signal (black appearance) then means the direction of the incident plane polarized light was not altered and therefore, the tissue lacks optical activity and organization[231]. To be birefringent thus requires sound collagen organization at the molecular level (quasi crystalline assembly). Polarized light microscopy revealed a loss of birefringence at many bifurcations. This was not surprising given the results from serial sections stained with Movat Pentachrome that showed a high concentration of GAGs in these regions (which would not illuminate under the polarized light). However, some bifurcations contained collagen yet lacked birefringent properties, indicating that the collagen was disordered at bifurcation zones. A lack of organized, crimped collagen could be indicative of active collagen synthesis and/or tissue degradation – signs of ECM remodelling. The disturbed collagen organization at bifurcations was the first sign of tissue turnover and remodelling in this work supporting a possibly splitting chorda structure, found surprisingly in both experimental groups. With disorganization frequently on a scale of only 0.1 mm^2 or less, it's possible that this relatively small collagen population was undetectable at bifurcations in the DSC analysis, with organized, seemingly more mature tissue dominating the DSC sample. This could explain the non-significant differences between sampling locations despite these obvious structural differences. As demonstrated, collagen disorganization occasionally extended deep into the tissue center, which could indicate the propagation of a splitting chorda through collagenous degradation.

Alternatively, the distinct bifurcation morphologies could be related to local tissue stresses. Some bifurcations showed disturbed collagen, while others showed crimped collagen fibers on either side of the bifurcation merging seamlessly at the common trunk segment. In some cases, crimped fibers curled directly into and molded around the

bifurcation tip. As collagen fibers are known to align with the direction of applied stress[232,233], this suggests oblique tensile forces (to the principal longitudinal axis) are present. Bifurcation loading could also be complex and multi-modal on a bifurcation-to-bifurcation basis dependent upon anatomical valve location, explaining the range of bifurcation morphologies. Unsustained tension or other multidirectional forces may not leave sufficient time for fiber orientations to develop, and thus manifest locally as unorganized collagen. It should be noted that the collagen fibers (due to the force distribution at the bifurcation) could very well have intact *molecular* organization yet lack birefringence based on fibre orientation. Bifurcation fibers may be present in various interweaving non-longitudinal orientations to appropriately bear load – some of which would consequently appear dark under polarized light due to their alignment relative to the polarizer. Therefore, on its own, a lack of birefringence does not necessarily indicate collagen remodelling at bifurcations; however, this argument becomes stronger alongside the complimentary histological data (Movat Pentachrome, α-SMA, periostin) presented below.

5.4 **Movat Pentachrome**

Until now in this thesis, there has been minimal evidence to distinguish heifer and maternal chordae given the similarities in their DSC data, crimp measurements, and bifurcation morphologies. That said, a plethora of novel, physiologically valuable insight has been gained into native chordae thermal properties and structure. This motif continues with the discussion of the Movat Pentachrome staining, used to gain a broad overview of chordae ECM composition. Although not bovine, other chordae histological studies have provided a look into their bulk compositional makeup. Straight segments of chordae are composed primarily of collagen intermixed with GAGs. The dense collagen core is consistent with previous findings[51,52,234]; however, an outer, more loose layer of collagen was less evident in our histological sections than that reported by Ritchie et al. (2005)[52]. A layer of elastin fibers intermixed with collagen was present beneath the outer endothelial cell layer; the elastin fibers diminished in size and abundance towards the tissue core as other studies confirm[51,52,234]. This combination of collagen for tensile

strength and elastin for an energetically favorable restoration of collagen crimp is well-suited to the cyclic loading environment to which chordae are subjected.

Chordae bifurcation histology was unlike that observed in straight segments, suggesting it is functionally distinct from the surrounding microenvironment. Total cell density was 4-fold higher than straight segments, an observation in both heifers and pregnant animals. These cells were more circular in appearance unlike the VICs found in the tissue bulk, whose shape followed the waves of collagen crimp. Their circular morphology was likely attributable to the decline in collagen organization and/or content at bifurcations, as the cells were no longer physically constrained between fibers. Alternatively, these cells may have been simply caught in cross-section during histological processing, given the possibility that collagen fibers at bifurcations could be projecting out of the longitudinal plane (discussed above). The shear density of cells present compared to straight regions hints at a greater remodelling capacity for bifurcations. This is supported by the high GAG content, as GAGs have been implicated in a wide variety of collagen-specific ECM regulatory roles. One proteoglycan in particular – decorin – is a small leucine-rich proteoglycan abundant in chordae[56] that can bind directly to collagen type I and regulate collagen fibrillogenesis, assembly, interfibrillar spacing, fibril growth, and orientation[191-194,235]. Unfortunately, the Movat stain itself does not differentiate between types of proteoglycans and therefore specific proteoglycans cannot be directly associated with the bifurcation; however, this general abundance of GAGs could communicate directly with the dense cell population to facilitate and orchestrate ECM remodelling at bifurcations.

This notion of preferential ECM remodelling at bifurcations due to an increased cell density and GAG concentration, is strongly reinforced by the astounding invasion of peripheral elastin into chordae bifurcations. Elastin, as described above, has only ever been found in abundance longitudinally encircling the outer chordal layer. This body of work has concretely shown a multitude of bifurcations containing a range of elastin propagations depths. This is strong evidence to support the chordae splitting hypothesis as an explanation for the increase in chordae number seen during pregnancy. Importantly, such elastin fibers were observed in bifurcations from both heifers and pregnant cows. In combination with the similarities thus far observed between pregnancy groups, this

chordae splitting concept must reasonably be extended to include chordae from non-pregnant animals. The high frequency (>1Hz) cyclic loading environment endured by hearts valves, accommodating valve closure approximately 70 times/min and over 35 million times per year, would inevitably lead to an accumulation of fatigue damage to the chordal ECM. This problem is addressed through baseline levels of ECM synthesis and degradation provided by resident VICs, providing heart valves with their structural and functionally longevity[8,17,18]. This type of routine tissue turnover is known at the cellular level, but could a similar process be occurring at the macro scale, including the turnover and renewal of entire chordae branches? Elastin penetration into chordae bifurcations hints yes.

With the evidence in hand thus far, we can begin to develop a preliminary model describing chordae splitting. In non-pregnant animals, an accumulation of fatigue damage (similar to other collagenous tissues) could be the initial trigger for chordae splitting, stimulating a repair-oriented remodelling response. In addition to tendon microdamage, an upregulation of chordal splitting in pregnant cows could be uniquely triggered by: (i) heightened mechanical loading of the chordal apparatus, (ii) hormones, (iii) the invasion of fetal cells into maternal valve tissue (a phenomenon known as fetal microchimerism[236]), or a combination of (i)-(iii). Regardless of the stimulus, qVICs will activate and initiate the bifurcation remodelling process. This includes an increase in GAG synthesis at the bifurcation tip where collagen degradation begins, and a *de novo* synthesis of elastic fibers as an extension to those currently present strictly around the chordal periphery. This statement of elastin synthesis in a mature adult tissue is, in and of itself, a controversial one. Elastin deposition and remodelling is believed only to occur during gestation and the perinatal period as tissues develop, with minimal (if any) elastin turnover in healthy adult tissues[237-241]. However, recent studies of the maternal aorta suggest that a reactivation of elastin synthesis and mature elastic remodelling is indeed possible[242,243]. Elastic fibers will begin invading the bifurcation tissue (Figure 4.24 'B'), being continually synthesized and propagated down the cleavage plane from either side of the bifurcation until they join at a point, effectively bounding and isolating a mass of tissue (Figure 4.24 'C'). The excluded tissue area will then degrade, and be eventually lost altogether. The elastin, which once penetrated into the tissue bulk, will become the

new exterior elastin wall well-known to typical chordae structure. This process can then repeat itself, progressing longitudinally down the length of the chordae. It's unlikely that these propagations proceed down to the papillary muscles, as there are relatively few chordae-papillary muscle insertions compared to total chordae number in the valve. To elevate chordae numbers, this process must therefore initiate at the leaflet insertion site. The initial cleavage event creating two distinct attachments may proceed similar to the gap formations observed in the primordial leaflet tissue; this bifurcation can then proceed down the length of the chordae as described above. The histological approaches used herein did not yield any definitive signs of an initial cleavage event at the leaflet surface. Additional staining of specific ECM remodelling proteins, such as a series of MMPs, would need to be applied to identify these initial splitting zones.

If this process is occurring in both heifers and pregnant cows, why is there an increase in chordae number during pregnancy, while the number of chordae in adult heifers presumably remains static? If new chordae are formed, then, necessarily, old chordae must be resorbed to maintain a constant number of chordal attachments. It's possible that chordae splitting is somehow amplified with the unique hemodynamic burden, hormonal aspects, and/or fetal cell trafficking associated with pregnancy, and splitting simply overwhelms the ongoing resorption process. The semi-quantitative comparison of elastin morphologies at bifurcations showed no difference in their frequencies between heifers and pregnant cows, suggesting this process is occurring throughout the valve in similar numbers of chordae in both groups. However, histology only provides a snapshot in time, which therefore does not exclude the possibility that chordae splitting could be occurring more rapidly in pregnancy. Alternatively, the resorption process may slow relative to splitting tissue turnover as more chordal attachments are functionally required to support the expanding leaflet tissue. In the 40+ valves obtained for this study, some abnormally long, thin chordae have been observed in numerous valves. The length of these chordae far exceeded that of their neighbouring attachments and certainly would not have borne mechanical load *in vivo*. These chordae, which were non-functional mechanically, may have been undergoing resorption. Odd tissue lumps were also observed near bifurcations in some histological sections that could signify ongoing residual tissue resorption (Figure 5.1).

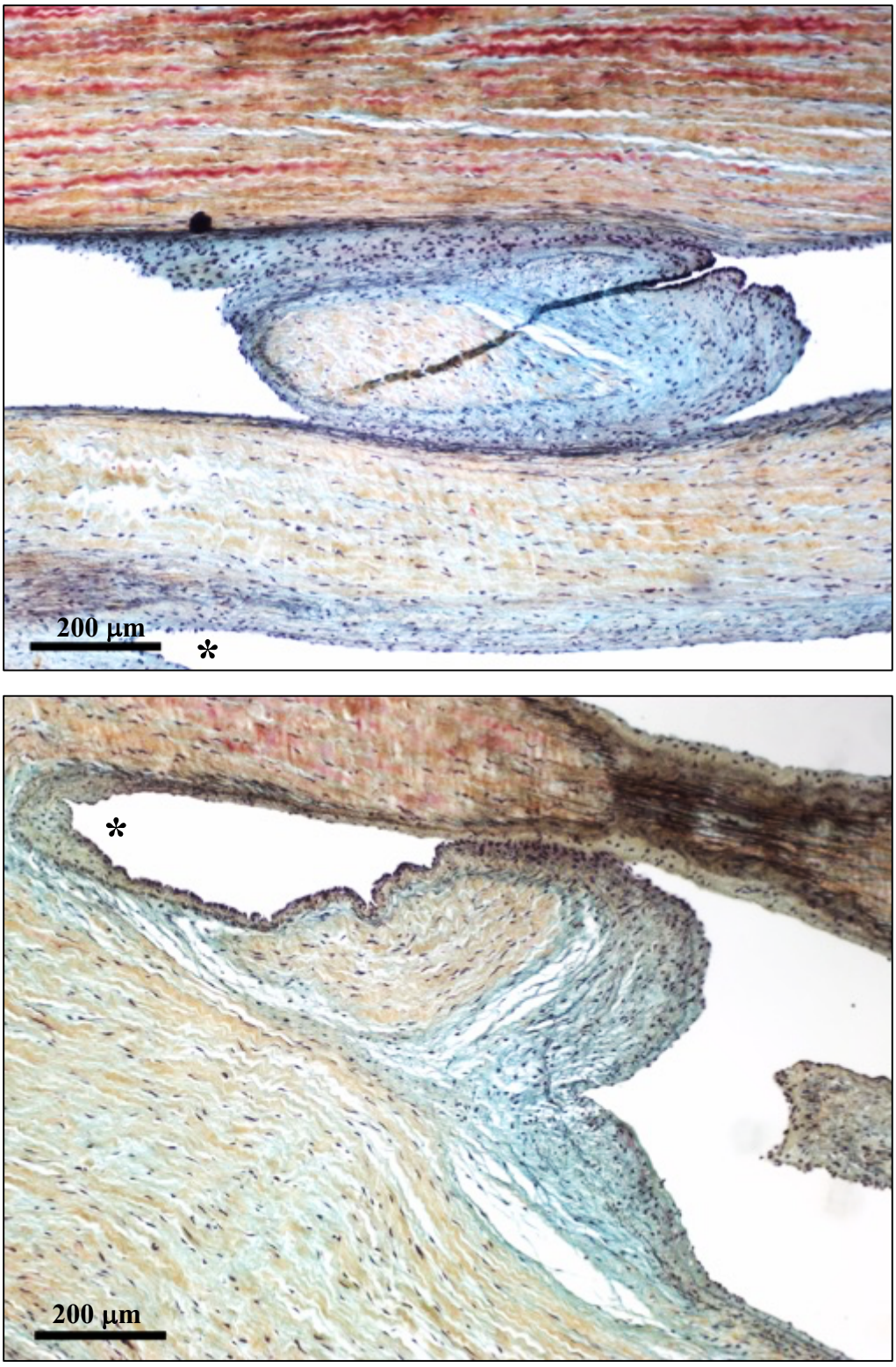

Figure 5.1: Movat Pentachrome-stained longitudinal sections through maternal bovine mitral chordae bifurcations showing the presence of odd tissue lumps. These regions may be undergoing resorption. Yellow=collagen, blue/green=GAGs, black lines= elastin fibers, purple dots=cell nuclei. Bifurcations are marked with an asterix (*).

5.5 α-SMA

Although VIC density speaks to the remodelling potential at chordae bifurcations, their phenotypic expression is a better marker for their level of cellular activity. Activated VICs are unique from qVICs in that they express α-SMA. Quiescent VICs can become activated when they sense a shift in their mechanical environment, to which they respond and remodel the surrounding ECM. There have been ample studies to show that VIC activation goes hand in hand with actively remodelling valves, such as fetal and diseased valves. A study performed by Rabkin-Aikawa et al. (2004) compared VIC population and proteolytic enzyme secretion in ovine and human pulmonary valves during fetal development and adulthood[101]. Their experiments showed that the qVIC population dominates in mature pulmonary valves (~90%), whereas fetal valves consist primarily of aVICs (62%) – indicative of the necessary ECM remodelling required for heart valve development. This staggering increase in aVICs was accompanied by an ~80% increase in MMP-13 expression in human fetal valves[101]. Compared to adults, fetal pulmonary and aortic valves not only show an aVIC phenotype and abundant MMP-collagenase expression, but also have a higher VIC density and proliferation to apoptosis ratio[195]. Differences between neonatal aortic and pulmonary valves were also observed, with a higher presence of aVICs in aortic valves only after the abrupt circulatory change (and thus elevated mechanical loading) associated with birth[195]. Similar phenotypes and protein expression patterns are observed in myxomatous mitral valve leaflets and chordae, which are characterized by a pathological thickening of the spongiosa via excess proteoglycan deposition, a reduction in collagen content and alignment, and elastin fragmentation[128,132,133,244]. These changes are mediated via the accumulation of aVICs and by an approximate 3-fold increase in MMP-1 and MMP-13 expression[101,133], the effects of which are often more severe in chordae[53,134].

The expectation herein, was to observe a global increase (at chordae straight segments and bifurcations) in VIC activation in pregnancy compared to heifers, stimulated by maternal hemodynamics and cardiac expansion. Moreover, although the number of chordae increase during gestation, their leaflet insertion density decreases which could further exacerbate their mechanical loading[166] and activate an increasing

number of VICs; however, this was in contrast to our findings which showed the number of α-SMA+ cells/0.01mm^2 and the % α-SMA+ cells/0.01mm^2 were unchanged between pregnancy groups. Remarkably, despite the drastic leaflet remodelling shown to take place during pregnancy to which the same α-SMA immunostain was applied, there was similarly no significant increase in the number of α-SMA+ cells/0.01mm^2 nor in the % α-SMA+ cells/0.01mm^2 in the leaflet tissue[196]. Instead, there was actually a *decrease* in overall VIC density in pregnancy, as well as a *decrease* in aVIC content. This was likely a consequence of the significant increase in leaflet area, overwhelming any potential proliferative cellular action. In the study by Pierlot et al. (2015), mean non-pregnant mitral leaflet VIC density was 10.2 cells/0.01mm^2. Mean non-pregnant straight segment and bifurcation VIC densities in this study were 3.9 cells/0.01mm^2 vs 14.4 cells/0.01mm^2 respectively, showing that leaflet tissue is intermediately cellular relative to these chordae locations. Pierlot et al. (2015) also reported a surprisingly high 43% α-SMA+ cells/0.01mm^2 in the bovine mitral valve anterior leaflet; while only 2-5% of the cell population in healthy human adult heart valves is comprised of aVICs[100,101]. The current work's proportions in bovine chordae are more consistent with those published for human valves with 4.2% (straight segments) and 7.0% (bifurcations) of VICs being α-SMA+ in heifers.

To the author's knowledge, no quantitative data has been published regarding chordal α-SMA expression in diseased or healthy valves of any kind. Regrettably, this leaves only a possible comparison between aVICs in leaflets and chordae as detailed above. Although limited, there are studies that describe cell activation in chordae *qualitatively*, that can, at the very least, validate their ability to remodel *in vivo* and explain how chordae composition and structure are altered in disease. One study employing transmission electron microscopy of degenerative mitral valve disease revealed chordae interstitial cells containing relatively robust rough endoplasmic reticula[127]. Myofibroblasts (similar to aVICs), are known to contain hypertrophic rough endoplasmic reticula as their synthetic processes are upregulated[245]. The majority of interstitial cells observed in degenerative mitral valve chordae were shown to contain this organelle-specific feature of activated matrix remodelling cells. Another study by Dal-Bianco et al. (2009) showed that tethered mitral valve leaflets (and thus increased

mechanical loading on valve chords), lead to a sub-endothelial accumulation of aVICs – a sign of a reactivated embryonic developmental pathway known as endothelial-mesenchymal transdifferentiation (EMT)[122]. In this process, endothelial cells delaminate from the tissue surface and migrate deeper into the tissue, gaining properties of mesenchymal cell markers like α-SMA[100]. This mechanism is imperative to the developmental remodelling progress. Interestingly, sub-endothelial staining of α-SMA was also observed occasionally in the current study (Figure 5.2). This observation was made in hindsight, and therefore its frequency was not compared between heifers and pregnant cows. This measurement, along with another co-immunostain for α-SMA and CD31 (marker for endothelial cells), would be a valuable future endeavour to uncover if an EMT-like process is underway in remodelling chordae.

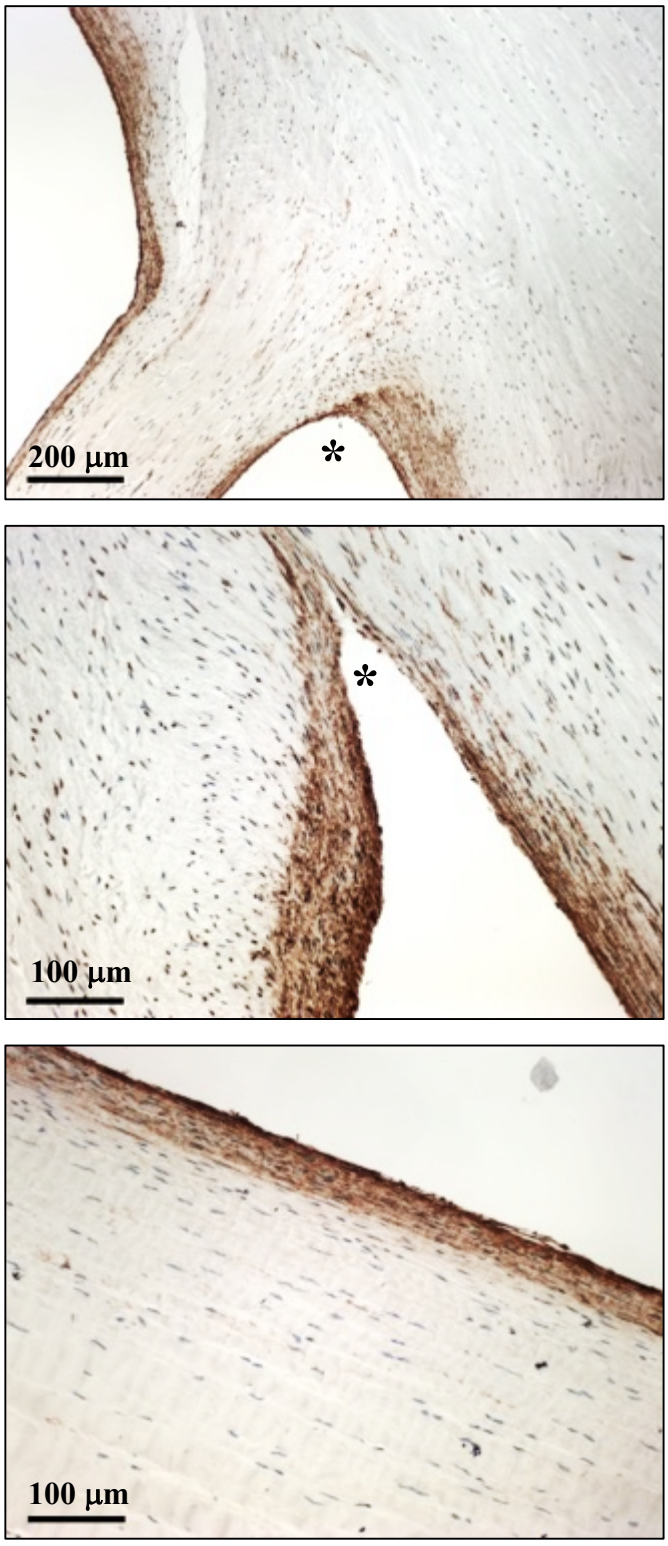

Figure 5.2: α-SMA immunostained longitudinal sections of bovine chordae tendineae taken from pregnant cows. A sub-endothelial accumulation of α-SMA+ staining (brown DAB deposition) is evident, possibly indicative of an endothelial-mesenchymal transdifferentiation. Bifurcations are marked with an asterix (*).

Even though no significant differences in α-SMA expression were observed between pregnancy groups, the number of α-SMA+ cells/0.01mm^2 tended to be higher (p<0.095) at bifurcations relative to straight segments. In all but one valve of the 6 valves studied (3 heifer, 3 pregnant), the means for the number of α-SMA+ cells/0.01mm^2 and % α-SMA+ cells/0.01mm^2 were consistently, and substantially larger at bifurcations compared to straight segments. However, there was no statistical significance achieved, likely due to the high standard deviations in these measurements. This shows that there was a large variation in α-SMA expression amongst bifurcations and straight segments within a single valve. This indicates, for example, that some bifurcations contain abundant aVICs remodelling the tissue, while other chordae bifurcations within the same valve are relatively stagnant. This could suggest the remodelling process is more selective in nature rather than global, targeting specific chordae for matrix turnover as the valve apparatus requires based on shifts in the mechanical environment, the accumulation of molecular damage, etc. Occasionally, tissue perforations were present below bifurcations surrounded by dense clusters of aVICs. These regions also lacked birefringence, showing strong evidence for local collagen remodelling and tissue degradation. This finding is akin to chordae development inside the chick embryo, where the tissue sheet linking the primordial valve cusps to the papillary muscle develops a series of perforations to create isolated chordae tendineae[222]. Endocardial cells are present nearby these embryonic perforations, suggesting a programmed cellular event. The tissue perforations observed inside mature bovine chordae could be a recapitulation of this developmental mechanism, and represent the advancement of the cleavage plane longitudinally down the chordal axis as splitting propagates. The association between VIC activation and the presence of elastin at bifurcations was not investigated; however, this would certainly be valuable future data to corroborate the idea that elastin propagation at bifurcations into the common trunk segment signifies an actively remodelling structure.

5.6 Periostin

The final remodelling marker searched for in this work was periostin, a matricellular protein that mediates a wide variety of cell-matrix interactions. Originally discovered in the periosteum and periodontal ligament, it has since been implicated in ECM remodelling in tissues throughout the body – including the heart. Indeed, periostin expression is present throughout the primordial mitral valve leaflets, and ubiquitously expressed in the chordae tendineae during cardiac development[246,247]; periostin has been deemed essential in the successful maturation of developing valve tissue[201,248]. More specifically and importantly for this work, periostin is required for the process of healthy chordae branching throughout fetal development[201]. Periostin null mice exhibit profound structural defects in the tensile apparatus. The chordae are stunted and thickened, and exhibit deficient branching patterns relative to wild-type mice[201]. This makes sense, given periostin's ability to mediate collagen type I fibrillogenesis – one of the main collagens found in the chordae tendineae[202]. The re-initiation of chordae splitting in a mature adult valve as seen in pregnancy, could partially be the result of an elevation in baseline periostin expression. An upregulation of this protein in maternal chordae would be strong evidence to support an actively remodelling chordae branching network.

Histological experiments revealed periostin to be abundant in chordae taken from both heifers and pregnant cows. This is comparable with previous reports that show intense periostin expression in adult mitral leaflets and chordae[198,201], consistent with that observed in fetal development. More interestingly was the spatial localization of periostin expression; the intensity of periostin staining was increased at bifurcations and around the chordal periphery. In the majority of cases, the intense periostin staining coincided with the presence of typical sub-endothelial elastin, as well as with the unique elastin propagations visible at bifurcations. Although abundant for periostin-collagen relationships, the literature is scarce citing the co-localization of periostin with elastin fibers. In one study of healthy adult human aortic and mitral valves, periostin was expressed in both superficial layers beneath the endothelial cells, and was found to largely overlap with elastin expression[198]. Their work also suggested that periostin contributes to valve degeneration in disease by inducing MMP production. The increase

in periostin expression seen at chordae bifurcations could therefore be contributing to chordae splitting in two ways by: (1) guiding local collagen remodelling at the head of the proceeding split, and (2) increasing MMP production at the tail to degrade leftover, scrap tissue remaining from the split. These contributions, combined with a trend towards elevated aVICs at bifurcations, tie in well with the preliminary model of routine chordae splitting, which is central to this thesis.

5.7 Summary of Mitral Valve Chordae Remodelling in the Maternal Bovine Heart

The overarching objective of this thesis work was to determine the mechanisms by which maternal bovine chordae tendineae remodel, giving rise to the increase in chordae number observed in pregnancy. A summary of the results from chordae counting, thermal, and histological experiments – as they relate to the outlined hypotheses – is provided below.

5.7.1 Chordae Counting

Hypothesis: The number of basal and marginal chordae will increase in maternal valves as the gestational period progresses.

Conclusion: There was a significant increase in basal and marginal chordae number in pregnancy; however, there was no relationship with gestational age. This effect was likely masked due to the high valve-to-valve variation in total chordae number from animals of the same age.

5.7.2 DSC

Hypothesis: There will be a global decrease in collagen thermal stability, and the distribution of thermal stabilities will increase in maternal chordae.

Conclusion: Thermal stability was largely unchanged in maternal chordae compared to heifers, marked by comparable values of T_{onset}, T_{peak}, and specific enthalpy; the FWHM was lower in pregnancy. The lack of prominent thermal changes between pregnancy groups suggest that the maternal increase in chordae number does not require substantial collagen remodelling throughout the tissue bulk (relative to heifers) to occur. Collagen remodelling is instead, localized to the "fault line" where chordal splitting is believed to unfold. During this investigation, significant thermal differences were observed between chordae types, likely reflecting their unique *in vivo* loading regimes, cross-link profiles, or tissue hydration.

5.7.3 Collagen Crimp

Hypothesis: Maternal chordae crimp length will increase and percent crimp area will decrease relative to non-pregnant animals. There will be a strong presence of localized, disordered collagen at chordae bifurcations and leaflet insertion sites from pregnant cows.

Conclusion: There were no significant changes in collagen crimp wavelength or percent area occupied by crimp between heifers and pregnant cows. This was surprising given the magnitude of structural change observed previously in the leaflet[166,186,187]. A novel relationship between crimp wavelength and distance from the anterior leaflet was discovered in strut and basal chordae, which could prove advantageous biomechanically. Uniform crimp patterns were disturbed at bifurcations and at leaflet insertion sites in both pregnancy groups, likely as a consequence of their mechanical loading environment or, more specifically at bifurcations, as a sign of ECM remodelling.

5.7.4 Movat Pentachrome

Hypothesis: Chordae bifurcations in pregnant animals will show an increase in cell nuclei and GAGs. Elastin will be localized to the outer chordal layer in both pregnant and non-pregnant animals, with minimal fibers present within the tissue bulk.

Conclusion: Straight segment bovine chordae composition (non-pregnant and pregnant) was consistent with previous findings in humans and pigs, with abundant sub-endothelial elastic fibers and increasingly few towards the tissue core. Never-before published chordae bifurcation histology was shown to be unique from the surrounding tissue, containing increased cell density and GAG content. Select bifurcations also contained deep, longitudinal propagations of elastin into the common trunk segment – strong evidence for chordae splitting observed in both non-pregnant and pregnant animals. A preliminary model of chordae splitting was developed from the histological evidence.

5.7.5 α-SMA

Hypothesis: Chordae immunostained from pregnant cows will show a global (straight segments and bifurcations) increase in the density and percentage of aVICs compared to heifers; aVICs will be most abundant at maternal bifurcations.

Conclusion: VIC activation was independent of pregnancy state. The number of α-SMA+ cells/0.01mm^2 tended to be higher at bifurcations relative to straight segments. Combined with visible tissue perforations and a loss of birefringence below bifurcations, these data collectively suggest that select bifurcations are being actively remodelled in heifers and pregnant cows.

5.7.6 Periostin

Hypothesis: Periostin expression will be upregulated in pregnancy adjacent to maternal bifurcations where chordae splitting is believed to be occurring; heifers will show a more homogeneous periostin expression.

Conclusion: Qualitatively, periostin expression was similar in chordae taken from non-pregnant and pregnant animals. Intense periostin staining was observed at select bifurcations and frequently around the chordal periphery, loosely co-localizing with

elastic fibers. These observations support our hypothesis that bifurcations – from both heifer and pregnant animals – are regions of active, cellular ECM remodelling.

Chapter 6 – Conclusion

6.1 Future Research Directions

The current investigation has not only revealed a wealth of new information regarding normal chordae physiology, composition, and structure, but has also suggested a remarkable remodelling potential in the hearts of non-pregnant and pregnant animals. Despite the novel contributions of this thesis, the mechanisms specific to pregnancy that yield an increase in chordal attachments during gestation remain a mystery. Ergo, more research is required to elucidate these mechanisms, and to advance the presented preliminary concept of routine chordae splitting and tissue turnover.

6.1.1 Post-Partum Chordae Counting & Other Experimental Follow-Ups

One of the most frequently posed questions with respect to maternal cardiovascular remodelling is whether the dramatic physiological changes that occur, return to normal post-partum. The multitude of hemodynamic changes including cardiac output, blood pressure, vascular resistance, blood volume, heart rate, and stroke volume return to baseline post-delivery[146,249-251]. Even the structural changes such as the increase in left ventricular mass and annular orifice area reportedly decrease to pre-pregnant levels[117,146,167,252]. If the hemodynamic stress and mitral orifice expansion are the initial triggers for maternal leaflet and chordae remodelling, will their postpartum abatement lead to the concomitant reversal of leaflet area and chordae number? More than that, will the valve's composition, mechanical properties, collagen crimp structure, and chordae lengthening return to pre-pregnant values? Although hemodynamics and select structural adaptations are known to reverse, some changes with pregnancy may be more permanent such as the accumulation of elastin within the aortic wall[243]. Ideally, valves taken from previously pregnant cows need to be harvested at different time points post-partum with all the aforementioned experiments performed, to see if leaflet and chordal remodelling is reversed in the months following delivery. Unfortunately, the necessary monitoring of

cattle reproduction makes this approach extremely difficult. The most practical means by which to address such questions would rather be in a small, in-house animal model such as mice. However, before any post-partum changes could be addressed, the maternal physiological remodelling observed in cattle (increase in leaflet area, chordae number, etc.) would have to be observed and validated in the mouse model.

6.1.2 Tricuspid Valve Chordae Counting

All the work herein has been restricted to the chordae of the bovine mitral valve anterior leaflet only. As discussed, there is minimal clinically significant retrograde flow through the mitral valve observed in pregnancy compared to healthy controls, but a 25% increase in tricuspid regurgitation, despite being on the left, lower pressure side of the heart[253]. Whether the number of tricuspid valve chordae increase is unknown, and could possibly explain clinically relevant differences in valve function. Following the same protocol outlined for chordae counting in this work, future studies could examine whether the tricuspid valve experiences similar increases in chordae number during gestation, or whether this growth is unique to the mitral apparatus.

6.1.3 Proteinase Expression

To help substantiate the chordae splitting hypothesis, immunostaining for MMPs and their tissue inhibitors would be valuable. Their localization and quantity would help confirm areas of active ECM remodelling, such as bifurcations containing elastin propagations or sites of cleavage initiation at the leaflet surface. Despite both heifers and pregnant cows containing the same density of aVICs, an upregulation of such proteinases could give information as to the rate of tissue turnover – something that may distinguish these experimental groups.

6.1.4 Cross-link Profile

Collagen cross-links can greatly influence molecular thermal stability. The DSC data presented here, for evaluations between pregnancy state and chordae type, would greatly benefit from knowing the relative quantities and brand of cross-links present within the tissue. Obtaining ratios for immature to mature cross-links (undetected by DSC) through high performance liquid chromatography or other biochemical techniques could be an indicator for the remodelling state of the tissue.

6.1.5 Hormones - Relaxin

Until this point, an increase in mechanical stress due to hemodynamic and structural cardiac modifications has largely been discussed as the trigger for heart valve remodelling. It would be naïve to think however, that mechanical stress alone would be influencing such a response given the breadth of additional hormones secreted during pregnancy that are known to contribute to global physiological remodelling during gestation. Rather, mechanical cues and hormones likely act synergistically to elicit pregnancy-induced heart valve remodelling, such as the increase in mitral valve chordae number. One hormone in particular – relaxin – has been implicated in a wide variety of collagen-specific remodelling events that are required for the establishment of pregnancy and for the preparation of successful parturition. Relaxin is secreted by the corpus luteum during the early stages of pregnancy, and is later taken over by more local endometrial and placental secretion[254]. It has been shown to influence collagen density and organization in the pubic symphysis, nipples, and cervix, favouring an overall softer, more compliant set of tissues (by increasing collagen catabolism) for the facilitation of child birth and breast-feeding[255-258]. Contrastingly, relaxin also reduces collagen degradation in the endometrium by negatively regulating MMP production[259].

The presence of relaxin receptors within the mitral valve leaflets and chordae is currently unknown; however, it seems plausible given other studies on the myocardium and aortic valve. Hsu et al. (2002)[260] showed that ventricular and atrial cells contain receptors for relaxin, while Dschietzig et al. (2001)[261] demonstrated relaxin synthesis in

myocytes and interstitial cells within the myocardium. Recently, relaxin itself has also been shown to be present in aortic valve tissue[262]. With these characteristics of relaxin in mind, it would be valuable to elucidate the hormonal roles at play in maternal valve remodelling in future studies. For example, using a mouse model, relaxin could be administrated to non-pregnant mice to look for signs of valve remodelling.

6.1.6 Fetal Chordae Research

Much like chordae remodelling in pregnancy, very little is known about fetal chordae development. Seeing as how the only other documented increase in chordae number is during fetal development, a thorough understanding of fetal mechanisms would likely be translatable to pregnancy. The study of these two models in tandem could yield shared results, with the possibility of pregnancy being a recapitulation of fetal chordae development.

6.2 Concluding Remarks

This research has furthered our understanding of fundamental mitral chordae physiology, composition, and structure in both pregnant and non-pregnant animals. The chordae are clearly unique, and do not simply mimic the remodelling patterns observed in the mitral anterior leaflet during pregnancy. The mechanisms responsible for the increase in maternal chordae number remain a mystery, but much has been accomplished towards its understanding. The ground laying work performed herein is a pivotal stepping stone towards achieving this goal, which, when fully unveiled, will certainly have future clinical significance.

The cardiac remodelling that occurs in pregnancy is well tolerated, i.e., the structural adaptations that occur meet the functional requirements of the mitral valve as the hemodynamics change. Contrastingly in disease, runaway valvular and myocardial remodelling processes ensue, eventually leading to the surgical replacement of native valves with bioprosthetic or synthetic constructs, or, in the long term, to complete heart failure and death. Maternal heart valve research is crucial to understanding the

differences between these distinct remodelling patterns and has implications for the future of cardiac regenerative medicine. Drugs and therapies could be developed to modulate VIC phenotypes and counteract pathological remodelling, switching the disease course into one of healthy adaptation. In the same respect, such information could prove valuable for tissue engineering as progress is made to direct the development of heart valve tissues *in vitro*. Long-term maternal health outcomes themselves could also improve. Risk factors for vascular disease are augmented during, and persist after pregnancy, with the severity increasing with multiple pregnancies[263]. A complete understanding of maternal heart valve physiology will undoubtedly contribute to improved future prognoses.

BIBLIOGRAPHY

1. Pappano, A. J. & Wier, W. G. *Cardiovascular Physiology*. 1–292 (Elsevier Inc, 2012).

2. Katz, A. M. *Physiology of the Heart*. (Lippincott Williams & Wilkins, 2010).

3. Harfield, D. How It Works. *www.howitworksdaily.com* (2012). Available at: http://www.howitworksdaily.com/inside-the-human-heart/. (Accessed: 27 June 2016)

4. Fukuta, H. & Little, W. C. The cardiac cycle and the physiologic basis of left ventricular contraction, ejection, relaxation, and filling. *Heart Fail Clin* **4,** 1–11 (2008).

5. Misfeld, M. & Sievers, H. H. Heart valve macro- and microstructure. *Philos Trans R Soc Lond B Biol Sci* **362,** 1421–1436 (2007).

6. Stella, J. A. & Sacks, M. S. On the biaxial mechanical properties of the layers of the aortic valve leaflet. *J Biomech Eng* **129,** 757–766 (2007).

7. El-Hamamsy, I., Chester, A. H. & Yacoub, M. H. Cellular regulation of the structure and function of aortic valves. *Journal of Advanced Research* (2010). doi:10.1016/j.jare.2010.02.007

8. Wiltz, D., Arevalos, A.C., Balaoing, L. R., Blancas, A. A., Sapp, M.C., Zhang, X., & Grande-Allen, J. K. Extracellular matrix organization, structure, and function, Chapter 1. *Calcific Aortic Valve Disease* (2013). doi:10.5772/52842

9. Scott, M. & Vesely, I. Aortic valve cusp microstructure: the role of elastin. *ATS* **60,** S391–4 (1995).

10. Rocca, D., Sartore, S., Guidolin, D., Bertiplaglia, B., Gerosa, G., Casarotto, D., Pauletto, P. Cell composition of the human pulmonary valve: a comparative study with the aortic valve--the VESALIO Project. Vitalitate Exornatum Succedaneum Aorticum labore Ingegnoso Obtinebitur. *Ann Thorac Surg* **70,** 1594–1600 (2000).

11. Sacks, M. S., David Merryman, W. & Schmidt, D. E. On the biomechanics of heart valve function. *J Biomech* **42,** 1804–1824 (2009).

12. Grande-Allen, K. J. & Liao, J. The Heterogeneous Biomechanics and Mechanobiology of the Mitral Valve: Implications for Tissue Engineering. *Curr Cardiol Rep* **13,** 113–120 (2011).

13. Rausch, M. K. *et al.* Characterization of Mitral Valve Annular Dynamics in the Beating Heart. *Ann Biomed Eng* **39,** 1690–1702 (2011).

14. Glasson, J. R., Komeda, M.K., Daughters, G. T., Niczyporuk, M. A., Bolger, A.F., Ingels, N. B., & Miller, D. C. Three-dimensional regional dynamics of the normal mitral anulus during left ventricular ejection. *J Thorac Cardiovasc Surg* **111,** 574–585 (1996).

15. Carlhall, C. Contribution of mitral annular excursion and shape dynamics to total left ventricular volume change. *Am J Physiol Heart Circ Physiol* **287,** H1836–H1841 (2004).

16. Tamburino, C. & Ussia, G.P. *Percutaneous Treatment of Left Side Cardiac Valves. A Practical Guide for the Interventional Cardiologist. 2nd Edition*. (Springer Science & Business Media, 2012).

17. Schneider, P. J. & Deck, J. D. Tissue and cell renewal in the natural aortic valve of rats: an autoradiographic study. *Cardiovascular Res* **15,** 181–189 (1981).

18. Dreger, S. A., Taylor, P. M., Allen, S. P. & Yacoub, M. H. Profile and localization of matrix metalloproteinases (MMPs) and their tissue inhibitors (TIMPs) in human heart valves. *J Heart Valve Dis* **11,** 875–80– discussion 880 (2002).

19. d'Arcy, J. L., Prendergast, B. D., Chambers, J. B., Ray, S. G. & Bridgewater, B. Valvular heart disease: the next cardiac epidemic. *Heart* **97,** 91–93 (2011).

20. Nkomo, V. T., Gardin, J.M., Skelton, T. N., Gottdiener, J. S., Scott, C. G., & Enriquez-Sarano, M. Burden of valvular heart diseases: a population-based study. *Lancet* **368,** 1005–1011 (2006).

21. Iung, B. & Vahanian, A. Nature Publishing Group 2011 Iung. *Nat Rev Cardiol* **8,** 162–172 (2011).

22. McCarthy, K. P., Ring, L. & Rana, B. S. Anatomy of the mitral valve: understanding the mitral valve complex in mitral regurgitation. *Eur J Echocardiogr* **11,** i3–i9 (2010).

23. Chiechi, M. A., Lees, W. M. & Thompson, R. Functional anatomy of the normal mitral valve. *J Thorac Surg* **32,** 378–398 (1956).

24. Kim, D.-H. *et al.* In vivo measurement of mitral leaflet surface area and subvalvular geometry in patients with asymmetrical septal hypertrophy: insights into the mechanism of outflow tract obstruction. *Circulation* **122,** 1298–1307 (2010).

25. Mautner, S. L., Klues, H. G., Mautner, G. C., Proschan, M. A., Roberts, W. C., & Maron, B. J. Comparison of mitral valve dimensions in adults with valvular aortic stenosis, pure aortic regurgitation and hypertrophic cardiomyopathy. *Am J Cardiol* **71,** 949–953 (1993).

26. Klues, H. G., Maron, B. J., Dollar, A. L. & Roberts, W. C. Diversity of structural mitral valve alterations in hypertrophic cardiomyopathy. *Circulation* **85,** 1651–1660 (1992).

27. Muraru, D. *et al.* Mitral valve anatomy and function: new insights from three-dimensional echocardiography. *J Cardiovasc Med (Hagerstown)* **14,** 91–99 (2013).

28. Tamburino, C. & Ussia, G. P. *Percutaneous Treatment of Left Side Cardiac Valves: A Practical Guide for the Interventional Cardiologist*. 1–333 (2012).

29. Muresian, H. The clinical anatomy of the mitral valve. *Clin Anat* **22,** 85–98 (2009).

30. Gogoladze, G., Dellis, S. L., Donnino, R., Ribakove, G., Greenhouse, D. G., Galloway, A., & Grossi, E. Analysis of the mitral coaptation zone in normal and functional regurgitant valves. *Ann Thorac Surg* **89,** 1158–1161 (2010).

31. Carpentier, A., Adams, D. H. & Filsoufi, F. *Carpentier's Reconstructive Valve Surgery*. (Elsevier Health Sciences, 2010).

32. Gross, L. & Kugel, M. A. Topographic Anatomy and Histology of the Valves in the Human Heart. *Am J Pathol* **7,** 445–474.7 (1931).

33. Simionescu, D. T., Lovekamp, J. J. & Vyavahare, N. R. Degeneration of bioprosthetic heart valve cusp and wall tissues is initiated during tissue preparation: an ultrastructural study. *J Heart Valve Dis* **12,** 226–234 (2003).

34. Yanagishita, M. Function of proteoglycans in the extracellular matrix. *Acta Pathol Jpn* **43,** 283–293 (1993).

35. Esko, J.D., Kimata, K, & Lindahl, U. Proteoglycans and Sulfated Glycosaminoglycans, Chapter 16. *Essentials of Glycobiology. 2nd Edition.* Cold Spring Harbor (NY): Cold Spring Harbor Laboratory Press, 2009).

36. Dal-Bianco, J. P. & Levine, R. A. Anatomy of the mitral valve apparatus: role of 2D and 3D echocardiography. *Cardiol Clin* **31,** 151–164 (2013).

37. Hulmes, D. *Collagen: Structure and Mechanics.* Collagen diversity, synthesis and assembly, Chapter 2 (Springer, 2008).

38. Shoulders, M. D. & Raines, R. T. Collagen structure and stability. *Annu Rev Biochem* **78,** 929–958 (2009).

39. Ramshaw, J. A., Shah, N. K. & Brodsky, B. Gly-X-Y tripeptide frequencies in collagen: a context for host-guest triple-helical peptides. *J Struct Biol* **122,** 86–91 (1998).

40. Fratzl, P. *Collagen: Structure and Mechanics*. Collagen: Structure and Mechanics, an Introduction, Chapter 1. (Springer, 2008).

41. Avery, N. C. & Bailey, A. J. *Collagen: Structure and Mechanics.* Restraining cross-links responsible for the mechanical properties of collagen fibers: natural and artificial, Chapter 4. (Springer, 2008).

42. Robins, S. P., Shimokomaki, M. & Bailey, A. J. The chemistry of the collagen cross-links. Age-related changes in the reducible components of intact bovine collagen fibres. *Biochem J* **131,** 771–780 (1973).

43. Cannon, D. J. & Davison, P. F. Aging, and crosslinking in mammlian collagen. *Exp Aging Res* **3,** 87–105 (1977).

44. Avery, N. C. & Bailey, A. J. Enzymic and non-enzymic cross-linking mechanisms in relation to turnover of collagen: relevance to aging and exercise. *Scand J Med Sci Sports* **15,** 231–240 (2005).

45. Aldous, I. G., Veres, S. P., Jahangir, A. & Lee, J. M. Differences in collagen cross-linking between the four valves of the bovine heart: a possible role in adaptation to mechanical fatigue. *Am J Physiol Heart Circ Physiol* **296,** H1898–906 (2009).

46. Miles, C. A. & Bailey, A. J. Thermal denaturation of collagen revisited. *Proc Indian Acad Sci* (*Chem Sci*) **111,** 71-80 (1999).

47. Miles, C. A. & Ghelashvili, M. Polymer-in-a-box mechanism for the thermal stabilization of collagen molecules in fibers. *Biophysj* **76,** 3243–3252 (1999).

48. Tiktopulo, E. I. & Kajava, A. V. Denaturation of type I collagen fibrils is an endothermic process accompanied by a noticeable change in the partial heat capacity. *Biochemistry* **37,** 8147–8152 (1998).

49. Aldous, I. G., Lee, J. M. & Wells, S. M. Differential changes in the molecular stability of collagen from the pulmonary and aortic valves during the fetal-to-neonatal transition. *Ann Biomed Eng* **38,** 3000–3009 (2010).

50. Lim, K. O. & Boughner, D. R. Mechanical properties of human mitral valve chordae tendineae: variation with size and strain rate. *Can J Physiol Pharmacol* **53,** 330–339 (1975).

51. Millington-Sanders, C., Meir, A., Lawrence, L. & Stolinski, C. Structure of chordae tendineae in the left ventricle of the human heart. *J Anatomy* **192 (Pt 4),** 573–581 (1998).

52. Ritchie, J., Warnock, J. N. & Yoganathan, A. P. Structural characterization of the chordae tendineae in native porcine mitral valves. *Ann Thorac Surg* **80,** 189–197 (2005).

53. Grande-Allen, K. J., Griffin, B. P., Ratliff, N. B., Cosgrove, D. M., III & Vesely, I. Glycosaminoglycan profiles of myxomatous mitral leaflets and chordae parallel the severity of mechanical alterations. *J Am Coll Cardiol* **42,** 271–277 (2003).

54. Liao, J. & Vesely, I. Relationship between collagen fibrils, glycosaminoglycans, and stress relaxation in mitral valve chordae tendineae. *Ann Biomed Eng* **32,** 977–983 (2004).

55. Akhtar, S., Meek, K. M. & James, V. Immunolocalization of elastin, collagen type I and type III, fibronectin, and vitronectin in extracellular matrix components of normal and myxomatous mitral heart valve chordae tendineae. *Cardiovasc Pathol* **8,** 203–211 (1999).

56. Grande-Allen, K. J., Calabro, A., Gupta, V., Wight, T. N., Hascall, V. C., & Vesely, I. Glycosaminoglycans and proteoglycans in normal mitral valve leaflets and chordae: association with regions of tensile and compressive loading. *Glycobiology* **14,** 621–633 (2004).

57. Lim, K. O. & Boughner, D. R. Morphology and relationship to extensibility curves of human mitral valve chordae tendineae. *Circ Res* **39,** 580–585 (1976).

58. Lim, K. O. & Boughner, D. R. Scanning electron microscopical study of human mitral valve chordae tendineae. *Arch Pathol Lab Med* **101,** 236–238 (1977).

59. Quain, J. *Quain's Anatomy: The Heart*. **V,** (Green & Co, 1929).

60. Tandler, J. *Anatomie des Herzens: Handbuch des Anatomie des Menshcen.* **3,** (Verlagsbuchandlung, 1913).

61. Brock, R. C. The surgical and pathological anatomy of the mitral valve. *Br Heart J* **14,** 489–513 (1952).

62. Lam, J. H., Ranganathan, N., Wigle, E. D. & Silver, M. D. Morphology of the human mitral valve. I. Chordae tendineae: a new classification. *Circulation* **41,** 449–458 (1970).

63. Rusted, I. E., Scheifley, C. H. & Edwards, J. E. Studies of the mitral valve. I. Anatomic features of the normal mitral valve and associated structures. *Circulation* **6,** 825–831 (1952).

64. Ranganathan, N., Lam, J. H.C., Wigle, E. D., & Silver, M.D. Morphology of the human mitral valve. II. The valve leaflets. *Circulation* **41,** 459–467 (1970).

65. Ho, S. Y. Anatomy of the mitral valve. *Heart* **88 Suppl 4,** iv5–10 (2002).

66. Silbiger, J. J. & Bazaz, R. Contemporary insights into the functional anatomy of the mitral valve. *Am Heart J* **158,** 887–895 (2009).

67. Rabbah, J.-P. M., Saikrishnan, N., Siefert, A. W., Santhanakrishnan, A. & Yoganathan, A. P. Mechanics of healthy and functionally diseased mitral valves: a critical review. *J Biomech Eng* **135,** 021007 (2013).

68. Gunnal, S. A., Wabale, R. N. & Farooqui, M. S. Morphological study of chordae tendinae in human cadaveric hearts. *Heart Views* **16,** 1–12 (2015).

69. Gunnal, S. A., Wabale, R. N. & Farooqui, M. S. Morphological variations of papillary muscles in the mitral valve complex in human cadaveric hearts. *Singapore Med J* **54,** 44–48 (2013).

70. Becker, A. E. & De Wit, A. P. Mitral valve apparatus. A spectrum of normality relevant to mitral valve prolapse. *Br Heart J* **42,** 680–689 (1979).

71. Kunzelman, K. S. & Cochran, R. P. Mechanical properties of basal and marginal mitral valve chordae tendineae. *ASAIO Trans* **36,** M405–8 (1990).

72. Liao, J. & Vesely, I. A structural basis for the size-related mechanical properties of mitral valve chordae tendineae. *J Biomech* **36,** 1125–1133 (2003).

73. Liao, J., Priddy, L. B., Wang, B., Chen, J. & Vesely, I. Ultrastructure of porcine mitral valve chordae tendineae. *J Heart Valve Dis* **18,** 292–299 (2009).

74. Obadia, J. F., Casali, C., Chassignolle, J.F., & Janier, M. Mitral subvalvular apparatus: different functions of primary and secondary chordae. *Circulation* **96,** 3124–3128 (1997).

75. He, S. *et al.* Geometric distribution of chordae tendineae: an important anatomic feature in mitral valve function. *J Heart Valve Dis* **9,** 495–501– discussion 502–3 (2000).

76. Lomholt, M., Nielsen, S. L., Hansen, S. B., Andersen, N. T. & Hasenkam, J. M. Differential tension between secondary and primary mitral chordae in an acute in-vivo porcine model. *J. Heart Valve Dis.* **11,** 337–345 (2002).

77. Debonnaire, P., Palmen, M., Marsan, N. A. & Delgado, V. Contemporary imaging of normal mitral valve anatomy and function. *Curr Opin Cardiol* **27,** 455–464 (2012).

78. Timek, T. A. *et al.* Influence of anterior mitral leaflet second-order chordae on leaflet dynamics and valve competence. *ATS* **72,** 535–40– discussion 541 (2001).

79. Nielsen, S. L. *et al.* Influence of anterior mitral leaflet second-order chordae tendineae on left ventricular systolic function. *Circulation* **108,** 486–491 (2003).

80. Rodriguez, F. *et al.* Importance of mitral valve second-order chordae for left ventricular geometry, wall thickening mechanics, and global systolic function. *Circulation* **110,** II–115–II–122 (2004).

81. Goetz, W. A., Lim, H. S., Lansac, E., Saber, H. A., Pekar, F., Weber, P. A., & Duran, C. M. Anterior mitral basal 'stay' chords are essential for left ventricular geometry and function. *J Heart Valve Dis* **14,** 195–202– discussion 202–3 (2005).

82. Messas, E. Chordal Cutting Does Not Adversely Affect Left Ventricle Contractile Function. *Circulation* **114,** I–524–I–528 (2006).

83. Mestres, C.-A. & Bernal, J. M. Mitral valve repair: the chordae tendineae. *J Tehran Heart Cent* **7,** 92–99 (2012).

84. Ormiston, J. A., Shah, P. M., Tei, C. & Wong, M. Size and motion of the mitral valve annulus in man. I. A two-dimensional echocardiographic method and findings in normal subjects. *Circulation* **64,** 113–120 (1981).

85. Padala, M., Sacks, M. S., Liou, S. W., Balachandran, K., He, Z., & Yoganathan, A. P. Mechanics of the mitral valve strut chordae insertion region. *J Biomech Eng* **132,** 081004 (2010).

86. Levine, R. A., Handschumacher, M. D., Sanfilippo, A.J., Hagege A. A., Harrigan, P., Marshall, J. E., & Weyman A. E. Three-dimensional echocardiographic reconstruction of the mitral valve, with implications for the diagnosis of mitral valve prolapse. *Circulation* **80,** 589–598 (1989).

87. Salgo, I. S. *et al.* Effect of Annular Shape on Leaflet Curvature in Reducing Mitral Leaflet Stress. *Circulation* **106,** 711–717 (2002).

88. Jimenez, J. H. *et al.* A saddle-shaped annulus reduces systolic strain on the central region of the mitral valve anterior leaflet. *J Thorac Cardiovasc Surg* **134,** 1562–1568 (2007).

89. Jimenez, J. H., Soerensen, D. D., He, Z., He, S. & Yoganathan, A. P. Effects of a saddle shaped annulus on mitral valve function and chordal force distribution: an in vitro study. *Annals of Biomedical Engineering* **31,** 1171–1181 (2003).

90. Kunzelman, K. S., Cochran, R. P., Murphree, S. S., Ring, W. S., Verrier, E. D., & Eberhart, R. C. Differential collagen distribution in the mitral valve and its influence on biomechanical behaviour. *J Heart Valve Dis* **2,** 236–244 (1993).

91. Stephens, E. H., Chu, C.-K. & Grande-Allen, K. J. Valve proteoglycan content and glycosaminoglycan fine structure are unique to microstructure, mechanical load and age: Relevance to an age-specific tissue-engineered heart valve. *Acta Biomaterialia* **4,** 1148–1160 (2008).

92. Jimenez, J. H., Soerensen, D. D., He, Z., Ritchie, J. & Yoganathan, A. P. Mitral valve function and chordal force distribution using a flexible annulus model: an in vitro study. *Ann Biomed Eng* **33,** 557–566 (2005).

93. He, Z. & Jowers, C. A Novel Method to Measure Mitral Valve Chordal Tension. *J Biomech Eng* **131,** 014501 (2009).

94. Nielsen, S. L., Hansen, S. B., Nielsen, K. O., Nygaard, H., Paulsen, P. K., & Hasenkam, J. M. Imbalanced chordal force distribution causes acute ischemic mitral regurgitation: Mechanistic insights from chordae tendineae force measurements in pigs. *J Thorac Cardiovasc Surg* **129,** 525–531 (2005).

95. Broom, N. D. Simultaneous morphological and stress-strain studies of the fibrous components in wet heart valve leaflet tissue. *Connect Tissue Res* **6,** 37–50 (1978).

96. Folkhard, W., Mosler, E., Geercken, W., Knörzer, E., Nemetschek-Gansler, H., Nemetschek, Th., & Koch, M. H. J. Quantitative analysis of the molecular sliding mechanisms in native tendon collagen — time-resolved dynamic studies using synchrotron radiation. *Int J Biol Macromol* **9,** 169–175 (1987).

97. Misof, K., Rapp, G., & Fratzl, P. A new molecular model for collagen elasticity based on synchrotron X-ray scattering evidence. *Biophys J* **72,** 1376–1381 (1997).

98. Rabkin-Aikawa, E., Mayer, J. E. & Schoen, F. J. Heart valve regeneration. *Adv Biochem Eng Biotechnol* **94,** 141–179 (2005).

99. Liu, A. C., Joag, V. R. & Gotlieb, A. I. The emerging role of valve interstitial cell phenotypes in regulating heart valve pathobiology. *Am J Pathol* **171,** 1407–1418 (2007).

100. Schoen, F. J. Evolving concepts of cardiac valve dynamics: the continuum of development, functional structure, pathobiology, and tissue engineering. *Circulation* **118,** 1864–1880 (2008).

101. Rabkin-Aikawa, E., Farber, M., Aikawa, M. & Schoen, F. J. Dynamic and reversible changes of interstitial cell phenotype during remodeling of cardiac valves. *J Heart Valve Dis* **13,** 841–847 (2004).

102. Taylor, P. M., Batten, P., Brand, N. J., Thomas, P. S. & Yacoub, M. H. The cardiac valve interstitial cell. *Int J Biochem Cell Biol* **35,** 113–118 (2003).

103. Chester, A. H. & Taylor, P. M. Molecular and functional characteristics of heart-valve interstitial cells. *Philos Trans R Soc Lond B Biol Sci* **362,** 1437–1443 (2007).

104. Chen, J.-H., Chen, W. L. K., Sider, K. L., Yip, C. Y. Y. & Simmons, C. A. β-catenin mediates mechanically regulated, transforming growth factor-β1-induced myofibroblast differentiation of aortic valve interstitial cells. *Arterioscler Thromb Vasc Biol* **31,** 590–597 (2011).

105. Cushing, M. C., Liao, J.-T. & Anseth, K. S. Activation of valvular interstitial cells is mediated by transforming growth factor-β1 interactions with matrix molecules. *Matrix Biology* **24,** 428–437 (2005).

106. Rabkin-Aikawa, E. *et al.* Clinical pulmonary autograft valves: Pathologic evidence of adaptive remodeling in the aortic site. *J Thorac Cardiovasc Surg* **128,** 552–561 (2004).

107. Gupta, V., Werdenberg, J. A., Blevins, T. L. & Grande-Allen, K. J. Synthesis of Glycosaminoglycans in Differently Loaded Regions of Collagen Gels Seeded with Valvular Interstitial Cells. *Tissue Engineering* **13,** 41–49 (2007).

108. Gupta, V., Werdenberg, J. A., Mendez, J. S. & Jane Grande-Allen, K. Influence of strain on proteoglycan synthesis by valvular interstitial cells in three-dimensional culture. *Acta Biomaterialia* **4,** 88–96 (2008).

109. Gupta, V., Tseng, H., Lawrence, B. D. & Grande-Allen, K. J. Effect of cyclic mechanical strain on glycosaminoglycan and proteoglycan synthesis by heart valve cells. *Acta Biomaterialia* **5,** 531–540 (2009).

110. Merryman, W. D. Correlation between heart valve interstitial cell stiffness and transvalvular pressure: implications for collagen biosynthesis. *Am J Physiol Heart Circ Physiol* **290**, H224-H231 (2006).

111. Quick, D. W., Kunzelman, K. S., Kneebone, J. M. & Cochran, R. P. Collagen synthesis is upregulated in mitral valves subjected to altered stress. *ASAIO J.* **43,** 181–186 (1997).

112. Schoen, F. J. Cardiac valves and valvular pathology. *Cardiovasc Pathol* **14,** 189–194 (2005).

113. Mihl, C., Dassen, W. R. M. & Kuipers, H. Cardiac remodelling: concentric versus eccentric hypertrophy in strength and endurance athletes. *Neth Heart J* **16,** 129–133 (2008).

114. Rawlins, J., Bhan, A. & Sharma, S. Left ventricular hypertrophy in athletes. *Eur J Echocardiogr* **10,** 350–356 (2009).

115. Eghbali, M., Wang, Y., Toro, L. & Stefani, E. Heart hypertrophy during pregnancy: a better functioning heart? *Trends Cardiovasc Med* **16,** 285–291 (2006).

116. Li, J. *et al.* New frontiers in heart hypertrophy during pregnancy. *Am J Cardiovasc Dis* **2,** 192–207 (2012).

117. Schannwell, C. M., Zimmermann, T., Schneppenheim, M., Plehn, G., Marx, R., & Strauer, B. E. Left ventricular hypertrophy and diastolic dysfunction in healthy pregnant women. *Cardiology* **97,** 73–78 (2002).

118. Gaasch, W. H. & Meyer, T. E. Left Ventricular Response to Mitral Regurgitation: Implications for Management. *Circulation* **118,** 2298–2303 (2008).

119. Kehat, I. & Molkentin, J. D. Molecular Pathways Underlying Cardiac Remodeling During Pathophysiological Stimulation. *Circulation* **122,** 2727–2735 (2010).

120. Gradman, A. H. & Alfayoumi, F. From Left Ventricular Hypertrophy to Congestive Heart Failure: Management of Hypertensive Heart Disease. *Prog Cardiovasc Dis* **48,** 326–341 (2006).

121. Chaput, M., Handschumacher, M. D., Tournoux, F., Hua, L., Guerrero, J. L., Vlahakes, G. J., & Levine, R. A. Mitral leaflet adaptation to ventricular remodeling: occurrence and adequacy in patients with functional mitral regurgitation. *Circulation* **118,** 845–852 (2008).

122. Dal-Bianco, J. P. *et al.* Active adaptation of the tethered mitral valve: insights into a compensatory mechanism for functional mitral regurgitation. *Circulation* **120,** 334–342 (2009).

123. Grande-Allen, K. J. *et al.* Apparently normal mitral valves in patients with heart failure demonstrate biochemical and structural derangements. *J Am Coll Cardiol* **45,** 54–61 (2005).

124. Grande-Allen, K. J., Barber, J. E., Klatka, K. M., Houghtaling, P. L., Vesely, I., Moravec, C. S., & McCarthy, P. M. Mitral valve stiffening in end-stage heart failure: evidence of an organic contribution to functional mitral regurgitation. *J Thorac Cardiovasc Surg* **130,** 783–790 (2005).

125. Lacerda, C. & Orton, E. C. Evidence of a Role for Tensile Loading in the Pathogenesis of Mitral Valve Degeneration. *J Clin Exp Cardiolog* (2012). doi:10.4172/2155-9880.S3-004

126. Whittaker, P., Boughner, D. R., Perkins, D. G. & Canham, P. B. Quantitative structural analysis of collagen in chordae tendineae and its relation to floppy mitral valves and proteoglycan infiltration. *Br Heart J* **57,** 264–269 (1987).

127. Icardo, J. M., Colvee, E. & Revuelta, J. M. Structural analysis of chordae tendineae in degenerative disease of the mitral valve. *Int J Cardiol* **167,** 1603–1609 (2013).

128. Akhtar, S., Meek, K. M. & James, V. Ultrastructure abnormalities in proteoglycans, collagen fibrils, and elastic fibers in normal and myxomatous mitral valve chordae tendineae. *Cardiovasc Pathol* **8,** 191–201 (1999).

129. Tamura, K., Fukuda, Y., Ishizaki, M., Masuda, Y., Yamanaka, N., & Ferrans, V. J. Abnormalities in elastic fibers and other connective-tissue components of floppy mitral valve. *Am Heart J* **129,** 1149–1158 (1995).

130. Grande-Allen, K. J., Griffin, B. P., Calabro, A., Ratliff, N. B., Cosgrove, D.M. 3rd, & Vesely, I. Myxomatous mitral valve chordae. II: Selective elevation of glycosaminoglycan content. *J Heart Valve Dis* **10,** 325–32– discussion 332–3 (2001).

131. Lis, Y., Burleigh, M. C., Parker, D. J., Child, A. H., Hogg, J., & Davies, M. J. Biochemical characterization of individual normal, floppy and rheumatic human mitral valves. *Biochem J* **244,** 597–603 (1987).

132. Gupta, V. *et al.* Abundance and location of proteoglycans and hyaluronan within normal and myxomatous mitral valves. *Cardiovasc Pathol* **18,** 191–197 (2009).

133. Rabkin, E., Aikawa, M., Stone, J. R., Fukumoto, Y., Libby, P., & Schoen, F. J. Activated interstitial myofibroblasts express catabolic enzymes and mediate matrix remodeling in myxomatous heart valves. *Circulation* **104,** 2525–2532 (2001).

134. Barber, J. E., Kasper, F. K., Ratliff, N. B., Cosgrove, D. M., Griffin, B. P., & Vesely, I. Mechanical properties of myxomatous mitral valves. *J Thorac Cardiovasc Surg* **122,** 955–962 (2001).

135. Barber, J. E., Ratliff, N. B., Cosgrove, D. M., Griffin, B. P. & Vesely, I. Myxomatous mitral valve chordae. I: Mechanical properties. *J Heart Valve Dis* **10,** 320–324 (2001).

136. Emine, B. S., Murat, A., Mehmet, B., Mustafa, K. & Gokturk, I. Flail mitral and tricuspid valves due to myxomatous disease. *Eur J Echocardiogr* **9,** 304–305 (2008).

137. Atlas, P., Yahini, J. H., Palant, A., Lieberman, Y., & Neufeld, H. N. Chordal rupture: a common complication of myxomatous degeneration of the mitral valve. *Isr J Med Sci* **12,** 1320–1324 (1976).

138. Hickey, A.J., Wilcken, D. E. L., Wright, J.S., & Warren, B.A. Primary (Spontaneous) Chordal Rupture: Relation to Myxomatous Valve Disease and Mitral Valve Prolapse. *J Am Coll Cardiol* **5,** 1341–1346 (1985).

139. Lee, Y. S., Chang, C. H., Chen, H. C. & Liang, G. F. Scanning and transmission electron microscopic studies on isolated ruptures of chordae tendineae. *Jpn Heart J* **24,** 355–367 (1983).

140. Heidemann, B. H. & McClure, J. H. Changes in maternal physiology during pregnancy. *Continuing Education in Anaesthesia, Critical Care & Pain* **3,** 65–68 (2003).

141. Pivarnik, J. M., Stein, A. D. & Rivera, J. M. Effect of pregnancy on heart rate/oxygen consumption calibration curves. *Med Sci Sports Exerc* **34,** 750–755 (2002).

142. Robson, S. C., Hunter, S., Boys, R. J. & Dunlop, W. Serial study of factors influencing changes in cardiac output during human pregnancy. *Am J Physiol* **256,** H1060–5 (1989).

143. Hunter, S. & Robson, S. C. Adaptation of the maternal heart in pregnancy. *Br Heart J* **68,** 540–543 (1992).

144. Capeless E. L. and Clapp J. F. Cardiovascular changes in early phase of pregnancy. *Am J Obstet Gynecol* **161,** 1449–1453 (1989).

145. Mabie, W. C., DiSessa, T. G., Crocker, L. G., Sibai, B. M., and Arheart, K. L. A Longitudinal Study of Cardiac Output in Normal Human Pregnancy. *Am J Obstet Gynecol* **39,** 29 (1995).

146. Savu, O. *et al.* Morphological and functional adaptation of the maternal heart during pregnancy. *Circ Cardiovasc Imaging* **5,** 289–297 (2012).

147. Katz, R., Karliner, J. S. & Resnik, R. Effects of a natural volume overload state (pregnancy) on left ventricular performance in normal human subjects. *Circulation* **58,** 434–441 (1978).

148. Torgersen, K. L. & Curran, C. A. A systematic approach to the physiologic adaptations of pregnancy. *Crit Care Nurs Q* **29,** 2–19 (2006).

149. Clark, S. L., *et al.* Central hemodynamic assessment of normal term pregnancy. *Am J Obstet Gynecol* **161,** 1439–1442 (1989).

150. Thornburg, K. L., Jacobson, S. L., Giraud, G. D. & Morton, M. J. Hemodynamic changes in pregnancy. *Semin Perinatol* **24,** 11–14 (2000).

151. Pritchard, J. A. Changes In The Blood Volume During Pregnancy And Delivery. *Anesthesiology* **26,** 393–399 (1965).

152. Peck, T. M. and Arias, F. Hematologic Changes Associated With Pregnancy. *Clin Obstet Gynecol* **22,** 785 (1979).

153. Chesley, L. C. Plasma and red cell volumes during pregnancy. *Am J Obstet Gynecol* **112,** 440–450 (1972).

154. Robson, S. C., Hunter, S., Boys, R. J., and Dunlop, W. Hemodynamic changes during twin pregnancy. *Am J Obstet Gynecol* **161,** 1273–1278 (1989).

155. Kametas, N. Maternal cardiac function in twin pregnancy. *Obstet Gynecol* **102,** 806–815 (2003).

156. Clapp, J. F. & Capeless, E. Cardiovascular function before, during, and after the first and subsequent pregnancies. *Am J Cardiol* (1997).

157. Kemp, C. D. & Conte, J. V. The pathophysiology of heart failure. *Cardiovasc Pathol* **21,** 365–371 (2012).

158. Kametas, N. A., McAuliffe, F., Hancock, J., Chambers, J. & Nicolaides, K. H. Maternal left ventricular mass and diastolic function during pregnancy. *Ultrasound Obstet Gynecol* **18,** 460–466 (2001).

159. Simmons, L. A., Gillin, A. G. & Jeremy, R. W. Structural and functional changes in left ventricle during normotensive and preeclamptic pregnancy. *Am J Physiol Heart Circ Physiol* **283,** H1627–33 (2002).

160. Maillet, M., van Berlo, J. H. & Molkentin, J. D. Molecular basis of physiologicalheart growth: fundamental conceptsand new players. *Nat Rev Mol Cell Biol* **14,** 38–48 (2013).

161. Heineke, J. & Molkentin, J. D. Regulation of cardiac hypertrophy by intracellular signalling pathways. *Nat Rev Mol Cell Biol* **7,** 589–600 (2006).

162. Dorn, G. W. The Fuzzy Logic of Physiological Cardiac Hypertrophy. *Hypertension* **49,** 962–970 (2007).

163. Melenovsky, V. Cardiac adaptation to volume overload. *Cardiac Adaptations* **4,** 167–199 (2013).

164. Cong, J., Fan, T., Yang, X., Squires, J. W., Cheng, G., Zhang, L., & Zhang, Z. Structural and functional changes in maternal left ventricle during pregnancy: a three-dimensional speckle-tracking echocardiography study. *Cardiovasc Ultrasound* **13,** 6 (2015).

165. Estensen, M. E., Beitnes, J. O., Grindheim, G., Aaberge, L., Smiseth, O. A., Henriksen, T., & Aakhus, S. Altered maternal left ventricular contractility and function during normal pregnancy. *Ultrasound Obstet Gynecol* **41,** 659–666 (2013).

166. Wells, S. M., Pierlot, C. M. & Moeller, A. D. Physiological remodeling of the mitral valve during pregnancy. *Am J Physiol Heart Circ Physiol* **303,** H878–92 (2012).

167. Campos, O., Andrade, J. L., Bocanegra, J., Ambrose, J. A., Carvalho, A. C., Harada, K., & Martinez, E. E. Physiologic multivalvular regurgitation during pregnancy: a longitudinal Doppler echocardiographic study. *Int J Cardiol* **40,** 265–272 (1993).

168. Kunzelman, K. S., Reimink, M. S. & Cochran, R. P. Annular dilatation increases stress in the mitral valve and delays coaptation: a finite element computer model. *Cardiovasc Surg* **5,** 427–434 (1997).

169. Grande, K. J., Cochran, R. P., Reinhall, P. G. & Kunzelman, K. S. Mechanisms of aortic valve incompetence: finite element modeling of aortic root dilatation. *ATS* **69,** 1851–1857 (2000).

170. Troxler, L. G., Spinner, E. M. & Yoganathan, A. P. Measurement of strut chordal forces of the tricuspid valve using miniature C ring transducers. *J Biomech* **45,** 1084–1091 (2012).

171. Ray, S. The echocardiographic assessment of functional mitral regurgitation. *Eur J Echocardiogr* **11,** i11–17 (2010).

172. FRCP, T. A. T. B. Valvular Heart Disease and Pregnancy. *Cardiol Clin* **30,** 369–381 (2012).

173. Sliwa, K. & Bohm, M. Incidence and prevalence of pregnancy-related heart disease. *Cardiovasc Res* **101,** 554–560 (2014).

174. Lloyd-Jones, D. M. *et al.* Lifetime risk for developing congestive heart failure: the Framingham Heart Study. *Circulation* **106,** 3068–3072 (2002).

175. World Health Organization. *Global status report on noncommunicable diseases*. (World Health Organization, 2014).

176. Heidenreich, P. A. *et al.* Forecasting the impact of heart failure in the United States: a policy statement from the American Heart Association. *Circ Heart Fail* **6,** 606–619 (2013).

177. Mehra, M. R., Reyes, P., Benitez, R. M., Zimrin, D. & Gammie, J. S. Surgery for Severe Mitral Regurgitation and Left Ventricular Failure: What Do We Really Know? *J Card Fail* **14,** 145–150 (2008).

178. Geha, A. S., El-Zein, C. & Massad, M. G. Mitral Valve Surgery in Patients with Ischemic and Nonischemic Dilated Cardiomyopathy. *Cardiology* **101,** 15–20 (2004).

179. Eghbali, M., Deva, R., Alioua, A., Minosyan, T. Y., Ruan, H., Wang, Y., Toro, L., & Stefani, E. Molecular and functional signature of heart hypertrophy during pregnancy. *Circ Res* **96,** 1208–1216 (2005).

180. Blondheim, D. S., Jacobs, L. E., Kotler, M. N., Costacurta, G. A. & Parry, W. R. Dilated cardiomyopathy with mitral regurgitation: decreased survival despite a low frequency of left ventricular thrombus. *Am Heart J* **122,** 763–771 (1991).

181. Junker, A., Thayssen, P., Nielsen, B. & Andersen, P. E. The hemodynamic and prognostic significance of echo-Doppler-proven mitral regurgitation in patients with dilated cardiomyopathy. *Cardiology* **83,** 14–20 (1993).

182. Koelling, T. M., Aaronson, K. D., Cody, R. J., Bach, D. S. & Armstrong, W. F. Prognostic significance of mitral regurgitation and tricuspid regurgitation in patients with left ventricular systolic dysfunction. *Am Heart J* **144,** 524–529 (2002).

183. Zuber, M., Gautschi, N., Oechslin, E., Widmer, V., Kiowski, W., and Jenni, R. Outcome of pregnancy in women with congenital shunt lesions. *Heart* **81,** 271–275 (1999).

184. Wilansky, S., Reuss, C. S. & Willerson, J. T. Pregnancy and the Heart. *Cardiovascular Medicine* (2007).

185. Robson, S. C., Richley, D., Boys, R. J. & Hunter, S. Incidence of Doppler regurgitant flow velocities during normal pregnancy. *Eur Heart J* **13,** 84–87 (1992).

186. Pierlot, C. M., Lee, J. M., Amini, R., Sacks, M. S. & Wells, S. M. Pregnancy-Induced Remodeling of Collagen Architecture and Content in the Mitral Valve. *Ann Biomed Eng* **42,** 2058–2071 (2014).

187. Pierlot, C. M., Moeller, A. D., Lee, J. M. & Wells, S. M. Biaxial Creep Resistance and Structural Remodeling of the Aortic and Mitral Valves in Pregnancy. *Ann Biomed Eng* **43,** 1772–1785 (2015).

188. Wells, S. M. Structure and thermal stability of heart valve chordae tendinae: association with physiological loading conditions. *Proc BMES Annual Meeting* (2011).

189. Wilkes, B. & Wells, S. M. Thermomechanical properties of branching chordae tendinae. *Proc BMES Annual Meeting* (2011).

190. Stephens, E. H. *et al.* Significant changes in mitral valve leaflet matrix composition and turnover with tachycardia-induced cardiomyopathy. *Circulation* **120,** S112–9 (2009).

191. Reed, C. C. & Iozzo, R. V. The role of decorin in collagen fibrillogenesis and skin homeostasis. *Glycoconj J* **19,** 249–255 (2002).

192. Schönherr, E., Hausser, H., Beavan, L. & Kresse, H. Decorin-type I collagen interaction. Presence of separate core protein-binding domains. *J Biol Chem* **270,** 8877–8883 (1995).

193. Zhang, G., Young, B. B., Ezura, Y., Favata, M., Soslowsky, L. J., Chakravarti, S., & Birk, D. E. Development of tendon structure and function: regulation of collagen fibrillogenesis. *J Musculoskelet Neuronal Interact* **5,** 5–21 (2005).

194. Reese, S. P., Underwood, C. J. & Weiss, J. A. Effects of decorin proteoglycan on fibrillogenesis, ultrastructure, and mechanics of type I collagen gels. *Matrix Biol* **32,** 414–423 (2013).

195. Aikawa, E., Whittaker, P., Farber, M., Mendelson, K., Padera, R. F., Aikawa, M., & Schoen, F. J. Human semilunar cardiac valve remodeling by activated cells from fetus to adult: implications for postnatal adaptation, pathology, and tissue engineering. *Circulation* **113,** 1344–1352 (2006).

196. Pierlot, C. M., Moeller, A. D., Lee, J. M. & Wells, S. M. Pregnancy-induced remodeling of heart valves. *Am J Physiol Heart Circ Physiol* **309,** H1565–78 (2015).

197. Norris, R. A., Moreno-Rodriguez, R., Hoffman, S. & Markwald, R. R. The many facets of the matricelluar protein periostin during cardiac development, remodeling, and pathophysiology. *J Cell Commun Signal* **3,** 275–286 (2009).

198. Hakuno, D. *et al.* Periostin advances atherosclerotic and rheumatic cardiac valve degeneration by inducing angiogenesis and MMP production in humans and rodents. *J Clin Invest* **120,** 2292–2306 (2010).

199. Conway, S. J., Izuhara, K., Kudo, Y., Litvin, J., Markwald, R., Ouyang, G., Arron, J. R., Holweg, C. T. J., & Kudo, A. The role of periostin in tissue remodeling across health and disease. *Cell Mol Life Sci* **71,** 1279–1288 (2014).

200. Hamilton, D. W. Functional role of periostin in development and wound repair: implications for connective tissue disease. *J Cell Commun Signal* **2,** 9–17 (2008).

201. Norris, R. A. *et al.* Periostin regulates atrioventricular valve maturation. *Dev Biol* **316,** 200–213 (2008).

202. Norris, R. A. *et al.* Periostin regulates collagen fibrillogenesis and the biomechanical properties of connective tissues. *J Cell Biochem* **101,** 695–711 (2007).

203. Reynolds, M. Measurement of bovine plasma and blood volume during pregnancy and lactation. *Am J Physiol* **175,** 118–122 (1953).

204. Scheaffer, A. N., Caton, J. S., Bauer, M. L. & Reynolds, L. P. Influence of pregnancy on body weight, ruminal characteristics, and visceral organ mass in beef heifers. *J Anim Sci* **79,** 2481–2490 (2001).

205. Rexroad, C. E., Casida, L. E. & Tyler, W. J. Crown-Rump Length of Fetuses in Purebred Holstein-Friesian Cows. **57,** 346–347 *J Dairy Sci* (1974).

206. Shi, S. R., Key, M. E. & Kalra, K. L. Antigen retrieval in formalin-fixed, paraffin-embedded tissues: an enhancement method for immunohistochemical staining based on microwave oven heating of tissue sections. *J Histochem Cytochem* **39,** 741–748 (1991).

207. Shi, S. R., Imam, S. A., Young, L., Cote, R. J. & Taylor, C. R. Antigen retrieval immunohistochemistry under the influence of pH using monoclonal antibodies. *J Histochem Cytochem* **43,** 193–201 (1995).

208. Shi, S. R., Cote, R. J. & Taylor, C. R. Antigen retrieval techniques: current perspectives. *J Histochem Cytochem* **49,** 931–937 (2001).

209. Shi, S. R., Cote, R. J. & Taylor, C. R. Antigen retrieval immunohistochemistry: past, present, and future. *J Histochem Cytochem* **45,** 327–343 (1997).

210. Shi, S. R. *et al.* Standardization of immunohistochemistry based on antigen retrieval technique for routine formalin-fixed tissue sections. *Appl Immunohistochem* **6** 89–96 (1998).

211. Biddolph, S. C. & Jones, M. Low-Temperature, Heat-Mediated Antigen Retrieval (LTHMAR) on Archival Lymphoid Sections. *Appl Immunohistochem Mol Morphol* **7,** 289 (1999).

212. Shi, S. R. & Taylor, C. R. *Immunohistochemical Staining Methods, 6th Edition.* Antigen Retrieval. Part 1: The Staining Process Chapter 3**.** 30–45 (Dako, 2013).

213. Struijk, P. C., Mathews, V. J., Loupas, T., Stewart, P. A., Clark, E. B., Steegers, E. A., & Wladimiroff, J. W. Blood pressure estimation in the human fetal descending aorta. *Ultrasound Obstet Gynecol* **32,** 673–681 (2008).

214. Kiserud, T., Ebbing, C., Kessler, J. & Rasmussen, S. Fetal cardiac output, distribution to the placenta and impact of placental compromise. *Ultrasound Obstet Gynecol* **28,** 126–136 (2006).

215. Rasanen, J., Wood, D. C., Weiner, S., Ludomirski, A., & Huhta, J. C. Role of the pulmonary circulation in the distribution of human fetal cardiac output during the second half of pregnancy. *Circulation* **94,** 1068–1073 (1996).

216. Kiserud, T. & Acharya, G. The fetal circulation. *Prenat Diagn* **24,** 1049–1059 (2004).

217. Hove, J. R., Koster, R. W., Forouhar, A. S., Acevedo-Bolton, G., Fraser, S. E., & Gharib, M. Intracardiac fluid forces are an essential epigenetic factor for embryonic cardiogenesis. *Nature* **421,** 172–177 (2003).

218. Bartman, T. *et al.* Early Myocardial Function Affects Endocardial Cushion Development in Zebrafish. *PloS Biol* **2,** e129 (2004).

219. Sedmera, D., Pexieder, T., Rychterova, V., Hu, N. & Clark, E. B. Remodeling of chick embryonic ventricular myoarchitecture under experimentally changed loading conditions. *Anat Rec* **254,** 238–252 (1999).

220. Butcher, J. T., McQuinn, T. C., Sedmera, D., Turner, D. & Markwald, R. R. Transitions in Early Embryonic Atrioventricular Valvular Function Correspond With Changes in Cushion Biomechanics That Are Predictable by Tissue Composition. *Circ Res* **100,** 1503–1511 (2007).

221. Oosthoek, P. W., Wenink, A. C., Vrolijk, B. C., Wisse, L. J., DeRuiter, M.C., Poelmann, R. E., & Gittenberger-de Groot, A. C. Development of the atrioventricular valve tension apparatus in the human heart. *Anat Embryol* **198,** 317–329 (1998).

222. Morse, D. E., Hamlett, W. C. & Noble, C. W. Morphogenesis of chordae tendineae. I: Scanning electron microscopy. *Anat Rec* **210,** 629–638 (1984).

223. Miles, C. A., Burjanadze, T. V. & Bailey, A. J. The kinetics of the thermal denaturation of collagen in unrestrained rat tail tendon determined by differential scanning calorimetry. *J Mol Biol* **245,** 437–446 (1995).

224. Miles, C. A., Avery, N. C., Rodin, V. V. & Bailey, A. J. The Increase in Denaturation Temperature Following Cross-linking of Collagen is Caused by Dehydration of the Fibres. *Journal of Molecular Biology* **346,** 551–556 (2005).

225. le Lous, M., Flandin, F., Herbage, D. & Allain, J. C. Influence of collagen denaturation on the chemorheological properties of skin, assessed by differential scanning calorimetry and hydrothermal isometric tension measurement. *Biochim Biophys Acta* **717,** 295–300 (1982).

226. Nazari, S. *et al.* Patterns of systolic stress distribution on mitral valve anterior leaflet chordal apparatus. A structural mechanical theoretical analysis. *J Cardiovasc Surg (Torino)* **41,** 193–202 (2000).

227. Beaudoin, J., Thai, W. E., Wai, B., Handschumacher, M. D., Levine, R. A., & Truong, Q. A. Assessment of mitral valve adaptation with gated cardiac computed tomography: validation with three-dimensional echocardiography and mechanistic insight to functional mitral regurgitation. *Circ Cardiovasc Imaging* **6,** 784–789 (2013).

228. Obase, K. *et al.* Elongation of chordae tendineae as an adaptive process to reduce mitral regurgitation in functional mitral regurgitation. *Eur Heart J Cardiovasc Imaging* **17,** 500–509 (2016).

229. Dickinson, M. G. & Vesely, I. Structural changes of rat mitral valve chordae tendineae during postnatal development. *J Heart Valve Dis* **21,** 433–439 (2012).

230. Chen, L., Yin, F. C. & May-Newman, K. The structure and mechanical properties of the mitral valve leaflet-strut chordae transition zone. *J Biomech Eng* **126,** 244–251 (2004).

231. Changoor, A., Tran-Khanh, N., Methot, S., Garon, M., Hurtig, M. B., Shive, M. S., & Buschmann, M. D. A polarized light microscopy method for accurate and reliable grading of collagen organization in cartilage repair. *Osteoarthr Cartil* **19,** 126–135 (2011).

232. Osaki, S., Tohno, S., Tohno, Y., Ohuchi, K. & Takakura, Y. Determination of the orientation of collagen fibers in human bone. *Anat Rec* **266,** 103–107 (2002).

233. Pagiatakis, C., Galaz, R., Tardif, J.-C. & Mongrain, R. A comparison between the principal stress direction and collagen fiber orientation in coronary atherosclerotic plaque fibrous caps. *Med Biol Eng Comput* **53,** 545–555 (2015).

234. Parto, P., Tadjalli, M. & Ghazi, S. R. Light and Ultrastructural Study of the Chordae Tendineae in the Heart of the Ostrich (Struthio camelus). *World J Med Sci* **4,** 93-97 (2009).

235. Häkkinen, L., Strassburger, S., Kahari, V. M., Scott, P. G., Eichstetter, I., Lozzo, R. V., & Larjava, H. A role for decorin in the structural organization of periodontal ligament. *Lab Invest* **80,** 1869–1880 (2000).

236. Kara, R. J. *et al.* Fetal cells traffic to injured maternal myocardium and undergo cardiac differentiation. *Circ Res* **110,** 82–93 (2012).

237. Shapiro, S. D., Endicott, S. K., Province, M. A., Pierce, J. A. & Campbell, E. J. Marked longevity of human lung parenchymal elastic fibers deduced from prevalence of D-aspartate and nuclear weapons-related radiocarbon. *J Clin Invest* **87,** 1828–1834 (1991).

238. Pierce, R. A., Mariani, T. J. & Senior, R. M. Elastin in lung development and disease. *Ciba Found Symp* **192,** 199–212– discussion 212–4 (1995).

239. Myers, B., Dubick, M., Last, J. A. & Rucker, R. B. Elastin synthesis during perinatal lung development in the rat. *Biochim Biophys Acta* **761,** 17–22 (1983).

240. Davis, E. C. Elastic lamina growth in the developing mouse aorta. *J Histochem Cytochem* **43,** 1115–1123 (1995).

241. Davis, E. C. Stability of elastin in the developing mouse aorta: a quantitative radioautographic study. *Histochemistry* **100,** 17–26 (1993).

242. Debay, D. R. & Wells, S. M. Structural-mechanical relationships in the thoracic aorta during pregnancy-induced remodelling. *Proc BMES Annual Meeting* (2006).

243. Brennan-Pierce, E. P. & Wells, S. M. Pregnancy-induced cardiovascular remodeling is not reversed. *Proc BMES Annual Meeting* (2012).

244. Baker, P. B., Bansal, G., Boudoulas, H., Kolibash, A. J., Kilman, J., & Wooley, C. F. Floppy mitral valve chordae tendineae: histopathologic alterations. *Hum Pathol* **19,** 507–512 (1988).

245. Eyden, B. The myofibroblast: phenotypic characterization as a prerequisite to understanding its functions in translational medicine. *J Cell Mol Med* **12,** 22–37 (2008).

246. Kern, C. B. *et al.* Immunolocalization of chick periostin protein in the developing heart. *Anat Rec A Discov Mol Cell Evol Biol* **284,** 415–423 (2005).

247. Norris, R. A., Kern, C. B., Wessels, A., Moralez, E. I., Markwald, R. R., Mjaatvedt, C. H. Identification and detection of the periostin gene in cardiac development. *Anat Rec* **281A,** 1227–1233 (2004).

248. Lie-Venema, H. *et al.* Periostin expression by epicardium-derived cells is involved in the development of the atrioventricular valves and fibrous heart skeleton. *Differentiation* **76,** 809–819 (2008).

249. Robson, S. C., Dunlop, W., Moore, M. & Hunter, S. Haemodynamic changes during the puerperium: a Doppler and M-mode echocardiographic study. *Br J Obstet Gynaecol* **94,** 1028–1039 (1987).

250. Silversides, C. K. & Colman, J. M. *Heart Disease in Pregnancy, 2nd Edition.* Physiological changes in pregnancy. Chapter 2. (BMJ Books, 2007).

251. Fujitani, S. & Baldisseri, M. R. Hemodynamic assessment in a pregnant and peripartum patient. *Crit Care Med* **33,** S354-S361 (2005).

252. Umar, S., Nadadur, R., Iorga, A., Amjedi, M., Matori, H., & Eghbali, M. Cardiac structural and hemodynamic changes associated with physiological heart hypertrophy of pregnancy are reversed postpartum. *J Appl Physiol* **113,** 1253–1259 (2012).

253. Robson, S. C., Dunlop, W., Moore, M. & Hunter, S. Combined Doppler and echocardiographic measurement of cardiac output: theory and application in pregnancy. *Br J Obstet Gynaecol* **94,** 1014–1027 (1987).

254. Goldsmith, L. T. & Weiss, G. Relaxin in Human Pregnancy. *Ann N Y Acad Sci* **1160,** 130–135 (2009).

255. Zhao, L., Samuel, C. S., Tregear, G. W., Beck, F. & Wintour, E. M. Collagen studies in late pregnant relaxin null mice. *Biol Reprod* **63,** 697–703 (2000).

256. Luque, E. H., Muñoz de Toro, M. M., Ramos, J. G., Rodriguez, H. A. & Sherwood, O. D. Role of relaxin and estrogen in the control of eosinophilic invasion and collagen remodeling in rat cervical tissue at term. *Biol Reprod* **59,** 795–800 (1998).

257. Samuel, C. S., Coghlan, J. P. & Bateman, J. F. Effects of relaxin, pregnancy and parturition on collagen metabolism in the rat pubic symphysis. *J Endocrinol* **159,** 117–125 (1998).

258. Pinheiro, M. C., Morase, S. G., Battlehner, C. N., Caldini, E. G., Toledo, O. M., Joazeiro, P. P. Histochemical and ultrastructural study of collagen fibers in mouse pubic symphysis during late pregnancy. *Micron* **35,** 685–693 (2004).

259. Goldsmith, L. T. *et al.* Relaxin regulation of endometrial structure and function in the rhesus monkey. *Proc Natl Acad Sci U.S.A.* **101,** 4685–4689 (2004).

260. Hsu, S. Y., Nakabayashi, K., Nishi, S., Kumagai, J., Kudo, M., Sherwood, O. D., & Hsueh, A. J. Activation of orphan receptors by the hormone relaxin. *Science* **295,** 671–674 (2002).

261. Dschietzig, T., Richter, C., Bartsch, C., Laule, M., Armbruster, F. P., Baumann, G., & Stangl K. The pregnancy hormone relaxin is a player in human heart failure. *FASEB J* **15,** 2187–2195 (2001).

262. Kapelouzou, A., Tsourelis, L., Kaklamanis, L., Degiannis, D., Kogerakis, N., & Cokkinos, D. V. Serum and tissue biomarkers in aortic stenosis. *Glob Cardiol Sci Pract* **2015,** 49 (2015).

263. Sattar, N. & Greer, I. A. Pregnancy complications and maternal cardiovascular risk: opportunities for intervention and screening? *BMJ* **325,** 157–160 (2002).